Mechanophenotyping Actin Networks in Minimal Cell Models

by

Nadab Habtamu Wubshet

A dissertation submitted in partial fulfillment
of the requirements for the degree of
Doctor of Philosophy
(Mechanical Engineering)
in the University of Michigan
2023

Doctoral Committee:

Associate Professor Allen P. Liu, Chair
Assistant Professor Morgan DeSantis
Professor Edgar Meyhofer
Professor Shravan Veerapaneni

Nadab Habtamu Wubshet

nadab@umich.edu

ORCID iD: 0000-0001-8735-8854

Dedication

I would like to dedicate this thesis to my grandmother, Emahoy Asnakech Filate (እማማ).

“ይብላኝልኝ አዴ አዳዬ : ውለታሽን ላልከፈልኩት”

Acknowledgements

I would like to acknowledge my advisor, Allen Liu, for his continued support and mentorship over the past 5 years. Thank you for challenging me and providing the space and freedom for me to explore and find directions in science. I owe a lot to you for my growth as a scientist. I would like to thank members of the Liu Lab, past and present. I have learned a lot from each of you and happy to call you all friends. I would like to thank everyone at University of Michigan that supported me and made my stay worthwhile. Special thanks to Laurie Nanofabrication laboratory (LNF) staff, and the Microfluidics in Biomedical Sciences Training Program (MBSTP).

I would like to thank my family and friends who enrich my life with more love, and who I continue to admire, look up to, and learn from. To my parents, I owe a lot to my father and my mother for their unwavering support all throughout my life. To my mother, Zewditu Yitafer, I can write another thesis about you. Thank you for raising me with all your might, for your love, for your kindness, and for your prayers.

“በእናንተ ዘንድ ሁሉ በፍቅር ይሁን።”

Table of Contents

List of Figures

List of Tables

Abstract

Actin, a highly conserved and abundant protein, constructs a fibrous matrix via actin binding proteins (ABPs) equipping the cell to sustain, exert, and sense forces. Actin assembly plays an important role in directed cell migration during wound healing, cancer metastasis, immune response, and embryonic development. Although actin is a well-studied protein, owing to inherent complexity of the cell, significant gaps remain in understanding how different actin architectures transform, interact, and behave to endow the mechanical behaviors of the cell. In my thesis, I investigate how cells mechanically respond to the absence of native physical forces, how ABPs cooperate and compete to construct actin networks, and how different actin architectures dictate cellular mechanophenotypes. The bulk of my thesis work leverages bottom-up construction of minimal cell models to decouple actin networks from the complex cytoplasm milieu.

In Chapter 3, we study mechanical response of human osteoblasts to simulated microgravity. Using a home-built random positioning machine to generate simulated microgravity, we find that actin networks become highly disorganized leading to less spread and more rounded cells. Furthermore, cells subjected to microgravity become significantly softer. These findings reveal that microgravity influences osteoblast cell mechanics through actin disassembly.

In Chapter 4, we introduce bottom-up reconstitution of actin networks in a minimal cell to decouple actin networks from the rest of the cytoplasm. Here, we reverse engineer a minimal cell model using giant unilamellar vesicle (GUV) encapsulating actin networks. We study

architectural phenotypes assembled by fascin and Arp2/3 complex. While fascin-bundled actin forms membrane protrusive structures, membrane-associated Arp2/3 complex assembles a uniform cortical dendritic shell. When co-encapsulated, we hypothesize that fascin and Arp2/3 cooperates/competes in a concentration dependent manner. Under this condition, we find that fascin-bundled membrane protrusions are reduced due to the branching effect of Arp2/3 complex that shortens filaments. Our results provide support that ABPs compete to generate diverse actin structures to meet the needs of a cell.

In Chapter 5, I electrically deform different actin network-encapsulating GUVs to study differential cell mechanics. I discover that increasing concentrations of filamentous actin dampens GUV deformability. Furthermore, GUVs with alpha-actinin crosslinked actin networks and actin cortex both exhibit even larger dampening of electrodeformability. Our results highlight the significance of actin network architecture in governing cellular mechanics.

In Chapter 6, I explore how actin cortex and bundles rearrange in response to loading exerted by micropipette aspiration. Interestingly, we find that protrusive actin bundles that are otherwise randomly oriented in a GUV lumen collapse and align along the axis of the micropipette. When uniform cortex-GUVs are aspirated, bleb-like cortex-free membrane is aspirated in the micropipette. These results reveal distinct responses in the rearrangement of actin networks subjected to physical forces.

In summary, my dissertation characterizes actin network mechanics in cells and in minimal cell models and addresses how different ABPs cooperate and compete to assemble actin networks with architectures that in turns influence their mechanical behaviors and their responses to load. I believe that these findings improve our understanding of how precisely actin networks endow the mechanics of the cell using a low complexity cell-like environment.

Chapter 1 Introduction

1.1 How do cells navigate and adapt to the physical environment?

Akin to the macroenvironment in which complex organisms like us exist and thrive in, the microscale environment cells endure is also full of complex physical mazes that demand intricate navigation and adaptation. Substrates of different rigidity, trails of variable confinement, and mechanical loads of variable intensities are the major elements that design the physical environment of cells. These conditions insist cells to be highly malleable. Changing shape, bearing load and escaping unfavorable physical restraints are some of the essential processes that assure continuation a cellular life. Over billions of years of effort, cells have produced the necessary machinery, the cytoskeleton, to stroll through such environments through sensing cues, exerting forces, and transforming shapes.

1.2 The cytoskeleton in a nutshell

The cytoskeleton, appropriately named, is the skeleton of the cell. Like bones and cartilages, it is the structural scaffold of a cell. Unlike bones, however, the cytoskeleton is comprised of protein-based polymeric fibers able to dynamically assemble and disassemble allowing cells to morph in response to chemical and mechanical cues. We can condense the purpose of the cytoskeleton in to three broad categories. First, because the cytoskeleton constructs the matrix of the cell, it innately spatially organizes the remaining cellular elements.

Second, the cytoskeleton, via linkage with transmembrane proteins, connects the inside of the cell to the outside. Third, the cytoskeleton exerts forces able to remodel the cell and the extracellular matrix (1). These three broad function classifications of the cytoskeleton are responsible for endowing mechanical characteristics of a living cell.

1.3 Cytoskeletal polymers

The cytoskeleton is comprised of three groups of filamentous fibers namely microtubule, intermediate filaments and actin filaments.

1.3.1 Microtubule

Microtubules are self-organizing tubular filamentous fibers that are found in all dividing eukaryotic cells and has a bacterial homology in FtsZ. Heterodimeric subunits α- and β-tubulin string together to form polar protofilaments, and 13 of these protofilaments cylindrically assemble to form a hollow microtubule fiber. The dynamics of microtubule is intrinsically regulated by GTP hydrolysis and by microtubule-associated proteins (MAPs), post-translational modification factors and motor proteins (2,3). Among polymerization factors assembling microtubules are plus-end-tracking proteins (+TIPs). Bound to the microtubule terminal, +TIPs facilitate αβ-tubulin dimer recruitment to the plus end of the mother filament (4). Kinesin family of proteins, on the other hand, are involved in the disassembly of microtubule filaments via walking on microtubule and removing subunits from the terminal end (5,6). A large multi-protein motor complex dynein associates with microtubules, generating motive forces towards the minus end of the microtubule regulate flagellar swimming (7) and assist mitotic spindle formation (8). Dynein complex function, it's velocity in particular, has been shown to be promoted by factors such as LIS1 (9). Additionally, post-translational modification of

microtubule such as tyrosination and acetylation facilitate stabilization of microtubule filament through improving MAPs and control motor protein trafficking, respectively (3,10).

Among the well-studied functions of microtubules are spatial organization of organelles including the nucleus and its genetic content, molecular transport, and cellular morphogenesis. In eukaryotic cells, microtubule is nucleated at microtubule organizing centers (MTOC), and centrosomes take hold of this role in dividing cells (11). During cell division, microtubules play a vital role in correct positioning of organelles and most importantly equally separating chromosomes through the formations of mitotic spindles, an astral pair of antiparallel active structures (12,13). Other non-centrosomal MTOCs nucleating microtubules, such as from the Golgi, assemble the microtubules in numerous different orientations regulating cell mechanics and molecular transport (11). Furthermore, microtubules are responsible for the formation of growth cones via collaboration with actin networks and intermediate filaments (14). Not only an integral part of cell function and mechanics, due to their principal participation during mitosis and cell migration, microtubules have been a prime therapy target for anticancer (15) and antiparasitic (16) treatments that aim to alter the dynamics of microtubules.

1.3.2 Intermediate filaments

A family of proteins that regulate cellular mechanics, especially as stress absorbers, are the intermediate filaments (IFs). Unlike microtubules and actin filaments, IFs are not conserved throughout different cells of the same species. In humans, there are over 65 IF encoding genes and their abundance is highly variable from one cell to another reaching up to 85% of the total protein mass in squamous epithelial cells and other fully differentiated keratinocytes (17,18). Intermediate filaments also occupy the nuclear space and are the key contributors for defining the shape of the nucleus. While actin filaments and microtubules are assembled from their

nucleotide bound globular protein subunits that are joined through ATP or GTP, intermediate filaments are assembled through specific subunit interaction such as basic and acidic heterodimer formation without substantial utilization of cofactors. Additional remodeling of intermediate filaments and their dynamics are mediated through phosphorylation and kinase activity (19).

IFs, either cytoplasmic or nuclear, are major contributors to a cell's ability to bear and sustain mechanical loads. In the cytoplasm, keratin, a type of IF, is the main contributor to the mechanical property of keratinocytes and mutation of keratin encoding genes could lead to diseases that induce cellular fragility and subsequently compromised mechanical integrity of the skin that can easily cause blisters and erosion (20). IFs such as lamins, particularly lamin A and C, on the other hand, are responsible for maintaining the shape, stiffness and also chromatin organization inside the nucleus (21). Downregulation or mutation of lamins can lead to nuclear fragility causing a multitude of diseases.

1.3.3 Actin

In 1942, Szent Gyorgyi and colleagues who studied muscle contraction discovered by accident that a myosin extract reversibly thickens over a period of 24 hours. Following their observation, they saw that addition of ATP to the myosin extract reduced the viscosity back to its original consistency suggesting that the extract has more than just myosin. This observation commenced the discovery of actin, at the time thought to only exist in muscle. Actin, the protein of interest in the scope of this thesis work, is one of the most abundant proteins universal for all eukaryotic cells with a molecular weight of ~43,000 Da. Actin is a highly conserved protein between different species, and has near-identical amino acid sequence between its muscle and non-muscle isoforms. There are 6 different isoforms of actin depending on their tissue specificity, α-cardiac actin, α-skeletal muscle actin, α-smooth muscle actin, ϒ-smooth muscle

actin and cytoplasmic actin isoforms β-actin and ϒ-actin (22,23). Throughout this thesis work, experiments are conducted exclusively using α-skeletal muscle actin. Structurally, actin has 2 domains commonly referred to as large and small domains despite the fact that they are of similar sizes (24). Between these two domains is an ATP-binding cleft stabilized in the presence of divalent ions (25). The polymerization of globular actin into helical filaments in the right salt buffer condition is purely regulated through nucleotide exchange and hydrolysis. After the initial, either spontaneous or assisted nucleation of two or three actin monomers, ATP-actin monomers rapidly polymerize at the barbed end of the filament (+ end) and hydrolyze to ADP-actin (26). At the pointed end (- end), ADP-actin dissociates from the filament and is replenished by new available ATP-actin. This polar polymerization/depolymerization process is referred to as treadmilling and is also characteristic to microtubules.

1.4 Actin dynamics

Continuous assembly and disassembly of the actin cytoskeleton is the lifeline of a cell. So, how do cells seamlessly compose a mechanical structure with up to a 1 billion subunits, deconstruct, build again, and sustain this cycle over its lifetime? The dynamics of all actin networks inside a cell is regulated by a class of proteins that interact with actin called actin binding proteins (ABPs). ABPs can be categorized as monomer binding and filament binding. These group of proteins are responsible for the malleability of actin networks via inhibiting aggregate formation, initiating filament growth, facilitating filament growth, assembly of all manner of actin architectures, arresting filament growth, and disassembling filament through severing.

Profilin, a small, ~14-17 kDa, ABP binds to the barbed end of actin and regulates actin dynamics by sequestering actin monomers and enhancing polymerization. By sequestrating actin, profilin reduces the available free actin monomers and also prevents spontaneous nucleation (27). Simultaneously, profilin also exponentially increases the rate of ATP/ADP exchange, thereby facilitating the filament polymerization (28). The growth of an actin filament is arrested by heterodimeric capping protein (CP) that binds to the barbed end of the filament (29). CPs play a vital role in the assembly of a complex actin network by cooperating along with crosslinker proteins in tandem. Opposite to profilin, actin ABPs such as cofilin and gelsolin are responsible for filament depolymerization through severing (30). A crucial step in the formation of an actin filament is nucleation of 2 or 3 subunits. While this can happen solely from diffusion and nucleotide exchange, ABPs such as formin play a vital role in accelerating this process (31,32). Additionally, myosin, a filament-binding family of motor proteins that decorate and contract actin filaments, is among the extensively studied ABPs.

Another cohort of ABPs are crosslinker proteins. Complex subcellular scaffolds that equip cells with molecular tools to migrate, divide, adhere, morph to different shapes are orchestrated in concert through the assembly of actin filaments into unique architectures using crosslinker proteins. Among over 20 crosslinker proteins, fascin, alpha-actinin, Arp2/3 complex, will be extensively used throughout this dissertation. Fascin is a 55-kDa short actin crosslinker with two actin binding sites at both the N and C terminus, and it tightly packs and bundles parallel actin filaments (33). Fascin-bundled actin networks are responsible for fingerlike protrusions in structures like filopodia and microspikes at the periphery of the cell (34). Belonging in the spectrin family of proteins, alpha-actinin a longer antiparallel dimeric actin crosslinking protein with an actin binding site on both ends (35). Compared to fascin bundles,

alpha-actinin assembles a rather flexible actin crosslinks and has a unique ability to crosslink actin both in a parallel and antiparallel manner by changing its structural conformation (36). Alpha-actinin, weighting at 100 kDa, is largely recognized as a crosslinker assembling actin architectures that mechanically reinforce the cell via the formation integrin-associated stress fibers to facilitate adhesion along with myosin and tropomyosin (37). Beyond bundling actin filaments, ABPs also assemble actin networks by means of branching. Arp2/3 complex is a 224-kDa multifunctional actin-branching protein made up of seven subunits. Arp2/3 complex is activated by the different nucleation promoting factors (NPFs) among which is the neural Wiskott-Aldrich syndrome (N-WASP) family of proteins, creating 70^{o} branched dendritic actin network at the periphery of the cell (38). Intrinsically, Arp2/3 complex is in an inactive state and activation through NPFs, which has affinity to both actin and Arp2/3 complex, activates Arp2/3 complex and enables binding to the side of the mother actin filament. Subsequently, Arp2 and Arp 3, which are structurally similar to globular actin undergo conformational change acting as the first two subunits in the daughter branch filament (39). The branching of actin filaments at the leading edge of the motile cells that pushes on the membrane each exerts pico-netwon-level forces, and collectively propel the membrane forward during cell migration (40).

Numerous other actin crosslinkers such as filamin, scruin, anillin, synapsin, spectrin, fimbrin, and villin, although not covered in this thesis are all ABPs capable of forming a scaffold essential for a multitude of cellular processes.

1.5 The role of actin in cell mechanics

While there are a plethora of scientific studies investigating the role of actin in cellular processes, in the interest of the scope of this work, we will exclusively look at the role of actin in

cell mechanics and related topics in this section. Cell mechanics itself is no one singular cellular property, but rather an amalgamation of characteristics defining how cells exert mechanical forces to effect a cellular process and to sense and respond to physical loads in a cell's native environment.

Through actin assembly, cells exert mechanical forces that enable them to change their shape and induce motive forces necessary for directed migration. This requires the assembly of actin with spatial specificity where the leading edge of the cell is enriched with networks able to generate a propulsion force consequently remodeling a viscoelastic membrane through the formation of lamellopodia and fillopodia. As for the rear of the cell during directed migration, it follows the leading edge through actomyosin contraction that advances the rear forward. Actin dynamics in cellular morphogenesis and directed migration is a key regulator of cancer cell metastasis. In the progression of cancerous tumors, a tumor develops to malignancy when a cell from the primary tumor dislodges and transits through the body to form secondary other organs. The transit to prime secondary tumors demands metastatic cencer cells to be soft and migratory enough to enter blood vessels via intravasating through a highly constricted endothelial barrier. Under these circumstances, actin cytoskeleton undergoes a game of balance and optimization by making cells highly migratory through the formation of lamellopodia and fillopodia in constricted regions, while maintaining a reduced cytoskeletal pre-stress to easily squeeze through during intravasation.

Actin is also the cellular machinery that equips the cell with the capacity to adapt to its physical environment. The mechanical environment is a vital cue for cells and their ability to sense it could determine their fate. Cell differentiation (41), activation (42), cell-cell communication through junctions (43), motility (44) and tissue formation (45) are a few of the

examples that necessitate mechanical cue sensing. In a study investigating T-cells for targeted therapy, researchers showed that the rigidity of a substrate determines the T cell stimulation where softer substrates were shown to induce higher level secretion of cytokines important for T-cell activation (42). These mechanotransductive responses were partially attributed to changes in traction forces transduced resulting in actin reorganization. Another notable mention of force sensing and remodeling via actin reorganization is during cancer progression. When there exists a mechanical change in their native environment, cancer cells alter the force landscape of their microenvironment by sensing the physical space through focal adhesions. Subsequently, cancer cells collectively, through cell-cell junction communication, reorganize their actin cytoskeleton (43).

These and other mechanobiological investigations studying actin mechanics and the role it plays in cell functions, diseases, and development have asserted the importance of further studying how actin regulates cellular mechanics in more detail. The question remains, does classical biology render the best serving experimental platform to study the intricacies of actin-endowed cellular mechanics?

1.6 Steering clear from classical in vitro platform: towards minimal systems

Much of the works that revealed close to everything we know now about cellular machineries were done in vivo and in vitro-in cells. How actin assembles networks that regulates cellular mechanics, identifying ABPs and their specific interactions with actin and their role in cell function, and our fundamental understanding of everything else about actin emerged from in vitro-in cell studies. Yet, in vitro platforms are extremely difficult to control and modulate simply due to the fact that the cell is a complex bag of molecules. Even in an organism such as *c.*

elegans, empirical mapping of the protein-protein interactome of ~10,000 proteins revealed that there are ~116,000 protein interactions (46). This presents a great hurdle to investigate actin mechanics at a high resolution due to concurrently occurring processes in the cell system. It is also a significant challenge to isolate a particular cellular process or machinery from the rest of the cellular background, which, in human cells, is made up of products made by genes encoding ~20,000 proteins.

Although using bulk systems to study actin mechanics dates as far back as the early 1900s to study myosin contraction, in an effort to resolve the issue of complexity, in recent years, researchers have turned into advanced bulk experiments using purified proteins to modularly reconstitute elements of a cellular process and reverse engineer a functional system. Force generation by dendritic networks (47), network transformation through cooperativity of actin binding proteins (48) and studying actin excitable waves vital for cell division (49) are among the few that resorted to using bulk systems to study actin mechanics and dynamics. While the issue of eliminating complexity and gaining control and modularity was resolved through bulk experimental platforms, it is apparent that cellular processes in an unbounded substrate does not recapitulate and is not the same as cellular processes in confined spaces. The bottom-up reconstitution technique tackles this challenge through encapsulating cellular modules inside cell-sized confinement, commonly made of lipid bilayers mimicking the cell membrane (50–52).

Bottom-up reconstitution as an experimental platform to study cellular processes inside minimal cell models, techniques used to mechanically characterize minimal cell models, and method for generating minimal cell models will be described in detail in the following chapters.

1.7 Dissertation Outline

In the following chapters, I will describe mechanical characterization of actin networks. These characteristics comprise of responses of actin networks to changes in their physical environment (simulated microgravity and physical constrictions), network architecture using different ABPs and how different ABPs compete and cooperate, and finally, differential regulation of network deformability as a function of architecture. In Chapter 2, I introduce techniques to mechanically perturb cells and GUV-based minimal cell models and discuss the benefits and drawbacks of numerous methods including those I employed in following chapters. In Chapter 3, I investigate how actin networks respond to simulated microgravity and how this subsequently affects the elastic modulus of human osteoblast cells. Escaping the complexity of a living cell and gaining modular control in minimal cell mimics, in Chapter 4, I will leverage actin-encapsulating GUVs to study how two ABPs, fascin and Arp2/3 complex, compete and cooperate to assemble actin networks. In Chapter 5, I will investigate and demonstrate how actin architectures encapsulated inside GUVs differentially regulate the mechanics of the cell by measuring their electric field-induced deformation profile. Chapter 6 will introduce preliminary findings of how actin networks transform and rearrange when subject to micropipette aspiration. Finally, Chapter 7 will highlight and summarize takeaways from previous chapters and I will share some thoughts on future directions to deepen our understanding of actin networks and molecular mechanisms partaken in cellular functions.

Chapter 2 Methods to Mechanically Perturb and Characterize GUV-Based Minimal Cell Models

This chapter was published in Computational and Structural Biotechnology Journal (CSBJ) (2023). Author Contributions: N.H.W. and A.P.L. wrote the review.

2.1 Abstract

Cells shield organelles and the cytosol via an active boundary predominantly made of phospholipids and membrane proteins, yet allowing communication between the intracellular and extracellular environment. Micron-sized liposome compartments commonly known as giant unilamellar vesicles (GUVs) are used to model the cell membrane and encapsulate biological materials and processes in a cell-like confinement. In the field of bottom-up synthetic biology, many have utilized GUVs as substrates to study various biological processes such as protein-lipid interactions, cytoskeletal assembly, and dynamics of protein synthesis. Like cells, it is ideal that GUVs are also mechanically durable and able to stay intact when the inner and outer environment changes. As a result, studies have demonstrated approaches to tune the mechanical properties of GUVs by modulating membrane composition and lumenal material property. In this context, there have been many different methods developed to test the mechanical properties of GUVs. In this review, we will survey various perturbation techniques employed to mechanically characterize GUVs.

2.2 Introduction

Theoretical physicists date the formation of elementary particles back to 13.8 billion years ago after the Big Bang, following which these particles formed atoms and then molecules of various complexity. Somewhere between 13.8 billion years ago and now, various inanimate molecules, complex and simple, organic and inorganic, self-assembled to form a condition we call life. Biologists have studied numerous cellular components and pathways to understand life and how it came to be, however, due to intrinsic complexity of even the modest of life forms with few hundred genes, how molecules synergistically self-assemble and give rise to a complex self-replicating, metabolizing and evolving matter remains elusive to all. Nature has mastered creation and sustenance of life by the way of making it robust enough to thrive, and to be efficient, dynamic and durable to endure abrupt environmental changes; in cells, this requires machineries that can interact in extremely entangled web of networks, with auxiliary processes having complex and redundant cellular components to ensure that life thrives. This makes the dissection of cellular processes to understand how they self-organize to produce life an impractical feat.

Bottom-up reconstitution of a minimal cellular process inside a cell-mimicking environment has recently become a popular approach to understand the making of life from its non-living parts. The bottom-up approach seeks to assemble biology one part at a time and evolve the hierarchy of complexity to understand emergent behavior of cellular processes. A fair number of reviews over the years have illustrated the advantages, the aims, and novel findings from bottom-up assembly of cell models (53–61). Of the major challenges in reverse engineering a cell is creating a 3-dimensional, few micrometer-sized container that segregates the cytosolic lumen from the external environment. Thus, one of the initial tasks in bottom-up reconstitution

was to identify a confining substrate that closely mimics the function and chemical composition of the cell membrane. Among other protocell compartments such as droplets, coacervates enriched with charged molecules (62,63), capsules made of polymeric amphiphiles (including block copolymers and peptides) (64–67) and proteinosomes (68,69), GUVs made of lipid bilayers have been largely used to create a cell-sized (1-100 μm) confinement to encapsulate numerous cellular components. Like natural cell membranes, GUVs can be made from various compositions of lipids, mainly phospholipids and cholesterol, whose amphiphilic nature allow them to self-assemble into spherical compartments in an aqueous solution. Various methods have been developed to efficiently generate GUVs (70–72) and numerous review articles have described these methods (73).

Many in the field of synthetic biology resorted to using GUVs for encapsulation of minimal set of biomolecules, thereby disentangling a specific cellular phenomenon from the cytosol that is present in cells. Encapsulation of purified proteins in GUVs and synthesis of proteins in GUVs using transcription-translation (TX-TL) have been used to study cellular processes in a minimal artificial setting. Protocells reconstituting eukaryotic and prokaryotic cytoskeletal dynamics (74,75), communication through membrane pores of various kinds (76,77), and protein-induced membrane remodeling (78,79) are among notable GUV-based cell model studies over the years. Among these, many groups have made significant advances in the study of cytoskeletal dynamics and self-assembly (50). Characterization of actin architecture in confinement and mechanical characterization (75,80–83), microtubule-assisted GUV deformation (84) and FtsZ remodeling in response to loading (74) are examples among a large cohort of studies reconstituting cytoskeletal proteins. Mechanosensitive channels (76), toxin pores such as alpha hemolysin (85), and other membrane proteins have also been inserted into

GUV bilayers to recapitulate numerous cellular processes including mechanotransduction (76), inducible chemical reactions and proximity sensors (86). Furthermore, others have also taken on ambitious aims to realize cellular processes such as motility (87), division (88), and metabolism (89).

Cells are able to dynamically change their biophysical properties, particularly their mechanical characteristics, in response to environmental cues, in order to endure and thrive in different environments. Cells do this by changing their membrane composition, cytoskeletal organization, and cell shape, of which none are mutually independent. As simplified cell models, there is a large body of work characterizing biophysical properties of GUVs including GUV domain formation as a result of liquid-liquid lipid phase separation (90), GUV mechanics (91), permeability and electrical property (92). However, an overly simplified cell model like the GUV is not nearly as durable. Thus, many have taken on the challenge to modulate the mechanical property of GUVs. In this review, we will explore approaches used to alter the mechanical properties of GUVs and on techniques used to mechanically characterize GUVs.

2.3 Modulating GUV mechanics

Mechanical robustness and durability of cells is one of the key characteristics for cell survival in changing and hostile physical and chemical environments. Mechanical make-up of a cell is endowed by complex cytoplasmic content comprised of numerous proteins and a heavily reinforced membrane with diverse lipid and membrane protein composition. Unlike cells, inherently and by design, GUV-based minimal cell models are not complex enough to possess a robust mechanical profile for them to endure and survive harsh physical environments. However, recent advances have focused on enhancing the mechanical property of GUV-based minimal cell

models by changing luminal and membrane make-up of GUVs. The definitions of commonly characterized mechanical properties are summarized in Table 1. In this section, we will highlight and describe advances in improving mechanical durability of GUV-based minimal cell models.

2.3.1 Membrane modulation

Lipid bilayers are 2-dimensional fluids held by compressive forces from surrounding water molecules due to their attractive hydrogen bonding forces (93). Since lipid bilayers alone do not construct a versatile and durable boundary, cells mitigate this by utilizing different lipid compositions and membrane proteins. About half the surface area of the cell membrane is covered by proteins which reinforces membrane mechanics and shape by lowering membrane fluidity via restricting lateral diffusion in response to protein crowding (94,95). Unlike cells, bare GUV-based cell models are not naturally enriched with a diverse set of lipids and membrane proteins. Thus, GUVs are too fragile to endure perturbations in changing environments, consequently requiring delicate handling. However, studies have utilized and demonstrated different successful means to enhance the mechanical property of GUV bilayer membranes. One of the commonly used methods to modulate mechanical property of GUV lipid bilayer is by tuning the lipid composition. For example, Kato et al. revealed, using optical tweezers, that membrane rigidity can be enhanced by increasing acidic phospholipid content in GUVs (96). Furthermore, it was also shown that, using micropipette aspiration, different membrane sterols differentially regulate the compressibility modulus and lysis tension of membranes in GUVs (97). Others, using electrodeformation of GUVs, have demonstrated that cholesterol plays a lipid-specific differential role in regulating membrane bending rigidity (98). In this work, they showed that addition of cholesterol to DOPC vesicles results in little to no difference in bending

rigidity whereas addition of cholesterol to sphingomyelin vesicles reduces bending rigidity (98). Additionally, it was also found that bilayer asymmetry plays a role in GUV membrane rigidity due to changes in bending energetics resulted from how lipids with different spontaneous curvatures are distributed in a bilayer (99).

Additional to modulating membrane mechanics via tuning lipid content, another approach is to introduce external molecules such as proteins and polymers. For example, mechanical tests using micropipette aspiration of GUVs show that addition of membrane proteins Ca^{2+} ATPase into lipid bilayer of GUVs regulate membrane fluctuation and increase bending rigidity (100). Similarly, a recent investigation revealed the insertion of lactose permease into the GUV bilayer nonlinearly regulate membrane rigidity (101). Besides proteins, addition of other polymers can also alter GUV mechanics. For example, addition of block copolymers to lipid bilayer in GUVs greatly increases the stretching modulus (102).

2.3.2 Lumenal modulation

Cytoskeletal proteins self-assemble into complex and dynamic structures that endow the mechanical property of a cell (1). This equips cells with the ability to endure and survive mechanically and chemically changing environments, thus making them capable of migrating in extremely constricted spaces or bearing heavy loads. Cells achieve this not by simply being physically tough but also by being adaptive enough to change their physical property in response to the changing environment mainly via cytoskeletal reorganization triggered by mechanotransductive signaling. Unfortunately, bare GUVs are helpless against the slightest physical disturbance. Similar to tuning bilayer content, this encourages researchers to study how lumenal content regulate the mechanical property of the whole GUV.

There are numerous studies encapsulating different synthetic and biological molecules to regulate the mechanical property of GUVs. Among these, one work demonstrated that the presence of agarose in GUVs increases the viscoelastic property of GUVs by increasing relaxation time during electric field perturbation as compared to agarose-free GUVs (103). Others have also illustrated the role of other biopolymers in regulating deformation modes of GUVs subjected to osmotic shock (104). Towards understanding cytoskeletal networks in an isolated environment and equipping GUVs with cell-like mechanical characteristics, many have encapsulated cytoskeletal proteins inside GUVs. For example actin cortex has been shown to increase the compressibility modulus of GUVs compared with cortex-free GUVs (105). Similarly, GUVs encapsulating actin cortex subjected to electric field showed increased resistance to electroporation (106). Furthermore, we recently demonstrated that different actin architectures, particularly filaments, crosslink networks and cortex shells, differentially regulate GUV mechanics(81).

While identifying methods towards making robust GUVs will propel the field of bottom-up biology to create versatile cell models, it is equally important to understand and utilize methods and techniques that allow us to manipulate and perturb GUVs to better understand their physical properties.

2.4 Methods to perturb GUV-based cell models

In order to extract quantities that will inform us about mechanical properties, GUV-based cell models must be subjected to a perturbation that results in deformation. The resulting deformation profile with respect to the perturbing load (stress) allows us to obtain various mechanical characteristics. Several methods have been developed to perturb GUVs and here, we

will describe some of the principal methods that have been applied to mechanically characterize GUVs. Almost all of these methods were initially designed for mechanical characterization of cells. The mechanical property of a cell is intimately linked to a myriad of its pathological and developmental states, and thus can be used as indicators of hematologic diseases, cancer progression and metastasis, and cardiovascular health. This incentivized the development of various force application techniques to measure Young's modulus, viscous response, and membrane bending rigidity of the whole cell and cell components such as the cytoskeleton and the membrane. These techniques have been repurposed and applied to mechanically characterize GUV-based protocells.

2.4.1 Micropipette aspiration

The predecessor of what we now call micropipette aspiration, then referred to as "sucker" or "cell elastimeter", was developed in the early 30s as described by Vles (107) and further modified in the early 50s by Mitchison and Swann in its application to investigate membrane properties of sea-urchin eggs (108). Over the following years, the set up morphed to its most familiar and current version by notable efforts from Rand and Burton (109) and Evans and Hochmuth (110). Micropipette's ability to seamlessly apply well controlled and defined stresses onto cell-sized samples has made it among one of the most popular mechanical perturbation methods towards material characterization of a cell and extracted nuclei. Young's modulus of cells (considered as homogenous solids), surface tension, and viscous properties for creep profiles are among the mechanical properties measured by using micropipette aspiration. Principally, micropipette aspiration applies negative pressure (aspirating) to single cells/GUVs suctioning them into a parallel-walled capillary of diameter smaller than the sample (Fig 2-1A). Although there are various designs of micropipette aspiration setup over the years depending on

researchers' preference, the setup generally comprises of a custom-prepared glass capillary pipette, a pipette holder, a reservoir for pressure control and a pressure controller of some sort. Briefly, pipettes are pulled commonly using a pipette puller and further cut using a microforge to the desired diameter at the pipette mouth. For GUV aspiration, pipette inner diameters in the range of 2-10 μm are typically used. Pipettes are surface-coated to minimize sample adherence and friction using reagents such as BSA. Manipulation of pipette to selectively aspirate on an isolated sample is done via a micromanipulator onto which a micropipette holder is mounted. In earlier days of micropipette aspiration development, negative aspiration pressure was attained by adjusting height of a reservoir inducing a change in hydrostatic pressure. However in recent years, high precision pressure controllers can replace water columns to apply high resolution and stable pressure points (111). The micropipette aspiration setup is typically installed on an inverted microscope mounted on a vibration isolation table.

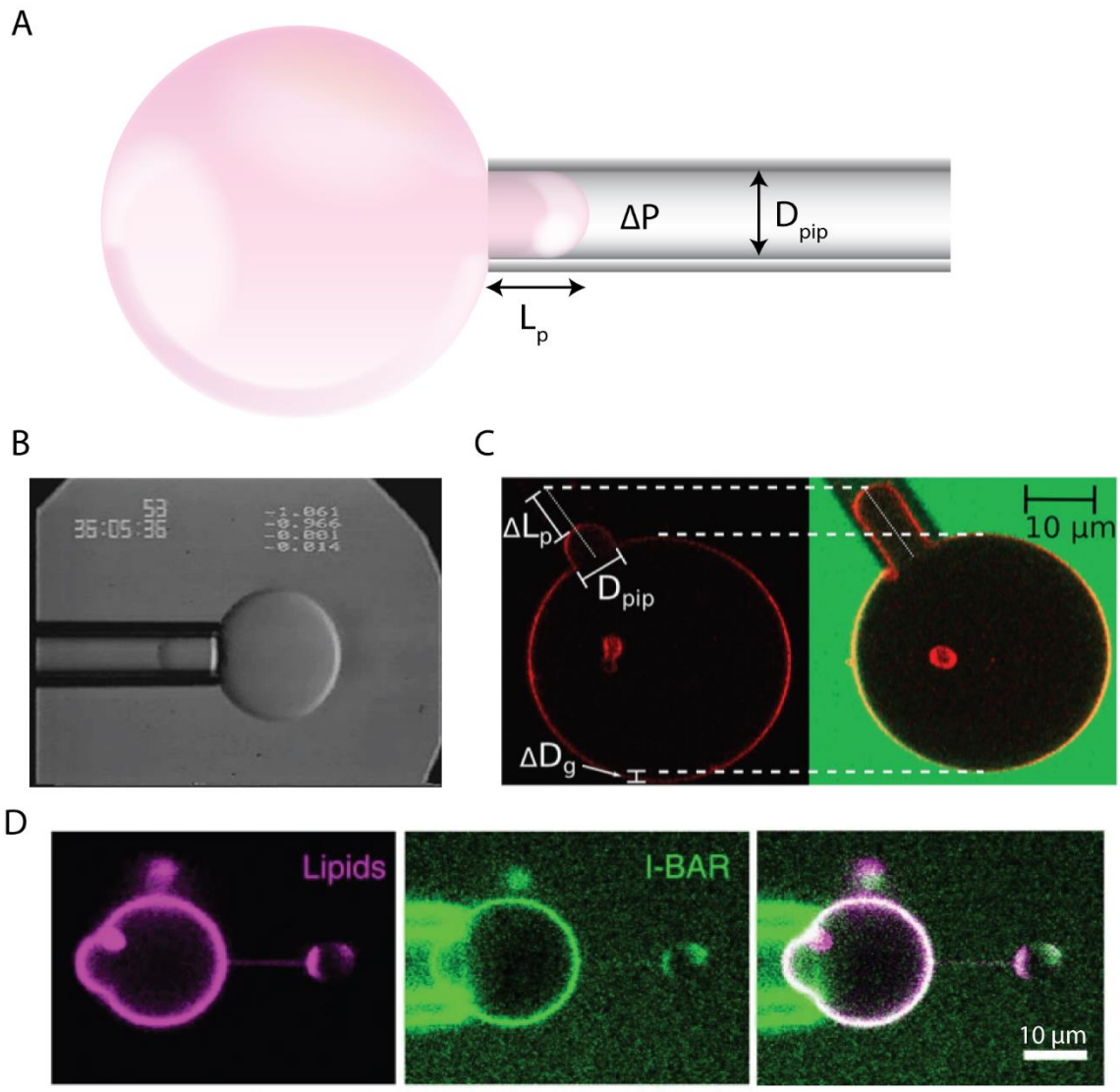

Figure 2-1 Micropipette aspiration of GUVs

(A) Schematic representation of a micropipette capillary aspirating on a GUV. ΔP is the pressure difference between ambient pressure outside of the pipette and pressure inside the pipette. D_{pip} is the diameter of the pipette and L_p is the protrusion length of GUV at ΔP. (B) Representative brightfield image of an aspirated GUV to measure elastic area expansivity modulus. (C) Aspirated GUV with fluorescently labeled lipid bilayer (red) under iso-osmotic condition (left) and GUV immersed in a hyperosmotic buffer containing carboxyfluorescein (green) with a larger aspirated protrusion length (right). (D) Relationship between GUV and membrane curvature

sensing protein (I-BAR) by modulating membrane tension using micropipette aspiration and optical tweezers for measure aspiration force and pulling membrane nanotubes, respectively. Panels B, C, D are adapted from (112), (113), and (114), respectively.

Since the 1980s, numerous micropipette aspiration studies have been conducted to measure material properties of model membrane. Elastic properties such as bending rigidity, area expansion and tensile strength of GUVs with different bilayer compositions (Fig. 2-1B) (56,57,112,115–117), role of increasing membrane tension and membrane curvature in lipid domain formation (118,119), thermomechanical properties (120) and viscous properties of GUVs with gel phase bilayers (121) are among the notable works. In addition to characterization of bare GUVs, other studies have also used micropipette aspiration to study various aspects of GUV cell models. These include studies of characterizing the hydraulic conductivity of membrane water channel permeability (Fig. 2-1C) (113) and identifying membrane curvature sensing proteins (Fig. 2-1D) (114). Later developments have combined micropipette aspiration with other perturbation setups. For example, micropipette aspiration combined with optical tweezers provides the ability to induce high membrane curvatures while controlling of GUV membrane tension (122) and has been used to acquire precise measurements of membrane tension (123) and protein clustering (114). Although a powerful tool to manipulate and apply load to GUVs, limitations such as low measurement yield, setup complexity requiring expertise and specialized equipment to prepare capillaries remain a challenge.

2.4.2 Atomic force microscopy

Successor to the scanning tunneling microscope (STM), a Nobel Prize winning invention for profiling surface topology at the atomic scale, atomic force microscopy (AFM) replaces the

current tunneling tip of STM with a force sensing cantilever (124). The original invention of the AFM was to correct critical surface imaging limitations of the STM, which was restricted to electrically conductive metals and semi-conductors. However, its ability to apply and sense forces as low as a few piconewtons allowed scientists to repurpose AFM for measuring physical properties of biological samples.

In principle, AFM is an elastography instrument that uses a cantilever of specific spring constant with a microscale indentation probe at the tip (Fig. 2-2A). Typically, conical silicon indentation tips are commonly used for indentation experiments, however, spherical geometries using glass tips and no tip (used for compression as opposed to indentation) have been frequently used. AFM is equipped with a laser reflecting off the back of the cantilever tip and a photodiode detects shifts of the reflected laser. These shifts enable the precise measurement of cantilever deflection as it comes to contact with a sample. A piezoelectric driver moves the cantilever towards immobile biological samples (adherent cells or substrate-immobilized suspension samples), thereby applying stress resulting in the indentation of the sample and deflection of the cantilever. Given that the cantilever has a known and calibrated spring constant, the detected cantilever deflection is then used to determine the precise loading force by the indenter. This results in a force-indentation curve that can be converted to a stress-strain curve.

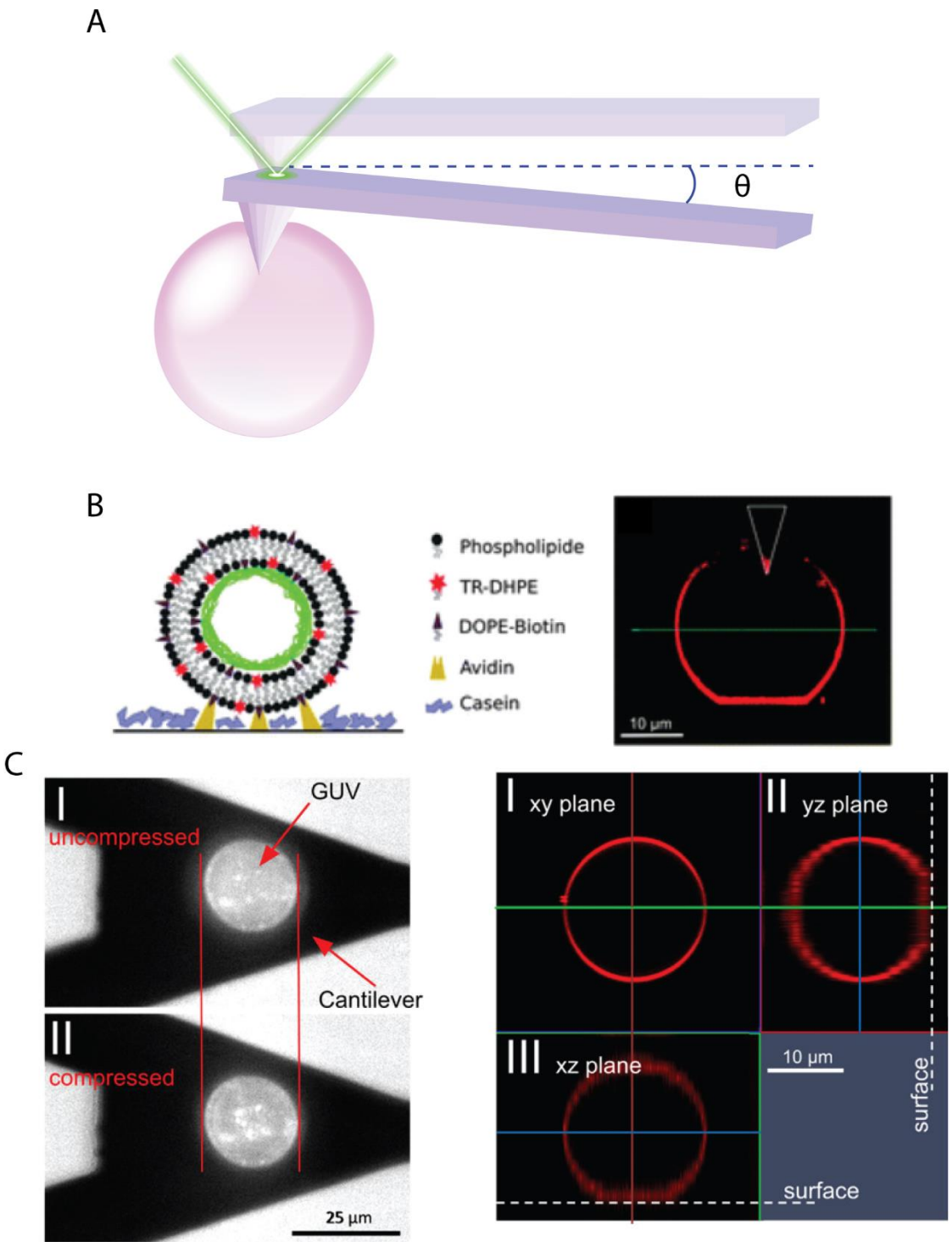

Figure 2-2 AFM indentation of GUVs (A) Schematic representation of AFM indentation of a GUV. Laser light reflecting from tip of the cantilever is used to measure deflection, θ, of cantilever in response to GUV indentation. (B) Actin cortex encapsulating GUVs immobilized

via biotin-avidin linkage subjected to AFM indentation using a conical tip to measure compressibility modulus and pre-stress membrane tension. (C) Compression of actin cortex encapsulating GUVs using tip-less cantilever. Similar to (B), parallel plate compression using AFM is used to extract physical properties of actin cortex GUVs including compressibility modulus and membrane tension. Panels B and C are adapted from (125) and (105), respectively.

Numerous studies have used AFM to characterize mechanical variability among cell types from bacteriophage (126) to eukaryotic cells (127–130), detect disease progression such as cancer metastasis (54,131,132), identify the mechanical topology of cytoskeletal networks (133,134), study viscoelasticity of the cell membrane (135,136), and to investigate dynamic mechanical properties of protein complexes (47,137). Given its ubiquitous use in biophysics, AFM can easily be adopted to study GUV mechanics. However, as of yet, mechanical studies of GUV-based and other cell models using AFM remain largely underutilized. Studies investigating GUV membrane tension and area compressibility modulus using conical indenters (Fig. 2-2B) (125), and measurement of the bending rigidity of DPPC liposomes (58) are among the few works using AFM to mechanically characterize GUV cell models. Additionally, using a modified AFM with tip-less cantilever, Schaefer et al. investigated area compressibility modulus of GUVs with and without reconstituted actin shells and found that actin shells significantly stiffen GUV membrane with up to 10-fold increase in compressibility modulus from 0.12 N/m (actin-free DOPC GUV) to 1.25 N/m (actin-shell GUVs) (Fig. 2-2C) (105). Although AFM can be implemented for GUV mechanical studies, limitation such as complexity of setup, prone to noise, requirement of substrate adhered samples and extended measurement time are worth noting.

2.4.3 Acoustic Manipulation

Acoustic perturbation is a field gradient perturbation approach used in numerous cell manipulation experiments as the preferred non-invasive perturbation technique with high precision. One of the early works implementing acoustic waves to cells was conducted in the early 70s by Dyson et al. on blood circulation where they observed “arranged” red blood cell aggregates (138). Alignment and separation of red blood cells was further investigated and attributed to standing waves induced by ultrasound by Baker the following year (139). Following these seminal works, commonly integrated with microfluidic devices, acoustic perturbation has been used for cell manipulation studies including patterning for tissue engineering (140,141), trapping for single cell analysis (142–144), sorting specific cell types from a heterogeneous population (145–147), and single cell mechanical testing (148–151).

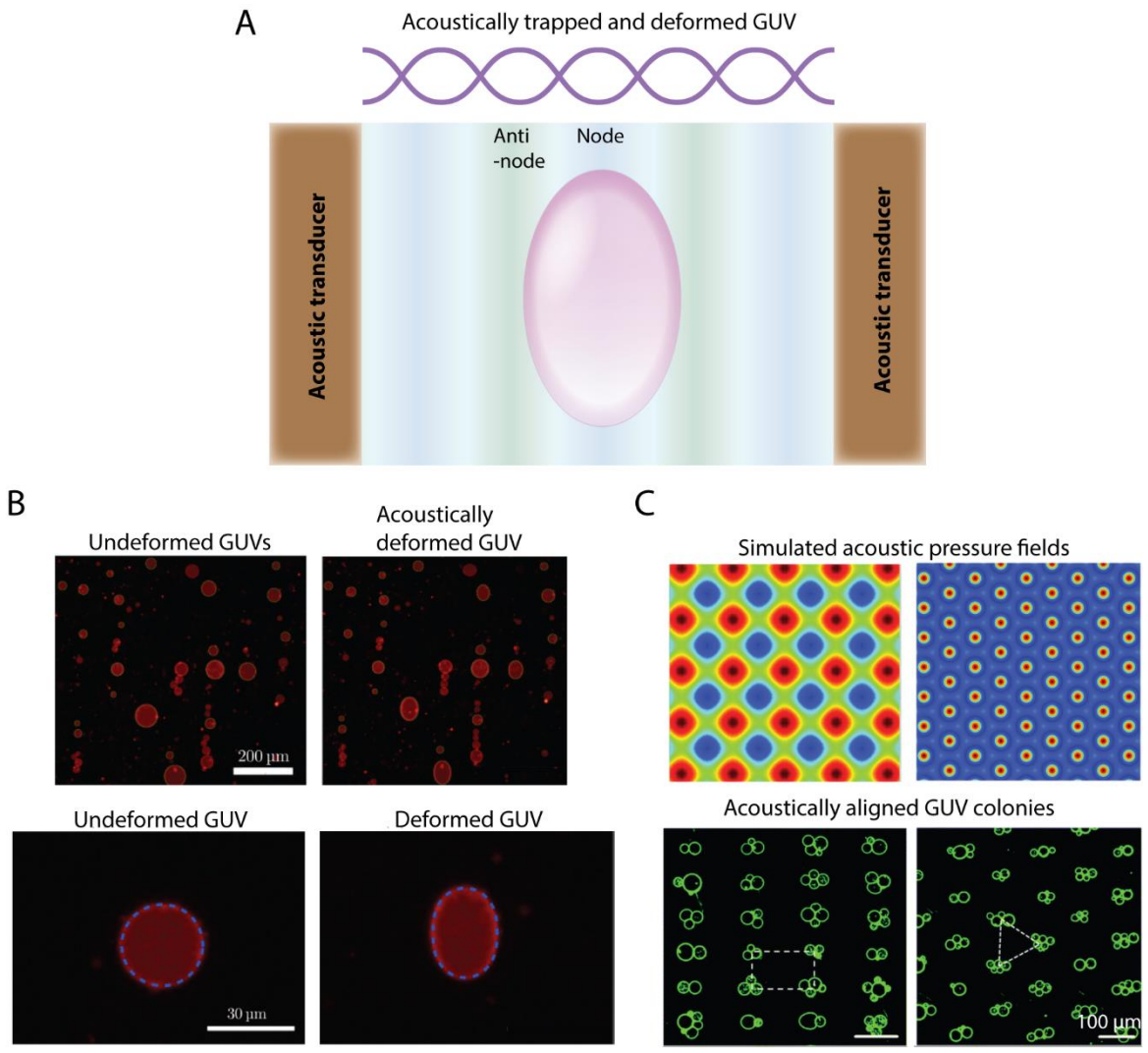

Figure 2-3 GUV manipulation via acoustic radiation (A) Schematic representation of an acoustically deformed GUV. A pair of piezo transducers operated at identical frequency are used to create standing waves generating pressure fields of nodes and anti-nodes in the GUV-containing solution. (B) Acoustic radiation used to mechanically deform GUVs. Membrane elasticity and other physical properties are obtained using acoustic radiation-induced GUV deformation. (C) Precise control of pressure field in GUV-containing solution allow the formation of aligned GUV colony formation. Chemical interaction between GUVs and GUV-cells are studied using acoustic manipulation/alignment of GUVs and cells. Panels B and C are

adapted from (152) and (153), respectively.

A sound source induces acoustic radiation force creating a time-averaged pressure field deviating from the local ambient static pressure due to velocity change in the medium. An acoustic device for cell or GUV manipulation leverages this characteristic to generate standing waves by using two opposing and identical acoustic waves (Fig. 2-3A). At a given frequency and acoustic intensity, a stable and steady pressure field is created with high pressure nodes (antinodes) and zero-pressure nodes simply referred to as nodes (Fig. 2-3A). Particles like cells, with a positive acoustic contrast factor, are driven by the acoustic radiation to localize at the nodes of the pressure field away from the antinodes. Theoretically, the node is a single point and thus a 3-dimensional particle suspended in the pressure field will be subjected to some level of radiation force and this can result in deformation of cells and GUVs. There mainly exist two different types of acoustic manipulation platforms utilized in perturbation of biological samples and these are surface acoustic waves (SAWs) and bulk acoustic waves (BAWs). SAWs are used to induce acoustic waves that are spatially specific to perturb a thin layer of liquid at the surface of the substrate. Interdigital transducers (IDTs) are used to drive a piezoelectric substrate, commonly lithium niobate, to transmit acoustic waves resulting in radiation capable of creating a pressure field to a thin layer of fluid dispensed on top of the piezo substrate (151,154,155). BAWs on the other hand are transmitted through the sample medium. Commonly, for standing BAW, two piezo transducers or one piezo transducer and a reflector, are arranged with a space in between where the sample solution will be dispensed. Driven by a function generator, acoustic waves will be transmitted through the solution resulting in a pressure field with stable nodes and antinodes.

Although there is not a large body of work implementing acoustic radiation to perturb GUV-based minimal cell models, some studies have used this platform to perturb and manipulate GUVs in order to study chemical signaling between GUVs and red blood cells (156), characterize membrane elasticity (Fig. 2-3B) (152), and spatially align GUV colonies (Fig. 2-3C) (153). Unlike cells, some minimal cell models, either GUV-based, condensates or otherwise, can be delicate and easily perturbed by contact-based and invasive perturbation methods. Thus, remote perturbation techniques such as acoustic manipulation can be of great benefit for characterization and manipulation of cell models. Furthermore, with the fast-growing field of synthetic biology where structurally and biochemically complex cell models are developed, the use of acoustic perturbation for characterization and perturbation of minimal cell models will be of great utility. For GUV-based cell models, which are not as robust as cells, remote manipulation and perturbation render a useful platform for mechanical studies. However, lack of spatial resolution for high precision control remains a limitation of acoustic manipulation devices.

2.4.4 Optical stretching

In the mid-80s, we learned from Ashkin et al. that the momentum of a gradient laser light with a point focus is capable of trapping particles with sizes ranging from micrometers to atomic scales in 3 dimensions (157,158). Using this method, for the first time, visible argon-laser light was used to trap viruses and bacteria (157). Through the years, optical tweezers have been deemed one of the crucial methods for manipulations of cells and sub-cellular biological materials. In 2000, Guck et al. demonstrated that optical tweezers can be transformed into optical stretchers using identical opposing laser gradients that are capable of stretching/deforming biological samples (159). Over the following years, optical stretchers were extensively used for

mechanical characterization of cells. Mechanical properties of eukaryotic cells (160,161) , differential mechanical properties of cells in response to drug treatment (162), differential mechanics of healthy and metastatic cancer cells (163,164) have been studied using optical stretchers.

Stretching principles of optical stretchers are similar to the trapping mechanism of optical tweezers. When an unfocused gradient laser light passes through a transparent material with a different refractive index compared to the native external environment, take a cell for example in a solution, light will change its path and gain momentum which will be transferred to the material as a scattering force that propels the cells in the direction of light path. Having two identical and opposing gradient laser lights, opposing propulsion of a cell will result in stretching of cell/GUV (Fig. 2-4A) (159). Unlike single beam optical tweezers which require focusing for 3-dimensional trapping of samples, double beam optical stretchers do not require focusing thereby minimizing damage of biological samples from high intensity lasers (159,165). For mechanical characterization of biological materials, optical stretchers are often integrated with microfluidic devices in order to easily focus and deliver samples to the trapping/stretching region (166–168).

In recent years, optical stretchers have been utilized for mechanical perturbation of GUV cell models. Among these, dual beam optical stretchers integrated into a microfluidic device have been used to study elastic constants (169) and bending modulus of GUVs (Fig. 2-4B) (170). Viscoelastic properties of GUVs have also been investigated using optical stretchers (Fig. 2-4C) (171). Others also have investigated lipid oxidation in GUVs in response to optical stretcher-induced change in membrane tension (172). Beyond direct mechanical characterization of optical tweezers to perturb GUVs, they have also been used together with micropipette aspiration

approach to modulate membrane tension (122,123). Over the years, many of the limitations of optical stretchers, such as laser-induced damage, have been improved, yet the effect of heat and laser-induced damages on GUVs and GUV-encapsulated proteins, especially during extended perturbation periods, remain an unresolved issue.

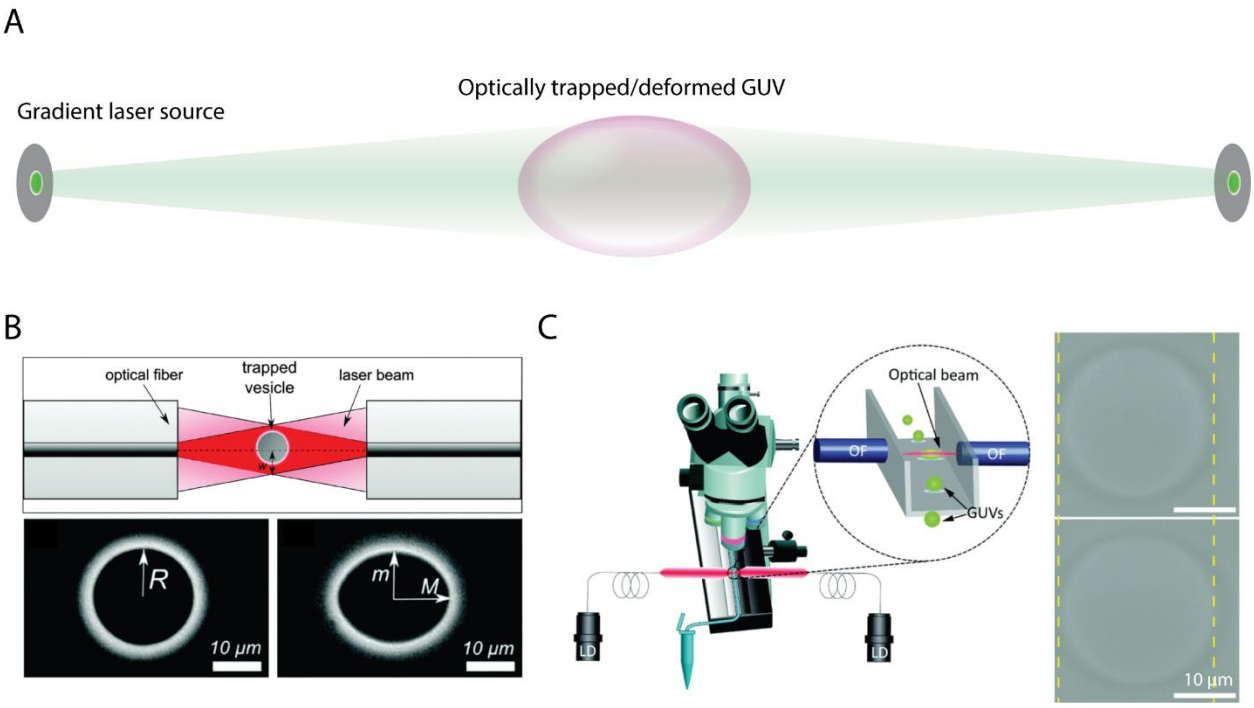

Figure 2-4 Optical stretching of GUVs (A) Schematic representation of an optically stretched GUV. Two opposing and identical gradient laser sources beam lasers on a GUV. Opposing light momentum results in the stretching of the GUV. (B) Optical trapping and stretching of GUVs to study elastic property of GUVs and the effect of generated heat from absorbed laser on GUV deformability. (C) Characterization of GUV bilayer viscoelastic properties. Stretching time constants in the slow stretching regime (elastic regime) are measured from optically stretched GUVs to characterize their viscoelastic properties. Panels B and C are adapted from (169) and (171), respectively.

2.4.5 Electrical perturbation

Initial use of electrical pulses to perturb single cells dates as far as the mid 20th century where researchers observed motile responses of sperm cells (173) and aggregation of red blood cells (174). However, the revolutionary use of electric fields to permeabilize the membrane, thus allowing access to the cytoplasm, was realized after seminal studies from Sale and Hamilton demonstrating cellular lysis when high energy electric pulses were applied (175,176). With further control and modulation, non-lethal access to the cell cytosol via electropermeabilization enabled technologies such as delivery of molecules for therapeutic purposes (177–179) and transfection (180–182). The use of electroperturbation to mechanically characterize cells began in the early 80s with studies showing deformability of red blood cells in response to electric fields (183) and studies measuring elastic modulus of blood cells (184). Over the following decades, advanced and integrated variation of electroperturbation devices were used to mechanically characterize cells (185–189). Although a facile approach to perturb single cells, complexity and variability of cells, which consequently result in variable electrical properties, such as membrane dielectric constant and cytosolic conductivity, has made identifying a universally reliable mathematical model describing the influence of electric field to cell's mechanical property a difficult feat.

Easy to make, cheap and customizable aspects of the electroperturbation setup make it attractive as a facile method for mechanical characterization of biological samples. Essentially, the setup comprises a chamber with parallel electrode walls into which samples are dispensed in, a function generator, a microscope and an image acquisition system. Copper tapes or platinum wires can be used to make the chamber with a known distance between two electrodes for precise control of electric field (190). Depending on the aim of the experiments, both AC and DC electric fields have been applied in numerous studies. AC fields induce steady, frequency

dependent, elliptical deformation of GUVs and are largely used to measure properties including membrane bending rigidity, membrane capacitance (191), and area dilation (192). DC fields, on the other hand, due to the high intensity pulses that can be induced, have been widely used to induce electroporation with aims to investigate membrane rheological dynamics and stability (193,194).

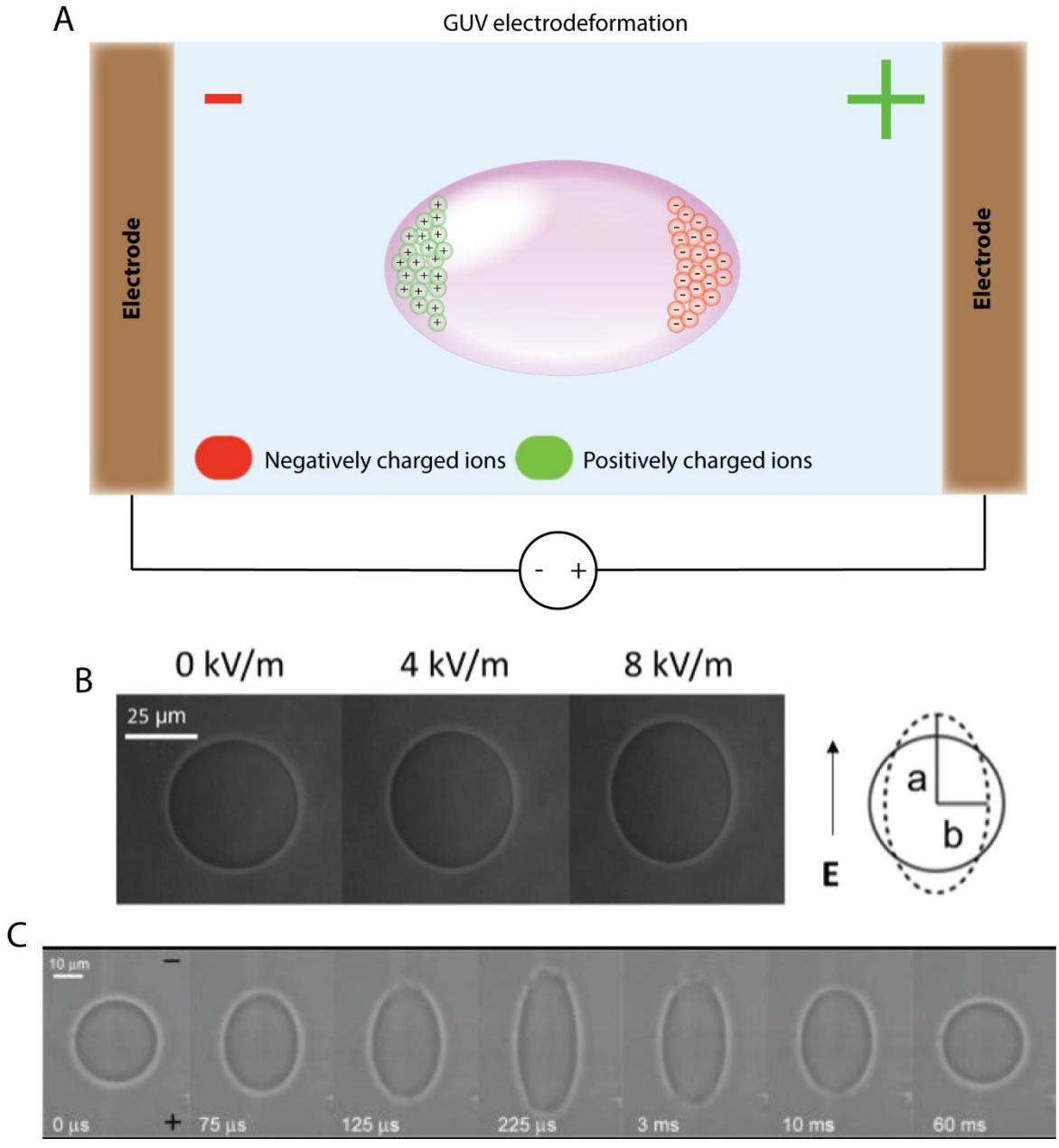

Figure 2-5 Electrodeformation of GUVs (A) Schematic representation of an electrodeformed GUV. Two parallel electrodes connected to a voltage source induce an electric field across a conductive GUV-containing solution. Charged ions inside GUV separate towards the opposing sides of the electrodes. This charge separation results in the deformation of GUVs. (B) Elliptical deformation of a GUV in response to an AC electric field. Deformation profiles of GUVs are used to measure membrane bending rigidity and membrane capacitance. (C) Electrodeformation of GUVs using DC pulses. Dynamic response of GUVs to electric field, including elliptical deformation and poration are captured at high temporal resolution. These dynamic responses are used to measure the critical transmembrane potential of GUV lipid bilayer. Panels B and C are adapted from (191) and (193), respectively.

Unlike other perturbation methods that operate by applying stresses either through contact or propagation via a medium that does not depend on inherent property of the sample itself, electroperturbation leverages unique properties of lipid bilayers in biological samples. Lipid bilayers create a physical insulating barrier between the cytosol and the outer environment, thereby permitting separation of charges of molecules and ions (Fig. 2-5A), which is the critical mechanism by which stresses are induced to result in electromechanical deformation of biological samples. Expectedly, this sparked researchers' interest to study electromechanical response of lipid bilayers in a cell-like environment, thus encouraging membrane biophysicists to use GUV-based cell models to study lipid bilayers of various compositions. Critical membrane voltage as a function of cholesterol in the lipid composition (195) to characterize membrane stability and permeabilization (196), characterization of membrane viscoelasticity (197), membrane bending rigidity (98) and capacitance (Fig. 2-5B) (191), and high resolution

deformability dynamics of GUVs (Fig. 2-5C) (193) are among notable works using GUV cell models for electromechanical characterization of lipid bilayers. Beyond mechanical characterization of GUVs, electroperturbation has been used for electromechanical characterization of polymer-based cell model microcapsules (198–200). Although the majority of studies using electrodeformation of cell models are directed at towards understanding membrane properties, the setup can be of great utility for characterization of cellular mechanics by reconstituted cytoskeleton networks. Recent studies have utilized electroperturbation to investigate the relaxation time and electrically induced pore resealing time showing that actin-cortex GUV pores seal in minutes while actin-free GUV pores seal in ~1 ms post poration (106). Additionally, differential regulation of GUV mechanics via different actin architectures was investigated by measuring deformability indicating ~25% deformation dampening by actin network encapsulating GUVs versus actin-free GUVs (81).

2.4.6 Microfluidic devices

Unlike the above perturbation methods, there are numerous microfluidic designs manipulating biological samples in different ways. Some utilize solely fluidic flow inside microfluidic flow channels to manipulate cells, or solid features at the micron-scale and some, often the case with most microfluidic devices, are integrated with other perturbation techniques as discussed earlier. Among studies using flow-dependent microfluidic devices for mechanical characterization include pneumatically controlled single cell compression microfluidic device to measure Young's modulus (201) and study biochemical responses to compressive forces (202), microfluidic micropipette aspiration devices for measuring cellular stiffness (203,204), microfluidic sorting devices for stiffness-based cell sorting (205,206), and constriction-based devices for single cell mechanical characterization (207,208). Microfluidic platforms can be

integrated with optical momentum (168), acoustic radiation (209), electric fields (210), or magnetic forces (211) to manipulate cells.

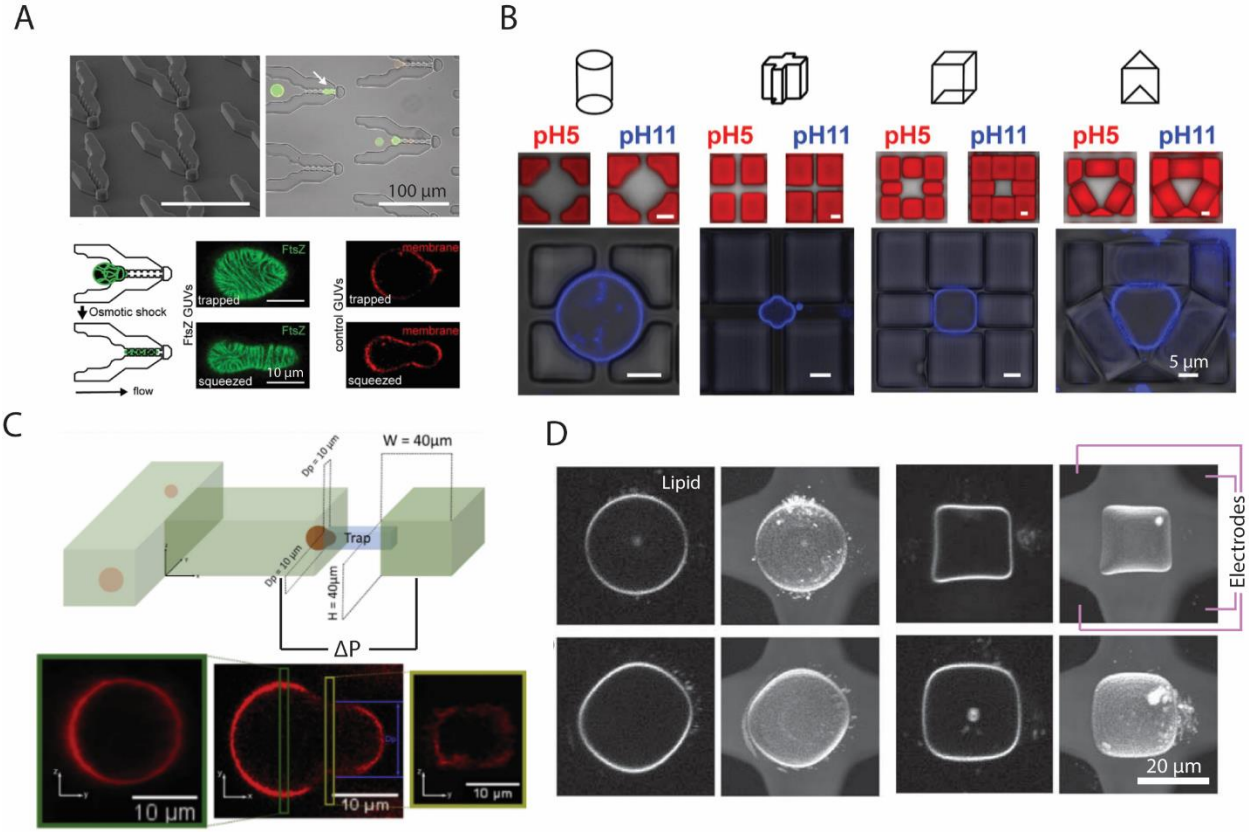

Figure 2-6 Microfluidic manipulation of GUV (A) FtsZ-encapsulating GUVs trapped and deformed using a microfluidic device (top). Modulating the osmotic condition of the GUV solution changes GUV deformation and FtsZ organization (bottom). (B) A chemically tunable microfluidic device is used to trap and shape GUVs. Different trapping designs are used to tarp GUVs. Increasing solution pH results in swelling of trapping features, thus deforming the GUVs to specific shapes. (C) Implementation of micropipette aspiration in a microfluidic device. GUVs are trapped and aspirated in to a microchannel. Changing the flow rate inside the microfluidic channel results in change in aspiration pressure ΔP. (D) Integrated microfluidic device with electric field cages trap deform and reorient GUVs. Panels A, B, C, and D are adapted from (74),

(212), (213), and (214), respectively.

Microfluidic devices, both flow-based and integrated, have also been frequently applied to perturb GUV-based minimal cell models. Notably, Ganzinger et al. developed a microfluidic device capable of trapping and deforming FtsZ network encapsulating GUVs (Fig. 2-6A) (74). Using this device, they studied the remodeling modes of cytoskeletal network in response to constriction-induced deformation (74). Others have utilized microfluidic devices for shaping GUVs using pH inducible microfluidic wells (Fig. 2-6B) (212), and for studying membrane biophysics using microfluidic micropipette aspiration device (Fig. 2-6C) (213). Integrating electric fields to microfluidics, Korlach et al. used dielectrophoretic field cages for deforming and reorienting GUVs (Fig. 2-6D) (214). Others have creatively implemented microfluidic design principles for single GUV trapping (215), measuring GUV membrane permeability (216), and trapping and filtering devices for GUV-GUV communication studies and synthetic tissue formation by facilitating colony formation (217). In Table 2, we have provided example studies that measured GUV mechanical properties by using various methods discussed in the sections above.

2.4.7 Additional perturbation methods

Numerous other methods are used to perturb GUV-based minimal cell models. These approaches can be standalone methods or integrated with those discussed in previous sections. To list a few, for instance, magnetic beads have been used to pull membrane tubes with piconewton scale forces from micropipette-aspirated GUVs (218). Furthermore, magnetic beads have been used to manipulate GUVs for trapping (219) and magnetic microrheometry was used to deform actin-encapsulating GUVs to measure viscoelastic relaxation modulus (220). Similar

to magnetic beads, encapsulated Janus particles have also been used to perturb GUVs to study membrane structural integrity (221). Numerous other works have used various nanoparticles to generate GUV deformation and poration to study membrane integrity and fluidity (222–224). Other GUV perturbation methods leverage controlling the native environment GUVs are dispersed in. These include changing the osmotic environment, regulating the surrounding temperature and the adhesive property of substrates onto which GUVs settle. For example, one study revealed the pulsatile property of bilayers by subjecting GUVs to hypotonic condition resulting in a swell-burst cycle (225). Others have leveraged such a simple mechanism to study oscillatory lipid-lipid phase separation driven by differential membrane tension (226). Furthermore, deformation modes of actin-reinforced GUVs were studied by changing osmotic gradient (227). Additionally, thermal fluctuation of the GUV environment has also been widely used to characterize different biophysical properties of GUVs. Among the large cohort of studies, regulating GUV morphology (228) and temperature-regulated lipid phase separation and miscibility are notable (229).

2.5 Summary and Outlook

Initially, GUVs were ubiquitously used as a model membrane system with control of membrane content. Recently, with the growth of bottom-up synthetic biology, GUVs were utilized as an ideal substrate for the creation of a synthetic cell-like system using biological parts. Perhaps, with the collective effort of scientists using GUVs to understand cellular mechanisms and creating synthetic systems, creating minimal life-form from non-living parts may be realized. Regardless, towards creating life or simply using them as model systems to understand cellular functions, GUV-based minimal cell models must be mechanically robust and their mechanical

characteristics be extensively characterized. Without further reinforcement, GUVs are just simply unfit to endure and survive the physiochemical environment native to cells and attempting to understand a cell outside of its biological environment will make the study incomplete. Thus, it is imperative to make all attempts to equip GUVs with the mechanical robustness and durability akin to that of cells. While we have yet to make a sturdy cell-like biological compartment with a boundary as versatile as the cell membrane, remarkable advances have been made to make GUV-based cell models more mechanically robust. Developing new techniques for effective mechanical characterization of GUV-based cell models is essential and innovative approaches for high precision, high resolution cell model manipulation will propel the field of synthetic biology and cell biology in general.

Table 1 List of GUV mechanical properties and their definition

Mechanical Property	**Definition**
Young's modulus	A physical quantity that measures the general stiffness of elastic solids. Generally not a quantity used to characterize GUVs.
Bending rigidity	Physical quantity that measures resistance of an elastic material to changing its curvature. Membrane bending rigidity is one of the commonly measured GUV physical quantities.
Area expansion modulus/stretching modulus	Under tensile stress, an elastic material can expand to failure. Area expansion modulus measures the resistance of an object to expand/stretch under load. In GUVs, area expansion modulus measures how GUV bilayers withstand area expansion.
Membrane tension	Membrane tension is a state property measuring the force per area acting on a membrane cross-section. For GUVs, different approaches

	can be used to either measure membrane tension of GUV bilayer at an unperturbed state or to modulate membrane tension.
Viscoelasticity	Like most biological materials, GUVs exhibit both elastic and viscous properties. Viscoelasticity measures time dependent behavior of a material by measuring loss modulus from the relaxation curve during loading and unloading phases of the material.
Area compressibility modulus	This is the same as area expansion modulus when the load is compressive
Deformability	In GUVs, deformation modes are often elliptical. Deformability measures how much elliptically deformed GUVs deviate from a unit circle by calculating the ratio of major axis to minor axis.

Table 2 Methods of GUV perturbations and some of the measured mechanical properties

Method	**Measured mechanical property**
Micropipette aspiration	Area expansion modulus (ref. 65) Bending rigidity (Ref. 4,62) Membrane tension (Ref. 5)
Atomic force microscopy	Area compressibility modulus (Re. 88) Bending rigidity (Ref. 6)
Acoustic manipulation	Deformability (Ref. 106) Membrane Young's modulus (Ref. 106)
Optical stretching	Viscoelasticity (Re.122) Bending rigidity (Ref. 121,120)

	Membrane tension (Ref. 120)
Electrical perturbation	Deformability (Ref. 144) Viscoelasticity (Ref. 148) Membrane bending rigidity (Ref. 47)
Microfluidic devices	Deformability (Ref. 22, 163) Stretching modulus (Ref. 164)

2.6 Acknowledgments

The work is supported by the National Science Foundation (CBET-1844132). N.H.W. was supported by NIH's Microfluidics in the Biomedical Sciences Training Program (NIH NIBIB T32 EB005582). A.P.L. acknowledges support from National Institutes of Health (R01 EB030031) and National Science Foundation (EF1935265 and MCB220136).

Chapter 3 Simulating Microgravity using a Random Positioning Machine for Inducing Cellular Responses to Mechanotransduction in Human Osteoblasts

This chapter was published in Review of Scientific Instruments (RSI) (2021). Author contributions: N.H.W. and A.P.L. designed research. H.A., R.K., M.R., and T.T. designed and built RPM. N.H.W. and E.A.M. performed experimental research. N.H.W., E.A.M., and M.N. analyzed data. N.H.W., E.A.M., B.G. and A.P.L. wrote the paper.

3.1 Abstract

The mechanotransduction pathways that mediate cellular responses to contact forces are better understood than those that mediate response to distance forces, especially the force of gravity. Removing or reducing gravity for significant periods of time involves either sending samples to space, inducing diamagnetic levitation with high magnetic fields, or continually reorienting samples for a period, all in a manner that supports cell culturing. Undesired secondary effects due to high magnetic fields or shear forces associated with fluid flow while reorienting must be considered in the design of ground-based devices. We have developed a lab-friendly and compact random positioning machine (RPM) that fits in a standard tissue culture incubator. Using a two-axis gimbal, it continually reorients samples in a manner that produces an equal likelihood that all possible orientations are visited. We contribute a new control algorithm by which the distribution of probabilities over all possible orientations is completely uniform. Rather than randomly varying gimbal axis speed and/or direction as in previous algorithms

(which produces non-uniform probability distributions of orientation), we use inverse kinematics to follow a trajectory with a probability distribution of orientations that is uniform by construction. Over a time period of 6 hours of operation using our RPM, the average gravity is within 0.00123% of the gravity of earth. Shear forces are minimized by limiting the angular speed of both gimbal motors to under 42 deg/s. We demonstrate the utility of our RPM by investigating the effects of simulated microgravity on adherent human osteoblasts immediately after retrieving samples from our RPM. Cytoskeletal disruption and cell shape changes were observed relative to samples cultured in a 1-*g* environment. We also found that subjecting human osteoblasts in suspension to simulated microgravity resulted in less filamentous actin and lower cell stiffness.

3.2 Introduction

Past studies have shown how genetic and soluble chemical factors play a role in dictating cellular functions, yet physical forces are also potent epigenetic regulators of diverse cellular processes including proliferation (230–232), differentiation (233–235) and disease progression (236,237). It is now well appreciated that cells respond to different physical forces: stress affects bone formation (238–241), mechanosensitive channels are activated by elevated membrane tension (242–245), and differentiation fates of stem cells are influenced by extracellular matrix rigidity (55,246,247). In addition, cell stiffness can be used as a biomarker for cancer metastasis (132,248,249). However, one type of physical force that has largely escaped the interest in mechanobiology is near-zero gravity or microgravity. With growing investments in long-term space exploration and space travel, it becomes important to uncover the physiological adaptations of terrestrial life. However, there is no genetic memory that can be extracted from

changes in physiological responses to variable gravity, since gravity is unchanging on earth (250,251). Thus, it is immensely helpful to understand how microgravity affects cell signaling, gene expression, cell mechanics, and overall cellular physiology and function. To investigate the effects of simulated microgravity on cellular function on the ground, a random positioning machine (RPM) is developed in this work.

Numerous methodologies have been developed and applied to investigate mechanotransduction responses to certain physical cues, harnessing such factors as increased membrane tension, compression, shear, and surface roughness and rigidity (252). These approaches include modulation of membrane tension using atomic force microscopy indentations (253) and uniaxial cell stretching devices (242), control of differentiation and proliferation using hydrogels and micropatterned substrates (55), and mechanophenotyping (254) and sorting based on cancer metastasis biomarkers using various microfluidic devices (19,25–27). Since the first manned space flight in 1961, we have learned, to a certain extent, how microgravity affects terrestrial life, and recent studies have shown that the effect of microgravity is very multifaceted. A multidimensional analysis by NASA on twin astronauts indicated numerous physiological responses such as muscle atrophy, osteoporosis, and genetic and epigenetic responses such as DNA methylation and telomere elongation (258). Because of rare flight opportunities and their associated high cost, performing experiments at the International Space Station is often not feasible nor practical. Therefore, it is important to create experimental conditions to simulate microgravity on earth (259–262), in order to enable experimental studies to understand the mechanism by which simulated microgravity causes alterations at the molecular and cellular level.

Among different methods of simulating microgravity on earth, there exist the use of diamagnetic levitation (263–265), rotating wall vessels (266–268), 2-dimensional clinostats (269–271), 3-dimensional (3-D) clinostats (272–274) and random positioning machines (RPMs). Diamagnetic levitation leverages the diamagnetic material property of biological tissues by placing them in a very large magnetic field to counterbalance the effect of gravity (264). Rotating wall vessels and 2-D clinostats work by subjecting a cell suspension in a container to fast rotations about an axis perpendicular to the axis of gravity until there is no fluid motion relative to the container (275). In 2-D clinostats, specimens are rotated inside a small cylinder and consequently sedimented circumferentially, whereas rotating wall vessels have a larger diameter and are operated at a lower speed such that specimens are not centrifugated away from the center of the vessel (60). The constant reorientation of a sample relative to the gravity vector eventually results in a functional weightlessness of the cells, thus simulating microgravity. 3-D clinostats, on the other hand, utilize a gimbal with two independent axes, each controlled by a dedicated motor, to constantly reorient a sample in the gravity field. When the angular velocity of each gimbal axis is varied randomly or systematically without changing direction, such a device is called a 3-D clinostat; whereas when the sign and/or magnitude are varied systematically or randomly, the device is called a RPM. Other methods of generating microgravity conditions include parabolic flights and free fall of samples from a drop tower; however, these approaches only allow seconds to a few minutes of microgravity conditions (250). While feasible for microgravity simulation, each of these techniques has their own unique and substantial drawbacks. Diamagnetic levitation requires superconducting magnets with an extremely high magnetic field (~17 Tesla) to induce forces in a diamagnetic material or tissue sample, which is highly power-demanding and expensive (265). Further, magnetic fields of such

magnitude can disrupt cellular processes (276). Moreover, the high-speed rotations from 2-D and 3-D clinostats and even from RPMs can have undesired shearing side-effects, especially on adherent cells (277).

In this work, we describe a custom RPM designed to simulate microgravity by reorienting samples while limiting the angular velocity of each gimbal axis to an upper threshold of 42 deg/s. We investigate the effects of simulated microgravity on human osteoblasts hFOB 1.19. Our RPM simulates microgravity by rotating samples about the two orthogonal axes of a two-axis gimbal in a systematic manner to follow a pre-planned trajectory specially constructed to produce a uniform distribution of 3-D orientations. The completely uniform distribution of 3-D gravity vector orientations visited under our RPM control algorithm improves upon previous algorithms (54) that introduce a uniform distribution of angular velocities in the two gimbal axis trajectories, which generates a non-uniform distribution of 3-D orientations. The device is designed for laboratory use and accommodates various cell culture container sizes and can be placed inside a cell culture incubator. Both adherent and suspension cell samples can be subjected to simulated microgravity to ~0.0000123 *g* after 6 hours in RPM. Using this device, we have characterized the effect of simulated microgravity on cytoskeletal arrangement, changes in cell area, circularity, overall cell viability, and changes in human osteoblast stiffness.

3.3 Device design and specifications

A. Device design

The RPM design was based on general design concepts involving a 2-axis gimbal that have been previously described by Kim et al. (278). The hardware scheme of the rotating RPM is depicted in Figure 3-1(a,b). Briefly, the device is composed of three assemblies: a gimbal

comprising two rotating frames, a clamp on the inner gimbal frame to secure tissue culture plasticware, and a support structure. The specified rotation of the two gimbal frames about orthogonal axes mimics the continuity of spherical motion required to average out the gravity vector over time. The smaller inner frame rotates about an axis fixed in the outer frame while the outer frame rotates about another axis fixed in the support structure, and these two axes are always perpendicular to one another. To accommodate cell culture flasks and well plates of various sizes, we designed the inner frame with X-shaped clamping plates attached by shoulder bolts on either side of a central panel. The clamping structure contains ample room so that it may be used in conjunction with custom-made holders to address specific experimental needs. It can carry up to the equivalent of 4 T75 flasks.

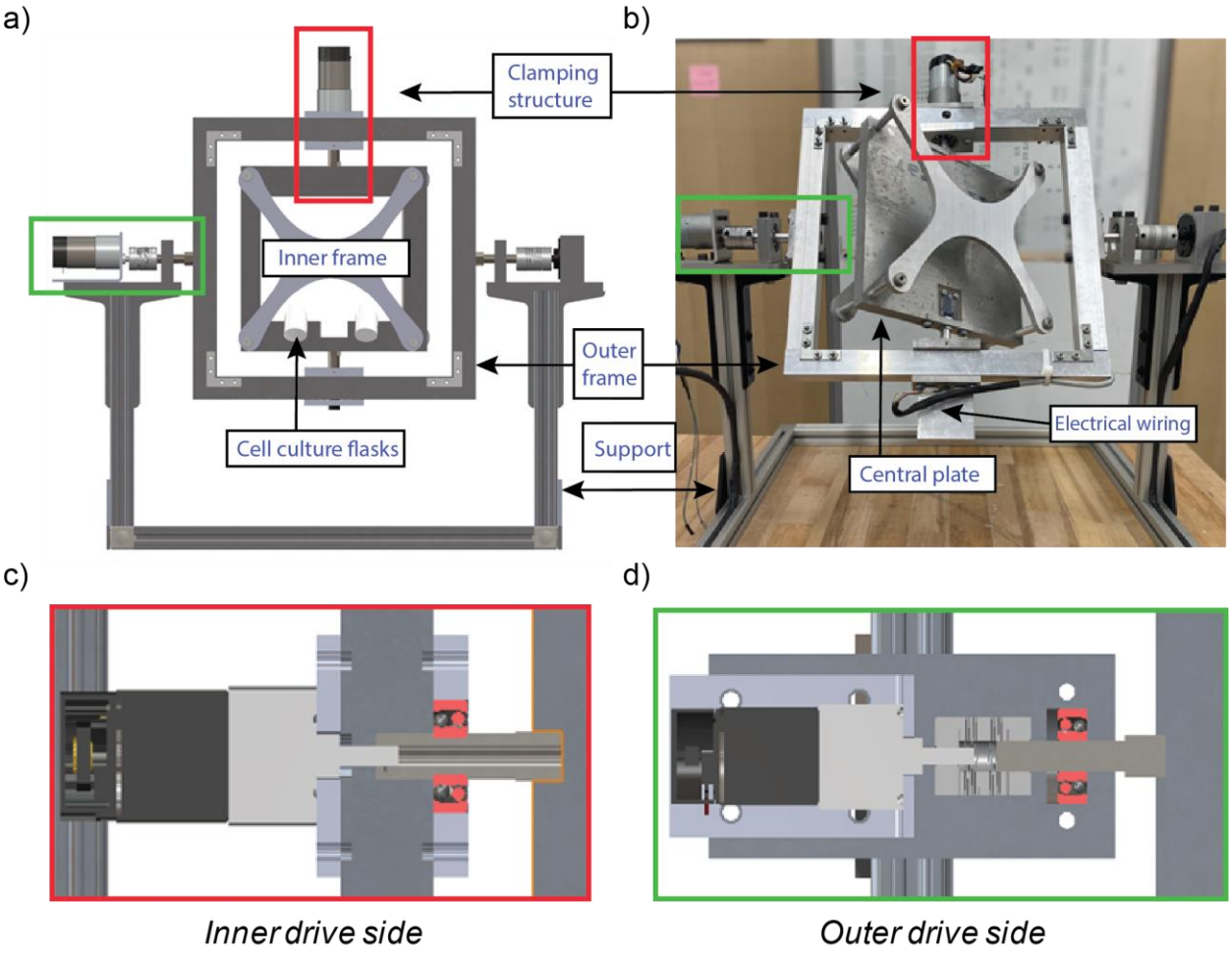

Figure 3-1 Hardware design of the RPM a CAD model of the RPM depicting the secured payload to the central frame. **b** Photo of RPM showing connected wiring and the center panel. **c** CAD drawing of the cross section of the motor driving rotation of the inner frame. **d** Cross section of the motor driving rotation of the outer frame.

Additionally, the external dimensions and hollow aluminum body of the device (457 x 609 x 482) make it suitable to fit within a standard tissue culture incubator (interior dimension of 508 x 541 x 680 mm) while operating under standard humidity and temperature conditions. Note that the RPM is designed to fit diagonally in the incubator. The rotation of the frames is powered by two 12V DC motors (Pololu Robotics and Electronics) and a Compact L298 Motor Driver is installed to convert the signals from a Raspberry Pi microprocessor into motor commands.

B. Kinematics and Control Algorithm

While three angles are required to orient a rigid body, only two are required to orient a vector. Thus, a two-axis gimbal is sufficient to build a RPM. There exists a surjective map from the two gimbal angles to all orientations of the gravity vector in the inner gimbal frame. However, a uniform distribution of gimbal angles will produce a non-uniform distribution of gravity vector orientations. This follows from the properties of the particular two-variable parameterization of the sphere that corresponds to the kinematics of any two-axis gimbal. For example, if angle q_2 specifies a positive rotation about the horizontal axis $\boldsymbol{a_1}$ fixed in the earth frame and angle q_2 defines a positive rotation about the axis $\boldsymbol{b_2}$ fixed in the outer gimbal frame (see Figure 3-2(a)), then the angles q_1 and q_2 correspond to azimuth and elevation angles

specifying a vector of length r on the surface of a sphere. The area of a differential element in the q_1-q_2 plane maps to an area

$dA=dq_1\,dq_2 = r^2 \cos q_2\, dq_1\, dq_2$ of the differential element of the sphere surface. As $q_2 = \pi/2$ or $q_2 = -\pi/2$, the differential element of area on the sphere becomes infinitesimally small. Thus, whether the two gimbal axes are driven at constant or random speeds or speeds that reverse direction at random times, there will result a non-uniform distribution of the gravity vector orientation in the inner gimbal frame. A certain non-uniform distribution on the q_1-q_2 plane would be required to produce a uniform distribution on the sphere, and such a distribution can be constructed using, for example, Archimedes' Theorem (279). Rather than determining the non-uniform distribution on the q_1-q_2 plane, we first constructed a reference trajectory on the sphere that visits all points with equal likelihood and subsequently used a trajectory tracking controller to cause the two-axis gimbal to follow this reference. Importantly, the algorithm used to generate the reference trajectory on the sphere is divorced from the gimbal kinematics.

To produce a uniformly random distribution of points on the surface of a sphere, we first drew a large number of random samples from a Gaussian function in three variables with zero mean. We then projected each point onto the surface of a unit sphere by dividing the position vector to each point by its distance from the origin. Neighboring points on the sphere were subsequently stitched together to form a trajectory with certain properties by adapting an algorithm from the field of computational geometry (280,281). The trajectory properties of concern are the geodesic curvature (how fast the curve is turning in the plane tangent to the surface at each point) and the distance between trajectory samples (the arclength derivative or speed along the trajectory). The geodesic curvature and speed determine the eventual angular velocity and angular acceleration to which the sample will be exposed in the moving RPM.

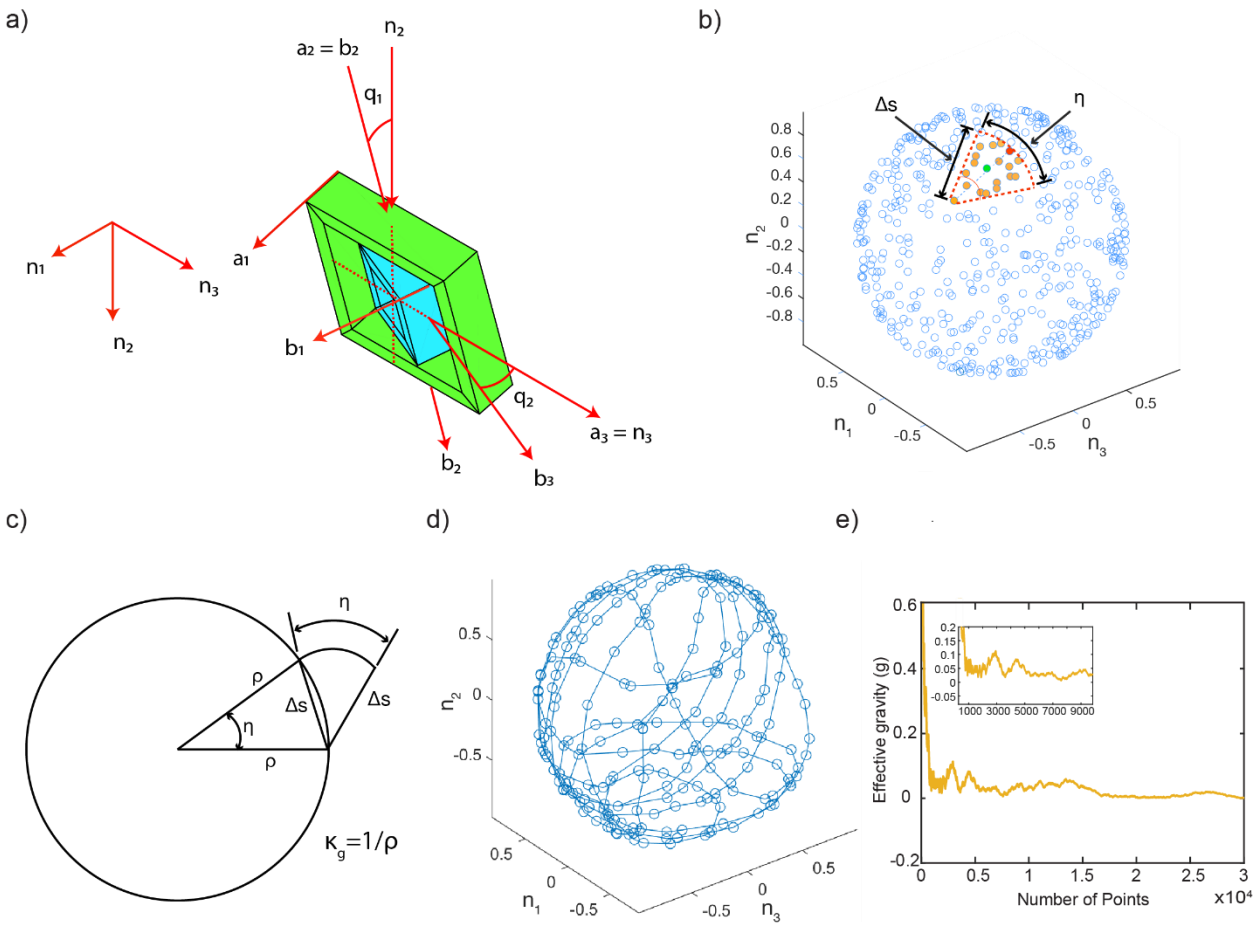

Figure 3-2 RPM model and simulation a A MATLAB-generated figure showing the configuration of the RPM and definitions for the angles q_1 and q_2 when displaced. **b** Points in a uniform random distribution on a unit sphere. Among candidate points (orange) lying within a wedge of angle η and radius Δs, one point is selected (green) and its distance from the previous point normalized before being added to the trajectory (red). **c** Trigonometric construction for determining the maximum geodesic curvature from the wedge parameters η and Δs. **d** A sample of the trajectory path created by the algorithm. **e** decreasing effective gravity experienced by the system as a function of the number of points generated by the program. 10,000 points corresponds roughly to one hour of run time. Inset shows the first 10,000 points.

To develop a trajectory that limits the maximum angular velocity and angular acceleration, we developed a random walk algorithm. After selecting at random an initial point and initial direction tangent to the sphere at the initial point, a family of points within a wedge anchored at the present point and centered about the present direction were considered candidates for the next point (see Figure 3-2(b)). The inscribed angle η and a radius Δs that parametrize the wedge were set to limit the angular velocity and angular acceleration of the sample as further described below. To increment the trajectory, a point within the wedge was selected at random and stitched to the present point. The distance between consecutive points on the trajectory was set to a constant value by dividing the position vector to the next point by its distance from the last and multiplying by the parameter Δs. With the distance between trajectory points set at Δs and the angle at which the trajectory turns in the tangent plane limited by the angle η, the maximum geodesic curvature of the trajectory on the sphere is determined. The relationship between the maximum geodesic curvature κ_g and the wedge inscribed angle η and radius Δs is apparent from the diagram in Figure 3-2(c) and is available in

$$\kappa_g = \frac{1}{\rho} = \frac{2sinsin\left(\frac{\eta}{2}\right)}{\Delta s} \qquad (1)$$

The sequence of points thus generated can be considered a reference trajectory in the task-space of the two-axis gimbal. It remains to convert this trajectory in three Cartesian coordinates into a trajectory for each of the two gimbal axis angles. Let the unit vector $\mathbf{n_2}$ point vertically downward (in the direction of the local gravity vector) and let $\mathbf{n_1}$ and $\mathbf{n_3}$ span the horizontal plane. A position vector locating a point on the unit sphere can be written $\mathbf{x} = k_1\,\mathbf{n_1} + k_2\,\mathbf{n_2} + k_3\,\mathbf{n_3}$. Likewise, the i^{th} point in our random walk trajectory can be represented in the column matrix $\mathbf{x_i} =$

$[k_{1i}\ k_{2i}\ k_{3i}]^{\mathrm{T}}$, where T designates the matrix transpose. Since the points all lie on the surface of a unit sphere, we have

$$k_{1i}^2 + k_{2i}^2 + k_{3i}^2 = 1 \qquad (2)$$

Also, between consecutive samples on the trajectory, we can measure the pathlength using $\Delta s = [(k_{1i} - k_{1i-1})^2 + (k_{2i} - k_{2i-1})^2 + (k_{3i} - k_{3i-1})^2]^{1/2}$

In the following, we develop a simple algorithm using the two gimbal axis angles (joint angles), which we will call q_1 and q_2. While we have chosen the three variables k_1, k_2, k_3 to describe the points in the uniformly sampled distribution on the sphere, these three variables carry the constraint Eq. (2). This constraint can be handled implicitly by choosing only two generalized coordinates q_1 and q_2 (the method we expound upon here) or by embedding the constraint derivative in a description of the differential kinematics containing three variables.

Let $\mathbf{a_1}$, $\mathbf{a_2}$, $\mathbf{a_3}$ comprise a right-handed orthonormal set of basis vectors fixed in the outer gimbal frame *A*, with $\mathbf{a_i}$ initially aligned along $\mathbf{n_i}$, (i = 1,2,3) as shown in Figure 3-2(a). Likewise, fix a basis comprising $\mathbf{b_i}$ in the inner gimbal frame *B*, with $\mathbf{b_i}$ initially aligned along $\mathbf{n_i}$ (i = 1,2,3). A simple rotation of *A* in *N* through the angle q_1 about $\mathbf{n_3} = \mathbf{a_3}$ produces the displaced configuration of the outer gimbal frame. And a simple rotation of *B* in *A* through the angle q_2 about $\mathbf{n_3} = \mathbf{a_3}$ produces the displaced configuration of the inner gimbal frame, as shown in Figure 3-2(a). Rotation matrices ${}^{N}R^{A}$ and ${}^{A}R^{B}$ can be constructed to describe the orientation of *A* in *N* and *B* in *A*, respectively, as:

$${}^{N}R^{A} = \begin{bmatrix} c_1 & -s_1 & 0 \\ s_1 & c_1 & 0 \\ 0 & 0 & 1 \end{bmatrix} \qquad (3)$$

$$ {}^{A}R^{B} = \begin{bmatrix} c_2 & 0 & s_2 \\ 0 & 1 & 0 \\ -s_2 & 0 & c_2 \end{bmatrix} \tag{4} $$

where c_i indicates $cos(q_i)$ and s_i indicates $sin(q_i)$, (i = 1,2). The rotation matrix ${}^{N}R^{B}$ orienting frame *B* in *N* is available as the product ${}^{N}R^{B} = {}^{N}R^{A}\ {}^{A}R^{B}$.

The vector $\mathbf{b_1}$ that points outward from the face upon which the sample is to be mounted shall be considered the reference vector. That is, at the beginning of a run, $\mathbf{b_1}$ shall be aligned with the gravity vector, yielding $q_1(0) = \pi/2$ and $q_2(0) = 0$. The forward kinematics can be derived by expressing the vector $\mathbf{b_1}$ in the *N*-frame

$$ b_1 = c_1 c_2 n_1 + s_1 c_2 n_2 - s_2 n_3 \tag{5} $$

and equating terms with the expression for $\mathbf{x} = k_1\,\mathbf{n_1} + k_2\,\mathbf{n_2} + k_3\,\mathbf{n_3}$. The forward kinematics can be inverted in various ways, but one of the more robust ways makes use of the four-quadrant inverse tangent $atan2(x, y)$ as follows

$$ q_1 = atan2\left(\frac{k_2}{\sqrt{k_1^2+k_2^2}}, \frac{k_1}{\sqrt{k_1^2+k_2^2}}\right) \tag{6} $$

$$ q_2 = (-k_3) \tag{7} $$

An even more robust algorithm can be constructed by inverting the forward differential kinematics

$$ \dot{k_1} = -c_1 s_2\ \dot{q}_2 - s_1 c_2\ \dot{q}_1 \tag{8} $$

$$ \dot{k_2} = -s_1 s_2\ \dot{q}_2 - c_1 c_2\ \dot{q}_1 \tag{9} $$

$$\dot{k_3} = -c_2\dot{q}_2 \tag{10}$$

which produces

$$\dot{q}_2 = \frac{k_1\dot{k}_2 - k_2\dot{k}_1}{k_1^2 + k_2^2} \tag{11}$$

$$\dot{q}_2 = -\frac{\dot{k}_3}{\sqrt{k_1^2 + k_2^2}} \tag{12}$$

Although the trajectory generated by our algorithm above is sampled, it may be considered a smooth differentiable curve embedded in the surface of a sphere for the purpose of estimating the acceleration experienced by a sample particle lying a given distance from the center of rotation. As such, the trajectory gives rise to a moving trihedron or basis of three orthonormal unit vectors known as the Darboux frame. The kinematics of the Darboux frame are directly related to the parameters of our algorithm and are well suited for generating an expression for the acceleration of a particle at the edge of the sample.

Consider the spherical curve generated by a particle *P* lying a distance *r* from the center of rotation *O*. The position vector $r\boldsymbol{b_1}$ locating *P* relative to *O* can be differentiated with respect to pathlength *s* to obtain a unit tangent vector which we shall call $\boldsymbol{d_1}$. The surface itself defines the unit normal $\boldsymbol{d_3}$, which in the case of the sphere is simply $\boldsymbol{b_1}$. The trihedron is complete with $\boldsymbol{d_2} = \boldsymbol{d_3} \times \boldsymbol{d_1}$, and $\boldsymbol{d_1}$ and $\boldsymbol{d_2}$ span the plane tangent to the sphere at *P*. Equations relating the derivatives of the vectors $\boldsymbol{d_i}$ (i = 1,2,3) with respect to pathlength are available in a set of equations containing a skew-symmetric matrix associated with the Darboux frame,

$$\frac{d}{ds}\begin{bmatrix}\boldsymbol{d_1}\\ \boldsymbol{d_2}\\ \boldsymbol{d_3}\end{bmatrix} = \begin{bmatrix}0 & 0 & \kappa_n\\ -\kappa_g & 0 & \tau_r\\ -\kappa_n & -\tau_r & 0\end{bmatrix}\begin{bmatrix}\boldsymbol{d_1}\\ \boldsymbol{d_2}\\ \boldsymbol{d_3}\end{bmatrix} \tag{13}$$

where κ_g is the geodesic curvature, κ_n is the normal curvature, and τ_r is the relative torsion. These equations (13) are analogous to the Serret-Frenet formulas for a space curve.

In the case of a sphere of radius *r*, $\kappa_n = -1/r$, and κ_g is the deviation of the curve from a great circle (the geodesic, or curve of shortest distance between points on the sphere).

The angular velocity ${}^N\boldsymbol{\omega}^D$ of the Darboux frame *D* in *N* can be expressed ${}^N\boldsymbol{\omega}^D = \boldsymbol{d_1}\dot{\boldsymbol{d}}_{\boldsymbol{2}} \cdot \boldsymbol{d_3} + \boldsymbol{d_2}\dot{\boldsymbol{d}}_{\boldsymbol{3}} \cdot \boldsymbol{d_1} + \boldsymbol{d_3}\dot{\boldsymbol{d}}_{\boldsymbol{1}} \cdot \boldsymbol{d_2}$, where $(\dot{})$ indicates differentiation with respect to time. A straightforward application of the formulas for the pathlength derivatives of the basis vectors yields

$$ {}^N\boldsymbol{\omega}^D = \left(\tau_r \boldsymbol{d_1} - \kappa_n \boldsymbol{d_2} + \kappa_g \boldsymbol{d_3}\right)\dot{s} \qquad (14)$$

The acceleration ${}^N\boldsymbol{a}^P$ of particle *P* in *N* may be computed by differentiating the velocity ${}^N\boldsymbol{v}^D$ of *P* in *N*, which is available in ${}^N\boldsymbol{v}^D = \dot{s}\boldsymbol{d_1}$. By design, our algorithm sets $\ddot{s} = 0$, and $\boldsymbol{d_1}$ is fixed in *D*. Thus ${}^N\boldsymbol{a}^P = {}^N\boldsymbol{\omega}^D \times \dot{s}\boldsymbol{d_1}$, which yields

$$ {}^N\boldsymbol{a}^P = \kappa_g \dot{s}^2 \boldsymbol{d_2} + \kappa_n \dot{s}^2 \boldsymbol{d_3} \qquad (15)$$

This acceleration expression has two components, the centrifugal acceleration $a_c = \kappa_n \dot{s}^2$ in the $\boldsymbol{d_3}$ direction and a tangential acceleration $a_t = \kappa_g \dot{s}^2$ in the $\boldsymbol{d_2}$ direction. Note that for the sphere, the normal curvature κ_n has a constant value of $-1/r$, where *r* is the radius of the sphere traced by the point *P*.

We used the algorithm described above to produce a trajectory with 603,000 points that would run over 10 hours, yielding a time interval Δt per trajectory increment of 0.0597 s. The two parameters that define the wedge, the inscribed angle η, and radius Δs were set as follows: $\eta = 30°$ and $\Delta s = 0.05$ m on the unit sphere or $\Delta s = 0.05r$ m on a sphere of radius *r*. Thus, the

trajectory speed $\dot{s}$ can be estimated as $\dot{s} = \frac{\Delta s}{\Delta t} = 0.8375r$ m/s. These values produce a centrifugal acceleration $a_c = \left(\frac{\Delta s}{\Delta t}\right)^2 \frac{1}{r} = 0.7014r$, which for a particle located a distance *r* of 10 cm from the center of rotation produces a_n = 0.0072 g's. Note the centrifugal acceleration produced by our algorithm is constant. The maximum tangential acceleration occurs when a point at the edge of the wedge is selected at random, producing a geodesic curvature $\kappa_g = \frac{2sinsin\left(\frac{\eta}{2}\right)}{\Delta s} = \frac{10.35}{r}$. Thus, the maximum tangential acceleration is $a_t = \left(\frac{\Delta s}{\Delta t}\right)^2 \frac{10.35}{r} = 7.26r$, which for a particle located a distance *r* = 10 cm from the center of rotation produces a_t = 0.074 *g*'s. Figure 3-2(e) shows the cumulative average of the gravity vector, or the effective gravity as a function of the number of points traversed within the trajectory. By the end of the trajectory (6 hours) the measured effective gravity is 0.0000123 *g*'s.

3.4 Materials and methods

A. Cell culture

Human osteoblasts hFOB 1.19 (ATCC) were cultured in growth medium 1:1 DMEM/F-12 supplemented with 2.5 mM L-glutamine, 0.3 mg/ml G418, and 10% FBS. Cells were cultured both adhered and in suspension, using a slide flask with a 10 cm^2 culture area (Nunc Lab-Tek flask on slide) (Thermo Fisher Scientific) and using 15 ml falcon tubes, respectively. Cells were cultured inside a cell culture incubator at 33.5 ^oC with a constant supply of 5% CO_2. Identical conditions were applied for cells subjected to simulated microgravity using our RPM.

B. RPM, orbital shaker and rocker setup

Our RPM was located inside a cell culture incubator. Once the cells were seeded inside the slide flask, adhered on the glass surface, and once they reached ~40% confluency, samples were loaded into the RPM sample holder to begin simulated microgravity treatment. The slide flask was completely filled with medium just before running the RPM to avoid unwanted, high shear inducing fluid flow due to random rotation inside the RPM. Control experiments to decouple the effect of shear from the simulated microgravity were performed using sample shakers. A 3-D rotator (Thermo scientific) was used to agitate adherent hFOB cells. Whereas, the MaxQ 4450 orbital shaker (Thermo Scientific) was used to subject suspension hFOB cells to a high shear environment at 220 rpm.

C. Viability assay

Cells cultured in suspension (~$2.3x10^4$ cells/ml) were mounted on the RPM in falcon tubes. After 3 and 6 hours, cells were collected, washed, and resuspended in PBS. Propidium iodide (PI) was added at a concentration of 500 ng/ml and incubated in the dark for 10 minutes. A total of 10,000 cells were analyzed prior to gating with the Guava EasyCyte Flow Cytometer and FlowJo software. The experiment was repeated three times and statistics were performed using a one-way ANOVA test.

D. Fixation and immunolabeling

Adhered hFOB cells were fixed immediately after retrieving cells from RPM in a 1 *g* condition using 4% paraformaldehyde (Thermo Fisher Scientific) diluted in PBS for 15 minutes followed by washing 3 times using 1X PBS. The fixed cell membrane was permeabilized using 0.1% Triton X-100 (Sigma-Aldrich) in PBS for 15 minutes followed by washing with 1X PBS. Cells were then blocked in 3% BSA for 1 hour followed by overnight incubation with mouse

anti-beta-tubulin (1:1000) (Sigma-Aldrich) in 4^{o}C. Cells were then incubated in rabbit anti-mouse Alexa Fluor 568 (1:1000), Acti-stain 488 phalloidin (1:1000) (Cytoskeleton Inc), and fluorescent DNA stain DAPI (1 µg/ml) for 1 hour. Following 3 additional washes with PBS, the cells were mounted for fluorescence imaging.

E. Imaging and image analysis

Fluorescence images of immunolabelled adhered fixed cell samples were taken using a spinning disk confocal microscope (Olympus IX73 with Yokogawa CSU-X1) using a 40X oil immersion objective. Acti-Stain 488 phalloidin, rabbit anti-mouse Alexa Fluor 568 and DAPI were excited at 488, 561, and 405 nm, respectively, with exposure time of 200, 50, and 100 ms, respectively. Images of cells were visualized, and cell area and circularity of cells were then measured using ImageJ.

Cells in suspension, approximately 10^6 cells/ml, used in stiffness characterization were fluorescently labeled by incubating cells with 5 µM lipophilic dye (Vybrant DiI cell-labeling solution) (Thermo Fisher Scientific) for 20 minutes followed by washing with fresh media. Fluorescence images of cells inside the microfluidic micropipette aspiration device were taken using a Nikon Ti-eclipse epi-florescence microscope with a laser excitation of 561 nm using a 40X objective. Collected images were processed and protrusions inside micropipette aspiration channels were measured using ImageJ.

F. Microfluidic micropipette aspiration experiments

For stiffness characterization of hFOB cells cultured in suspension in 1 *g* condition and after experiencing simulated microgravity for 3 hours and 6 hours, we used a custom multilayer

PDMS-based microfluidic pipette array (μFPA) device (203) according to principles akin to a glass capillary-based micropipette aspiration set up. Cells cultured in suspension under different conditions were fluorescently labeled and introduced into the device using the iFlow Touch Microfluidic Pump System pressure/flow controller (PreciGenome, San Jose CA, USA). The pressure controller used in this work allows for direct control of valves and pumps via a 10 inch user friendly touch screen interface with 8 outlet ports available to provide pulse-free positive and negative pressures at a resolution of 1 μl/min. The μFPA device connected to the cell solution containing an Eppendorf tube and pressure controller in series was mounted on to a Nikon Ti-eclipse epi-florescence microscope for imaging using a 40X objective. The field of view allowed simultaneous observation of 8 aspiration chambers. First, cells at a density of 10^6 cells/ml were loaded into the micropipette aspiration chamber by applying a pressure of 0.2 psi. Then, cells were aspirated by increasing the pressure in increments of 0.1 psi until the cell protrusion length (L_p) became equal to the pipette hydraulic radius (R_p), forming a hemispherical protrusion at approximately 1 psi. The upper limit for cell protrusion length allowed us to measure cortical tension of the cells assuming a cell behaves like a homogeneous elastic solid. DiI was excited at 561 nm and fluorescence images were taken after 2 minutes of wait time between every pressure interval. The cell stiffness was then estimated according to (282):

$$E = \frac{\frac{3\Delta p \Phi}{2\pi}}{\frac{L_p}{R_p}} \tag{16}$$

where E is Young's modulus, Δp is the pressure difference at the aspiration chamber, and Φ is a geometric constant that takes a value of 2.1. The pressure difference Δp is theoretically determined by the Darcy-Weisbach equation as a function of the flow rate and was further numerically confirmed (203). We measured the flow rate for a range of controller pressure values. The controller pressure was converted to pressure across the microfluidic aspiration

pipette (Δp) from the measured flow rates at the various applied pressures and using the theoretical analysis reported previously for this device (203).

G. Flow cytometry

To determine the amount of polymerized actin of cells in suspension, actin filaments were stained using phalloidin, and fluorescent intensity of individual cells was measured using flow cytometry. Cells cultured in suspension were mounted on the RPM in falcon tubes. After 3 and 6 hours, cells were collected along with the control cells, and fixed and permeabilized by using PFA and Triton X-100 in PBS. Cells were incubated in the dark for 30 minutes with 14 nM acti-stain 488 phalloidin to stain actin filaments. Cells were then washed and resuspended in PBS for analysis. A total of 5,000 cells were analyzed prior to gating with the Guava EasyCyte Flow Cytometer and FlowJo software.

H. Microgravity validation and vibration severity

To validate our RPM can achieve time-averaged simulated microgravity and to measure vibrational severity of RPM and high shear inducing environments such as a rocker and an orbital shaker, we used a wireless accelerometer - vibration meter (Monnit, MNS2-9-W2-AC-VM-SW). We mounted the vibration meter at the center of the RPM where cell samples are placed. Vibration and velocity vectors were measured at a measurement interval of 1 minute for 9 hours. With the velocity vectors from each measurement, acceleration was collected between intervals (change in velocity) and averaged to compute the time-averaged acceleration. As for measuring vibrational severity for rocker and orbital shaker, the vibration meter was mounted at a fixed location and vibration was measured and averaged over 30 minutes.

I. Statistical analysis

One-way ANOVA tests were used to determine the statistical significance of cell area, circularity, and Young's modulus data. Furthermore, *p*-values were determined using two-tailed Student's t-test and assigned * and ** corresponding to $p < 0.05$ and $p < 0.01$, respectively.

3.5 Results

A. Simulated microgravity exposure induced cytoskeletal disruption and cell shape changes

Physical forces that induce genetic and epigenetic changes in cells are transmitted via mechanotransduction through the cytoskeleton by rearranging and restructuring various cytoskeletal networks. In order to study cytoskeletal changes induced by cells experiencing simulated microgravity, we visualized actin and microtubule networks of adhered hFOB cells subjected to 3 and 6 hours of simulated microgravity in our RPM. Simulated microgravity was measured using an accelerometer and calculating time-averaged acceleration over 6 hours inside RPM, which was found to be ~0.0000123 *g*. When loading samples, media were filled to the volume of the flasks in order to reduce the effect of shear stress due to bubbles. Observations under bright field imaging following simulated microgravity treatment revealed changes in cell spreading area and a decrease in the number of adhered cells suggesting RPM exposure induced cell detachment. This observation is consistent with a previous study (283), where increased cell detachment of ROS 17/2.8 cells following simulated microgravity using a 2-D clinostat was shown. Fluorescence images of F-actin showed that there was a significant cytoskeletal disruption compared to our control sample cultured under a 1 *g* condition. As shown in Figure 3-

3(a), hFOB cells had disorganized actin networks and fewer stress fibers after experiencing simulated microgravity for 3 hours and 6 hours. However, there were no noticeable differences between the 3-hour and the 6-hour time points. In addition, we did not observe any distinct differences in microtubule organization and nuclear size between 1 *g* and simulated microgravity conditions. Although our RPM can be run for shorter or longer periods, we did not run the experiment beyond 6 hours as this could lead to further cell detachment. We have also noticed that prolonged (over 1 day) culture of hFOB cells in suspension would lead to cell death (not shown). From the analysis of fluorescence images, we found a significant increase in circularity from ~0.2 to ~0.6 and decrease in spreading area from ~3000 μm^2 to ~1000 μm^2 after cells were exposed to simulated microgravity (Figure 3-3(b,c)). To decouple the effects of shear from fluidic motion inside the RPM, we performed an experiment by placing adherent hFOB cells in a rocking shaker with vibration severity of 74 Hz at 30 rpm with a 10^o tilt, providing a high shear environment. Compared to cells in a static 1g environment, there was no clear difference in cellular morphology as shown in Figure 3-4.

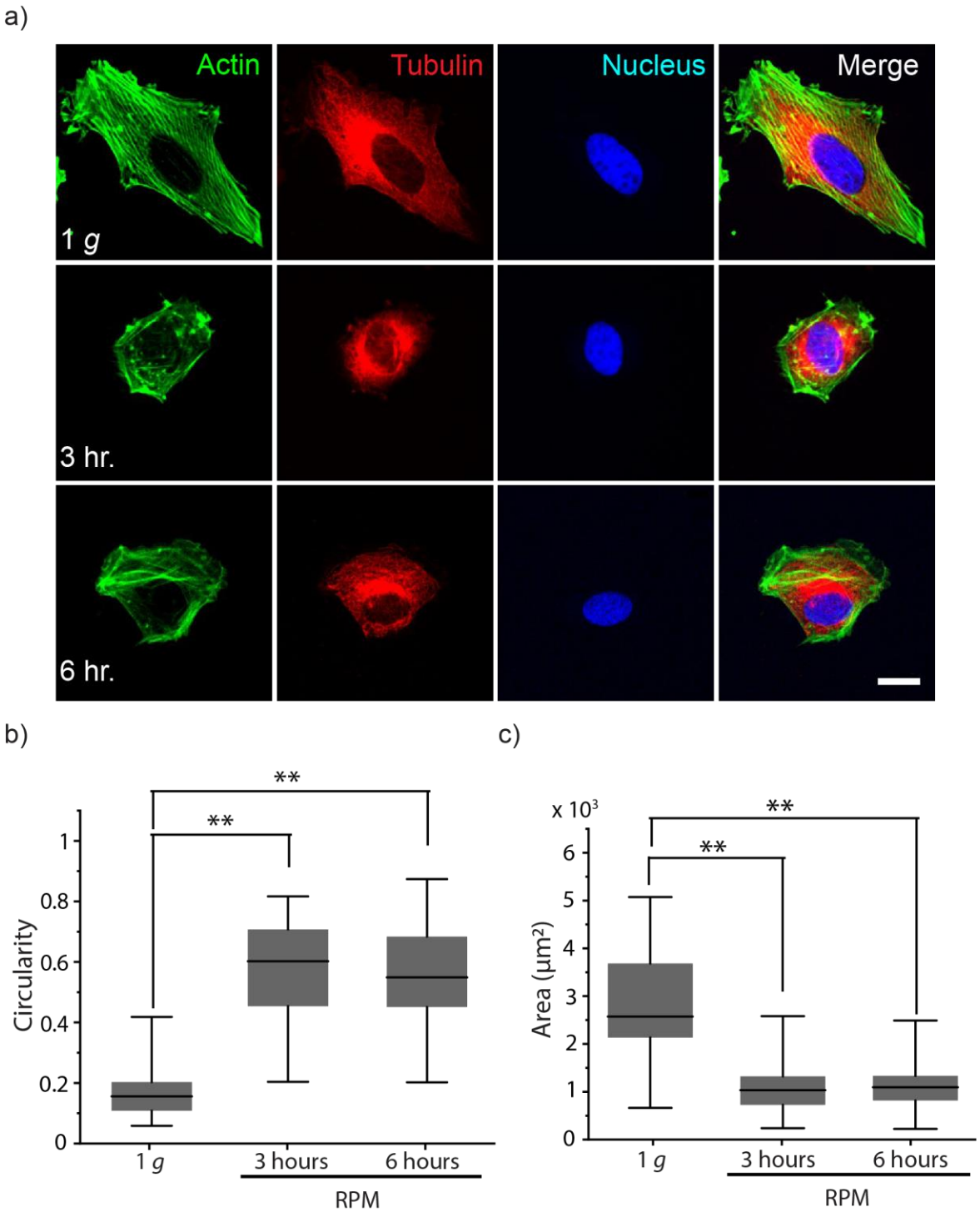

Figure 3-3 Morphology analysis of hFOBs via immunostaining a Representative images of F-actin stained with acti-stain 488 phalloidin, immunofluorescently labeled microtubule and the nucleus of hFOB cells under 1 *g* condition or experiencing simulated microgravity for 3 or 6

hours. Scale bar: 10 µm. **b** Measurement of cell spreading area between the three conditions indicated in **a**. N = 51. **c** Quantification of circularity for conditions in **a** scored within 0 - 1 range, where 1 represents a perfect circle and 0 an increasingly elongated polygon. N = 51.

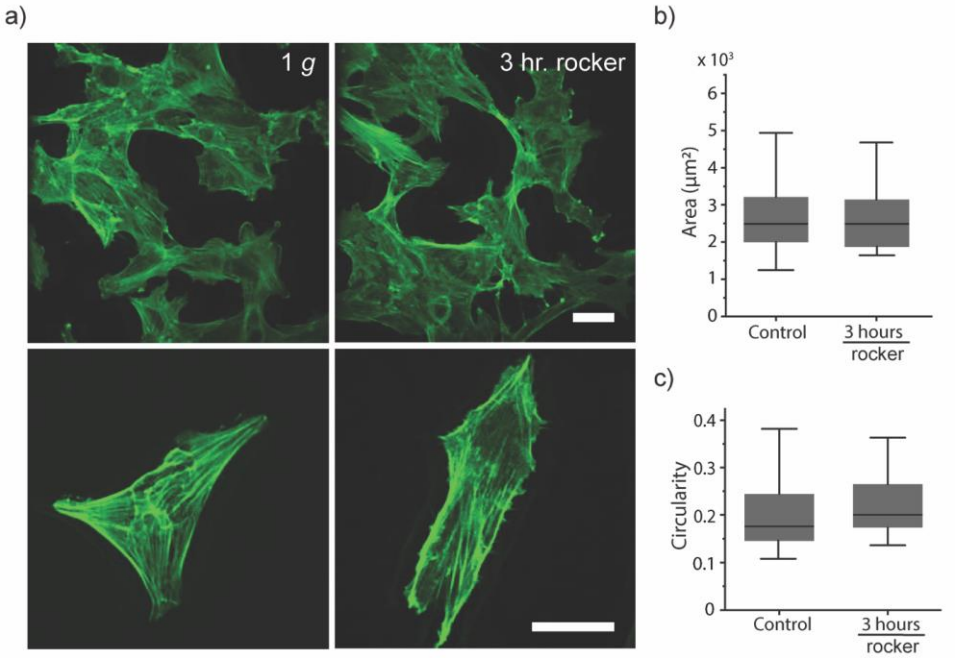

Figure 3-4 hFOB shape response to shear a Fluorescence images of phalloidin-labeled actin filaments in fixed hFOB cells in static (control) and perturbed on a rocking shaker for 3 hours. Scale bar: 10 µm. N = 2. **b** Box plot of area of cells measured between a static and shearing environment. **c** Box plot of circularity of cells measured between a static and shearing environment. $N_{cell} > 22$.

B. Simulated microgravity reduced stiffness of human osteoblasts

Our next set of experiments were performed with hFOB cells in suspension subjected to simulated microgravity. Among the various changes that result from mechanotransduction are changes to the mechanical properties of a cell. As the main structural component, reorganization

and disruption of cytoskeletal components are known to result in variations in the mechanics of a cell. For example, differences in cytoskeletal organization of cancer cells is known to affect cell stiffness (284). Given that data from the above experiment indicate simulated microgravity from RPM exposure results in the disruption of actin filaments, we asked whether simulated microgravity might impact the mechanical properties of hFOB cells. Firstly, we confirmed that the viability test indicated that hFOB cells remained viable under simulated microgravity (Figure 3-5(b)). Consistent with what we found for adherent hFOB cells, filamentous actin was also significantly reduced in suspended hFOB cells subjected to simulated gravity. To quantify cell stiffness, we utilized a PDMS-based microfluidic micropipette aspiration device previously established in our group (203) to measure the stiffness of hFOB cells cultured under a 1 *g* condition and after recovering cells in suspension from being in the RPM for 3 hours and 6 hours. To ascertain that these observations are due to cellular responses to simulated microgravity induced by RPM and not due to shearing effects, we placed cell suspensions inside an orbital shaker with vibration severity of 37 Hz at 220 rpm. We found the amount of filamentous actin to be the same comparing cells between a static 1 *g* and the shaking condition (not shown).

After cells in suspension were exposed to simulated microgravity inside our RPM, we quantified cell stiffness by measuring elastic deformations of cells that are protruded into the micropipette channel of our device as shown in Figure 3-5(a). This device has a meandering main flow channel making up a total of 16 columns in a single device, and adjacent columns are connected with 4 micropipette aspiration chambers near the turnings of the main channel fixed at constant distances. Due to the head loss that develops as a cell solution flows in the main channel, cells are autonomously trapped and aspirated inside the micropipette aspiration chamber

as a result of the pressure difference between adjacent columns. Flow of the cell solution and subsequent pressure application is generated by using a pressure controller connected to the inlet of our device. The pressure difference between the two sides of the micropipette aspiration chamber autonomously trapped single cells following the fluid streamline. Further increasing the flow rate creates a suction force that allowed us to aspirate on a single cell at controlled pressures. Fluorescence images of DiI-labeled hFOB cells for 1 *g* and simulated microgravity-treated conditions showed deformation with increasing pressures (Figure 3-5(c)). Treating a cell as a homogeneous solid (54,58), the stiffness of hFOB cells subjected to simulated microgravity was found to decrease to ~490 Pa at 6 hours of simulated microgravity exposure compared to ~550 Pa in a 1 *g* environment (Figure 3-5(d)).

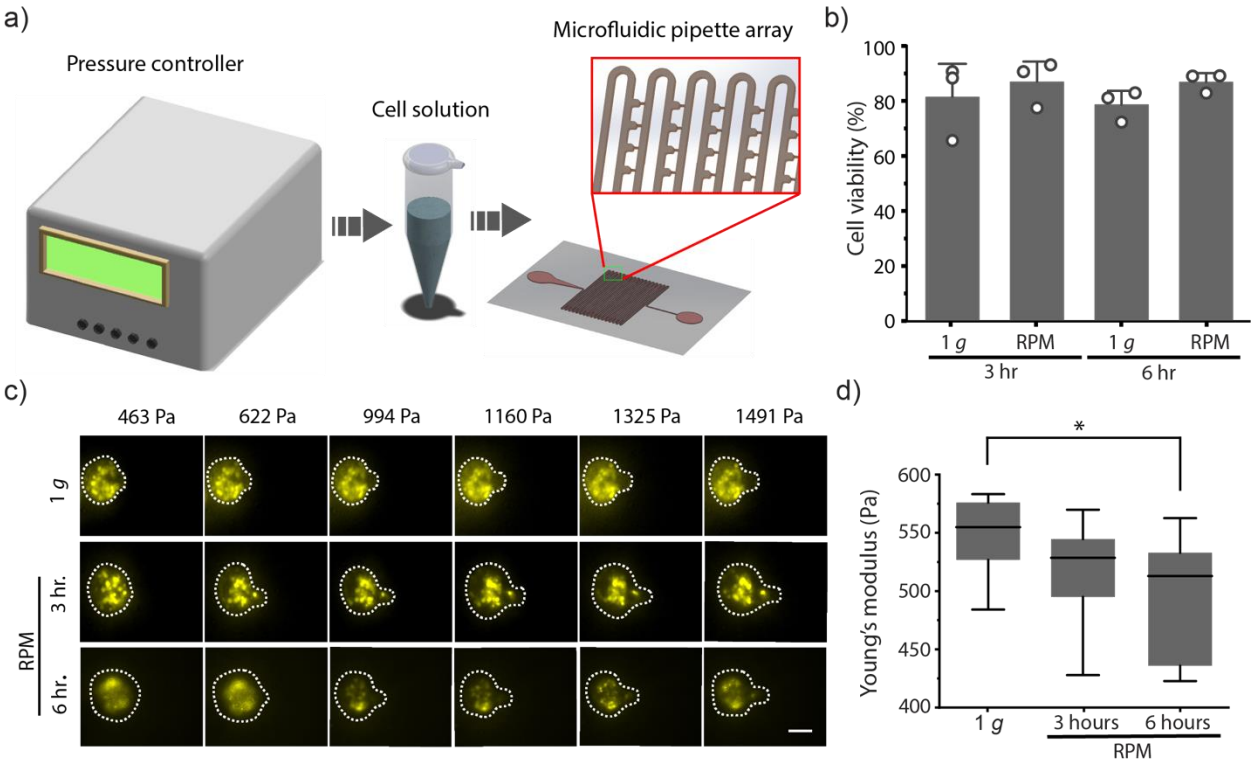

Figure 3-5 Mechanical characterization of hFOB cells in suspension using µFPA device a Schematic of microfluidic device connected to a pressure generator at the inlet of the device. **b** Cell viability test, for cells in suspension, for the indicated conditions as measured by PI staining

using flow cytometry. Three independent replicates were performed for all experiments. Plots indicate mean and standard error of the mean. ** $p < 0.01$. **c** Fluorescence images of aspirated hFOB cells under 1 *g* condition and following 3 hours and 6 hours simulated microgravity treatment. Edges of the cell are contoured using dashed lines. Scale bar: 10 μm. **c** Stiffness measurements for each condition. N = 10. **d** Young's modulus changes of hFOB cells under 1 *g* and simulated microgravity conditions determined using μFPA device. * $p < 0.05$.

3.6 Discussion

In contrast to existing devices used to subject cells to a simulated microgravity environment, including parabolic flights, diamagnetic levitation, and 2-D clinostats, our RPM is a convenient platform for several reasons. For example, compared to altered physical conditions caused by the magnetic fields, our RPM eliminates external effects such as magnetic fields which could have unintended biological consequences. 2-D clinostats have been shown to have lower shearing effects compared multi-axis platforms such as previous RPMs and 3-D clinostats, which create higher shear stresses due to residual acceleration (274) and change in direction of rotation. However, our algorithm is optimized based on prior studies (259), such that the rotational velocity is limited to 42 deg/s and angular acceleration is limited to 0.2 rad/s^2. These limits were chosen to minimize the effects of shearing and vibrational fluid perturbations that might propagate to cells. Our RPM is designed in such a way that is lab-friendly and easy-to-use for research groups to investigate the effects of simulated microgravity on cells here on earth. Among the main biological challenges of long-term space travel for humans is osteoporosis, and thus understanding the effect of microgravity on bone cell development is an important research question. Having a compact, lab-friendly device to simulate microgravity for biological systems

provides an experimental platform that helps address the feasibility of future long-term space travel. This device can be used to further understand the effects of simulated microgravity not only using other cell types, but also to understand the effects of simulated microgravity on tissue formation and genetic mutation. We recognize that the interpretation on the observations of cellular changes we made may be due to simulated microgravity and may not necessarily represent true microgravity conditions where cells are subject to true zero gravity that is not time-averaged and where there is no rotation-induced fluidic turbulence. This can only be confirmed in future experiments studying human osteoblast cells under true microgravity. Furthermore, our study exposing cells to high shear and vibration severity environments presented evidence that the primary factor attributed morphological changes observed after cells were exposed to RPM are not shear forces, rather due to the effects of simulated microgravity.

While our device has significant advantages over existing microgravity simulators, we have verified that our RPM attains simulated microgravity by measuring time-averaged acceleration. Moreover, the gravity experienced by the sample the morphological and physical changes occurring in the cell cultures agree with observations made by others in simulated or real gravity conditions (285–287).

We detected significant changes to actin cytoskeleton assembly in both adherent and suspended hFOBs following simulated microgravity treatment. From the exposure of adherent cells to simulated microgravity, we found a significant change in cell morphology indicated by the decrease in total area and increase in circularity of cells. The observed actin disruption from fluorescence images of adherent cells is consistent with morphological changes. Changes to the actin cytoskeleton following exposure to simulated microgravity were also reinforced by the reduced filamentous actin found in suspended hFOB cells exposed to simulated microgravity.

Differences in cell stiffness, on the other hand, were not very large. This is in contrast to cytoskeleton disruption in breast epithelial cells MCF10A and MDA-MB-231 that led to larger changes to cell stiffness (203,288). We suspect this is due to cell type differences, and that the stiffness of hFOBs may be more dominated by the stiffness of the nucleus. It is well appreciated that the nucleus is 5-10 times stiffer than the surrounding cytoskeleton (289). Depending on the size and stiffness of the nucleus, the mechanical properties of the nucleus can dominate the overall cell stiffness. Although the smaller cell stiffness difference could also be attributed to cell recovery as our measurements were made in 1 *g*, we think the time scale of full cytoskeletal recovery would take longer than the time of our cell stiffness measurements.

In the future, it is also possible to upgrade our device into a more complex platform, for example, by allowing our RPM to achieve intermediate gravities to better understand cellular changes at different levels of gravity. Although human studies have shown that microgravity results in various physiological changes including osteoporosis, these studies do not provide information regarding whether the human body can sustain and adapt to microgravity in the long term. Thus, investigating variable gravity and its long-term effects can be useful to provide information regarding the range of sub 1 *g* gravity that can be habitable for humans and other organisms.

3.7 Conclusion

In this work, we developed a compact RPM device that allowed us to subject biological samples to a simulated microgravity environment in a lab-friendly and compact manner. Our RPM simulates microgravity by rotating samples about two orthogonal axes which are systematically rotated according to a pre-programmed random-walk trajectory on a unit sphere.

A uniform distribution of the gravity vector is achieved by using the inverse kinematics of the RPM to track the pre-programmed trajectory. We were able to achieve a time averaged microgravity of magnitude 0.0000123 *g* after 6 hours. We have also demonstrated the application and utility of our device by examining the effects of simulated microgravity on cytoskeletal organization and shape change in human osteoblast cells. These experiments provided results akin to prior microgravity studies with other cell lines, confirming that the simulated microgravity environment we generated had an effect on human osteoblasts. The development of our RPM device provides a convenient platform to investigate the effects of simulated microgravity here on earth which can be insightful to future long-term space exploration and space travel. This opens up a new domain for mechanotransduction research for investigating a range of cellular processes under simulated microgravity conditions.

3.8 Acknowledgements

This work was supported by the National Science Foundation (NSF-CMMI 1927803 to A.P.L.), NIH's Microfluidics in the Biomedical Sciences Training Program (NIH NIBIB T32 EB005582 to N.W.), National Institutes of Health (NIH-NIGMS 5R25GM086262-10 to E.A.), and the Department of Mechanical Engineering at the University of Michigan, Ann Arbor. We acknowledge the Lurie Nanofabrication Center (LNF) at the University of Michigan for allowing us to use their facilities. We would like to thank Dr. Lap Man Lee and Dr. Jin Woo Lee for their technical support and providing the MATLAB code for pressure difference determination. We would like to thank Benjamin Hamilton for his assistance with calibration of the microfluidic pipette array device.

Chapter 4 Fascin-Induced Actin Protrusions are Suppressed by Dendritic Networks in GUVs

This chapter was published in Molecular Biology of the Cell (MBoC) (2021) fifth special issue on Forces on and within cells. Author contributions: N.H.W. and A.P.L. designed research. N.H.W. and Y.B. performed research. N.H.W. analyzed data. N.H.W., Y.B. and A.P.L. wrote the paper.

4.1 Abstract

The interactions between actin networks and cell membrane are immensely important for eukaryotic cell functions including cell shape changes, motility, polarity establishment, and adhesion. Actin binding proteins are known to compete and cooperate, using finite amount of actin monomers, to form distinct actin networks. How actin bundling protein fascin and actin branching protein Arp2/3 complex compete to remodel membranes is not entirely clear. To investigate fascin- and Arp2/3-mediated actin network remodeling, we applied a reconstitution approach encapsulating bundled and dendritic actin networks inside giant unilamellar vesicles (GUVs). Independently reconstituted, membrane-bound Arp2/3 nucleation forms an actin cortex in GUVs whereas fascin mediates formation of actin bundles that protrude out of GUVs. Co-encapsulating both fascin and Arp2/3 complex leads to polarized dendritic aggregates and significantly reduces membrane protrusions, irrespective of whether the dendritic network is membrane-bound or not. However, reducing Arp2/3 complex while increasing fascin restores membrane protrusion. Such changes in network assembly and the subsequent interplay with

membrane can be attributed to competition between fascin and Arp2/3 complex to utilize a finite pool of actin.

4.2 Introduction

Membrane remodeling due to assembly and disassembly of the actin cytoskeleton is critical to many cellular processes, including cell migration, cell division, and endocytosis (290,291). The ability for actin cytoskeleton to provide structural functionalities in processes like cell movement, adhesion, polarity, and molecular transport depends on the spatial and temporal dynamics of actin networks and the magnitude and direction of forces exerted by these networks (1,292). These dynamic changes in actin networks are achieved by actin binding proteins which enable self-organization of diverse types of actin networks within a confined and shared space while utilizing limited amount of actin monomers (50,293). Inside the cell, multiple actin binding proteins compete and collaborate to construct functional actin architectures (293). For example, filopodia formed by bundled actin filaments and lamellipodia formed by Arp2/3-branched networks can be found at the leading edge of a motile cell (294,295). Similarly, alpha-actinin is prevalent at focal points between cell to cell or cell to substrate contacts facilitating cell adhesion (296,297). Moreover, formin, profilin, cofilin, and capping proteins are responsible for regulating actin polymerization and depolymerization. With the aid of numerous actin binding proteins, actin networks actively and dynamically remodel the cell membrane.

Fascin and Arp2/3 complex are among the well-studied actin binding proteins that are found in protrusive structures at the cell membrane. Fascin is a 55 kDa short actin crosslinker that bundles actin filaments in a tightly packed and parallel manner (294). Fascin-bundled actin networks are responsible for finger-like protrusions in structures like filopodia and microspikes.

These cellular structures mediate cell movement and cell-cell interaction (199,294). Arp2/3 complex on the other hand is a 224 kDa multifunctional actin branching protein made up of 7 subunits (298). Arp2/3 complex, when activated by the VCA domain of the neural Wiscott-Aldrich Syndrome protein (N-WASp) (299,300), branches actin filaments to form a dendritic network that plays a major role in force generation at the leading edge of a cell to mediate cell motility (298,301). To study the roles of these actin binding proteins, *in vitro* reconstitution and studies in cells have defined the roles of fascin in filopodia formation and cell migration (48,199,294,302–304) as well as the role of Arp2/3 complex in the formation of an actin cortex (38,39,59,305,306). As an alternative experimental system, others have biochemically reconstituted actin networks on the outside surface or inside giant unilamellar vesicles (GUVs) to independently study actin networks formed by fascin and Arp2/3 complex and their respective interaction with lipid membranes. For example, when encapsulated inside a GUV, fascin was shown to form actin bundles which induced reversible membrane protrusions or formed contractile rings (75,83,307). When polymerized on the outside, reconstitution of Arp2/3-branched network led to the emergence of short filopodium-like actin protrusions into the GUV lumen in the absence of fascin (52,308).

Considering the strong evidence that fascin and Arp2/3 complex organize different types of actin networks in cells, it was surprising that *in vitro* reconstitution studies of branched networks on GUVs formed filopodium-like protrusions. Thus, it is critical to investigate how these two actin binding proteins might cooperate to organize actin networks and thereby remodel the membrane. Co-encapsulation of multiple actin binding proteins in previous studies have revealed formation of emergent structures as a result of either synergy or competition between different actin binding proteins. It was shown recently that the co-encapsulation of α-actinin

together with fascin impairs the formation of protrusive bundled actin structures (83). Similarly, others have shown that membrane remodeling caused by an Arp2/3-induced actin cortex can be tuned by changing the concentration of capping protein (309). In an attempt to show the transformation of lamellipodia into filopodia, a membrane-free assay reconstituting actin networks formed by fascin and Arp2/3 complex revealed a transition from aster-like actin network, which occurred as a result of Arp2/3-mediated nucleation, to star-like networks due to fascin-mediated bundling (48,302). Finally, a previous reconstitution study has shown that fascin-bundled actin can drive motility in *Listeria* independently of Arp2/3-dependent motility in a system that has both fascin and Arp2/3 complex (310). Although these are significant findings, these prior studies have not considered the interaction of actin networks formed by fascin bundling and Arp2/3 nucleation with membrane. To our knowledge, there have been no studies that investigated the interplay between fascin-bundled and Arp2/3-branched networks in a confined membrane-bound space.

In this work, we study the interaction between actin networks formed by fascin and Arp2/3 complex inside GUVs. We hypothesize that these actin binding proteins compete for actin and would alter the resulting networks and consequently affect membrane remodeling. We compare this composite network system with known benchmark systems generated by encapsulating actin with fascin or Arp2/3 complex alone. We show that Arp2/3-branched network at the membrane forms a uniform cortex while fascin-bundled network induces protrusions in a fascin concentration dependent manner. Our experiments show that co-encapsulation of fascin and Arp2/3 complex results in the inhibition of actin bundle protrusions and shortens the bundle lengths compared to fascin-only condition. Our results suggest that

dendritic network formation can suppress filopodia formation through an actin monomer competition mechanism.

4.3 Method

Preparation of proteins.

We purified actin from rabbit skeletal muscle acetone powder (Pel-Freez Biologicals) as described previously (319) or purchased it from Cytoskeleton Inc, USA. ATTO 488 actin and CapZ were purchased from Hypermol Inc, Germany. α-Actinin from rabbit skeletal muscle and Arp2/3 complex from porcine brain were purchased from Cytoskeleton Inc. We purified human fascin from *E. coli* as glutathione-S-transferase (GST) fusion protein (303). For purification, BL21(DE3) *E. coli* cells were transformed with pGEX-4T-3 (GE Healthcare) containing the coding sequences of fascin. Cells were grown at 37 °C while shaking at 220 rpm until the OD_{600} reached 0.5 - 0.6. Protein expression was induced with 0.1 mM IPTG and cell culture was incubated at 24 °C for 8 h. Cells were harvested by centrifugation at 4,000 x g for 15 min and washed with PBS once. Pellets were stored at -80 °C until the day of purification. Cell pellets were resuspended in lysis buffer (20 mM K-HEPES pH 7.5, 100 mM NaCl, 1 mM EDTA, 1 mM PMSF) and ruptured by sonication. Cell lysates were centrifuged at 75,000 x g for 25 min and supernatants were loaded on a GSTrap FF 1 mL column (GE Healthcare) using an AKTA Start purification system (GE Healthcare) at a flow rate of 1 mL/min. The column was washed with 15 mL washing buffer (20 mM K-HEPES pH 7.5, 100 mM NaCl) and the protein was eluted with 5 mL elution buffer (washing buffer + 10 mM reduced L-glutathione). Purified fascin was dialyzed against 1 L PBS twice for 3 h and once overnight at 4 °C. Protein concentration was calculated by UV absorption using predicted molar extinction coefficients (ExPasy) of 110,700 $M^{-1}cm^{-1}$.

Proteins were concentrated with Centricon filters (Merck-Millipore) when needed and/or diluted to a final concentration of 1 mg/mL in PBS.

We purified hexa-histidine-tagged VCA (His_6-tagged VCA) domain from neural Wiskott-Aldrich syndrome protein following the same steps by transformation of BL21(DE3) RIL *E. coli with plasmids* containing the coding sequences of VCA. Induction was performed using 0.5 mM IPTG and incubation of cells at 37°C for 3 h. Cells were harvested by centrifugation at 5,000 rpm for 10 minutes and resuspended in lysis buffer containing 20 mM HEPES pH 7.5, 200 mM NaCl, 10 mM imidazole, and 1 mg/ml lysozyme. Lysate was then flash frozen with liquid nitrogen. Cells were thawed, followed by addition of 1 mM PMSF, and then lysed by sonication. The lysate was incubated with Ni-NTA resin (600 µL resin for 2 mL of lysates) for 2.5 h, washed several times with 20 mM HEPES pH 7.5 containing 200 mM NaCl, and eluted in elution buffer (20 mM HEPES pH 7.5, 200 mM NaCl, 250 mM imidazole) from a column into aliquots. Fractions containing purified His_6-VCA were dialyzed in 20 mM HEPES pH 7.5, 200 mM NaCl, 1 mM TCEP overnight. The concentration of VCA was determined using Nanodrop (Thermo Scientific).

Production of GUVs.

All lipids were purchased from Avanti Polar Lipids (Alabaster, AL). We modified continuous droplet interface crossing encapsulation (cDICE) technique for robust encapsulation in GUVs of various sizes as previously reported (314). Briefly, a custom 3D-printed chamber is mounted on a benchtop stir plate and rotated at 1,200 rpm. An outer solution of 200 mM glucose (matched to the osmolarity of the inner solution) is pipetted into the chamber. Then, the lipid mixture (70% DOPC, 25% cholesterol, 5% DGS-NTA(Ni)) in a mixture of silicone oil and mineral oil (4:1) is

added. The lipid-oil solution forms an interface at the oil-water interface. 20 μL inner solution containing 7.5% OptiPrep (a solution that increases the density of inner solution encapsulated inside GUVs so that they can settle at the bottom of the imaging chamber (75,83)) in 200 mM glucose was added into 700 μL of the lipid-oil mix and droplets were generated by pipetting up and down. For reconstitution of confined actin networks, the inner solution contained 5.3 μM actin including 10% ATTO 488 actin in polymerization buffer, 7.5% OptiPrep, 0 -2.65 μM fascin, 0-2 μM Arp2/3 complex, and 0.5 μM His_6-VCA as indicated. We also encapsulated 200 nM capping protein (CapZ) to regulate actin filament lengths inside vesicles. GUVs were then generated by dispensing the droplets into the cDICE chamber. A lipid bilayer is formed when a second layer of lipid is acquired as the droplets cross the lipid/oil-outer solution interface. In the case of branched actin networks reconstituted on the outer surface of GUVs, vesicles were made using 200 mM glucose for both inner and outer solution. GUVs were then collected and incubated in 5.3 μM actin including 10% ATTO 488 actin, 1 μM Arp2/3 complex, and 0.5 μM His_6-VCA, and actin polymerization buffer (50 mM KCl, 2 mM $MgCl_2$, 0.2 mM $CaCl_2$, and 4.2 mM ATP in 15 mM Tris, pH 7.5).

Imaging and image processing.

Following cDICE, GUVs were transferred to a 96-well plate for imaging. OptiPrep in the inner solution increases GUV density and accelerates sedimentation of GUVs onto the bottom of well plate. An Olympus IX-81 inverted microscope equipped with a spinning disk confocal (Yokogawa CSU-X1), AOTF-controlled solid-state lasers (Andor Technology), and an iXON3 EMCCD camera (Andor Technology) was used for microscopy and controlled by using MetaMorph software (Molecular Devices). Images were acquired by using an oil immersion 60

x/1.4 NA objective lens. Fluorescence images of actin and lipids were taken with 488 nm and 561 nm laser excitation respectively. Z-stack fluorescence confocal image sequence of lipids and actin were taken with a z-step size of 0.5 μm.

Images were processed using ImageJ/Fiji (75,320,321), SOAX (322,323), and MATLAB routines (318). For 3D characterization of actin bundle structures, we generated skeletonized models from regions of interest in actin images. In order to optimize the images for identification of actin bundles, images were first preprocessed using ImageJ/Fiji. The structures from z-stack images are identified and extracted with SOAX source code (322,323) by active contour methods. SOAX program stores all the coordinates of snakes (skeletonized bundles) and joints in a .txt file. Custom MATLAB routines were written to reconstruct the text as a Chimera marker file, include a colormap of z coordinates, and save file as .cmm format. This process enables UCSF Chimera (324) to read the file and provide a better 3D visualization of actin structures for selecting actin bundles and measuring parameters such as bundle length using MATLAB.

Data analysis.

Actin bundle phenotypes and GUV deformation were characterized from z-stack actin and lipid images by counting the number of GUVs that do not assume a spherical shape and are deformed by actin bundles. The diameter of a GUV was measured by line scan from GUV images. The percentages and probabilities of GUV shape changes were obtained by their count divided by the total number of GUVs with actin bundles (i.e. GUVs encapsulating fluorescent actin monomers with no sign of bundling activity were not counted). We calculated the length of actin bundles using the skeletonized images of actin bundles. Bundle length values are shown as average ± standard error of the mean of the data at each fascin concentration. For probability and

percentage measurements at least 2 independent experiments were conducted for each condition indicated. Error bars for reporting protrusion probability represent counting error. Assuming a binomial distribution, this error is calculated as $\sqrt{prob(1-prob)/N}$, where *prob* is the probability of an observation and *N* is the total number of observations. The reported *p* values are two-tail, unpaired two-sample student *t*-test assuming unequal variances.

4.4 Results and Discussion

We first implemented two approaches to assemble a minimal actin cortex by nucleating actin at the membrane using His_6-tagged VCA of N-WASp to activate Arp2/3 complex. The first approach is similar to previous studies reported by Liu et al (52,311), in which dendritic actin networks are polymerized on the external leaflet of the GUV membrane. In this work, we used an emulsion-transfer method called continuous droplet interface crossing encapsulation (cDICE) that is adopted to a benchtop centrifuge to generate GUVs of a variety of sizes, with a composition of DOPC/cholesterol/DGS-Ni-NTA (70/25/5). To form an actin cortex on the surface of GUVs, we used an outer solution comprising 5.3 μM actin, 1 μM Arp2/3, 0.5 μM His_6-tagged VCA in actin polymerization buffer for cDICE. With this approach, His_6-tagged VCA binds to Ni-NTA lipids due to the metal affinity to the His_6-tag, thereby localizing the activation of Arp2/3 complex at the outer leaflet of the membrane (Figure 4-1A). Similar to previous observations by us and others (52,308), we observed a uniform, Arp2/3-nucleated, actin cortex with thin actin protrusions projecting into the vesicle lumen (Figure 4-1B). In our second approach, we encapsulated the same proteins at the same concentrations inside the GUV instead. In contrast, we observed a uniform actin cortex but without any formation of thin actin protrusions (Figure 4-1B). Addition of capping protein CapZ to regulate actin filament lengths

did not alter the actin cortex in GUVs (not shown). It was not immediately clear as to why nucleating dendritic network assembly on the inner leaflet of the membrane did not generate inside-out protrusions. We suspected that this could be a result of differences in membrane curvature with respect to the direction of protrusion, where the force for actin bundle to push and deform from the outside is lower than the force required to protrude membrane from the inside from a force balance analysis - membrane tension would help with outside-in protrusions but inhibits inside-out protrusions. The energetics of out-tube vs. in-tube have also been described to show that out-tube has higher energetics (312) compared to in-tube. Given these considerations, we hypothesize that lowering membrane tension may allow the formation of inside-out protrusions. To test this, we lowered membrane tension by deflating vesicles using a hyperosmotic solution of 70 mOsm difference and observed membrane protrusions induced by actin cortex from the inside (Figure 4-1C).

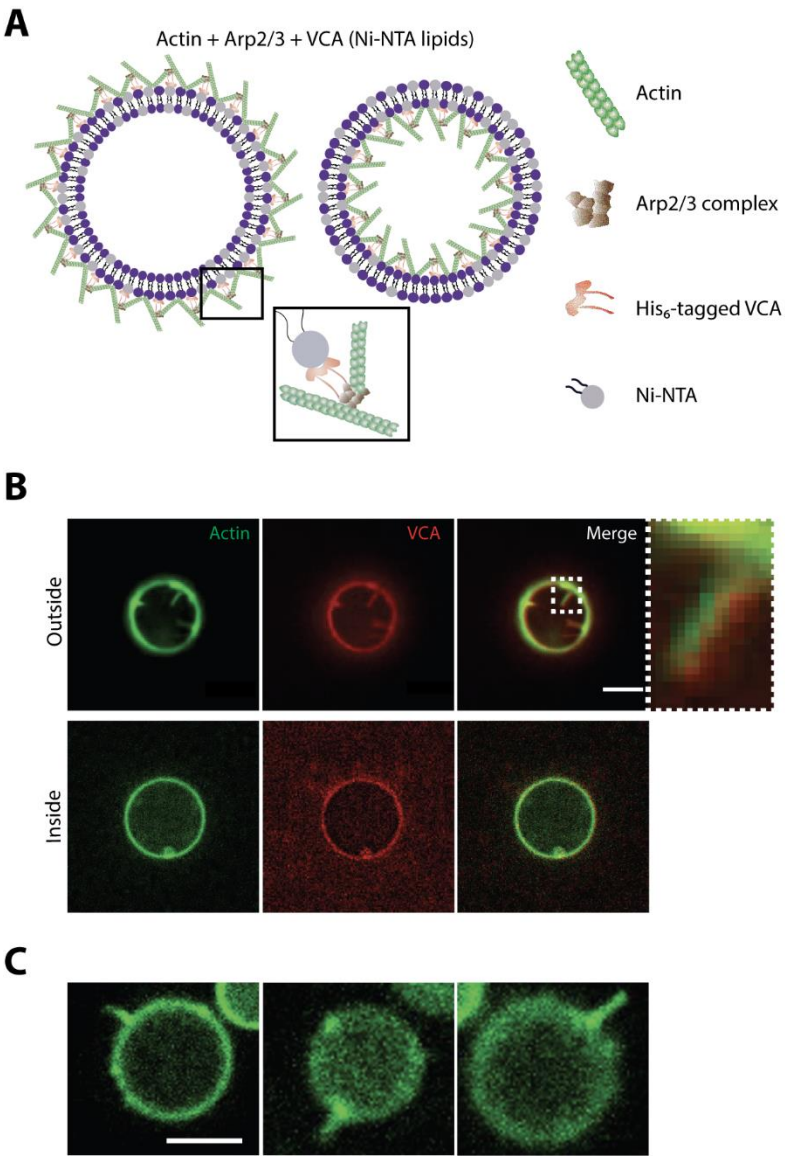

Figure 4-1 Actin cortex reconstitution (A) Schematic representation of two different approaches of actin cortex reconstitution. Actin cortex reconstitution from the outside (left) or inside (right) of GUVs by via activation of Arp2/3 complex using His_6-tagged VCA bound to Ni-NTA lipids (B) Representative confocal fluorescence images showing dendritic actin cortex (actin: 5.3 µM; Arp2/3 complex: 1 µM; His_6-tagged VCA: 0.5 µM) networks on the outer leaflet of the GUVs (top) or on the inner leaflet (bottom). Actin protrusions can be seen in GUV lumen (inset on top right). GUVs with a composition of 70/25/5 DOPC/cholesterol/DGS Ni-NTA are made by cDICE. Scale bar is 10 µm. (C) Representative confocal fluorescence images showing dendritic actin cortex (actin: 5.3 µM; Arp2/3 complex: 1 µM; His_6-tagged VCA: 0.5 µM) networks on the inner leaflet of the GUVs of a hyperosmotic condition with a difference of 70 mOsm between inner and outer solution.

After demonstrating we can form a dendritic network, we next sought to investigate how Arp2/3 activation might influence fascin-bundled network. For this, we compared encapsulated fascin-bundled network known to deform membranes with and without non-membrane-bound dendritic actin networks (Figure 4-2A), which can be achieved by leaving out Ni-NTA lipids. We encapsulated fascin and actin at three different fascin-to-actin ratios of 1:2 (2.65 μM fascin), 1:10, and 1:20 in actin polymerization buffer in GUVs. At a high fascin concentration, we found that fascin-bundled actin frequently deformed the GUV membrane and GUV deformation reduced with decreasing fascin concentration from ~85% to ~60% of GUVs over 10 μm in diameter (Figure 4-2B, C). This indicates that elongation of stiff fascin-bundled actin is the driving force of GUV deformation. Inclusion of CapZ prevented the formation of long actin bundles and abrogated membrane deformation (not shown). By comparison, in the presence of Arp2/3-nucleated dendritic network, the appearance of bundled actin diminished and GUV deformation significantly reduced to less than 10% (Figure 4-2B,C). Since fascin and Arp2/3 complex compete for the same pool of actin inside GUVs, we expect bundle length to change when Arp2/3 complex was added. From 3D reconstructed image stacks, we skeletonized actin networks and quantified bundle lengths. From this analysis, as one would expect, we found that there was a significant decrease in the bundle length with decreasing fascin that coincided with a reduction of GUV deformation probability (Figure 4-2D). More importantly, formation of dendritic network drastically reduced actin bundle lengths for the two high fascin concentrations (Figure 4-2D). Our finding is in accord with previous findings (48,302) where bulk experiments showed that an increase in the concentration of fascin results in an increase in actin bundle length during co-assembly of actin networks by fascin and Arp2/3 complex. Consistent with this, we quantified the number of branch nodes in each reaction condition and found that there was an

increase in branching of bundles when Arp2/3 complex was added (Figure 4-3). Together, these observations support the idea that both fascin and Arp2/3 complex simultaneously compete for the limited pool of actin and thus leading to the inhibition of fascin-bundled actin protrusions that are otherwise prevalent when fascin is encapsulated alone with actin. It is worth pointing out that all reconstituted systems, whether bulk or confined, have finite amounts of proteins. In a confined system such as GUVs with a size of tens of microns, the pool of actin and actin binding proteins available is very different compared to a reconstitution system with polystyrene beads as the nucleating surface, even though such a bulk system also has a finite pool of proteins.

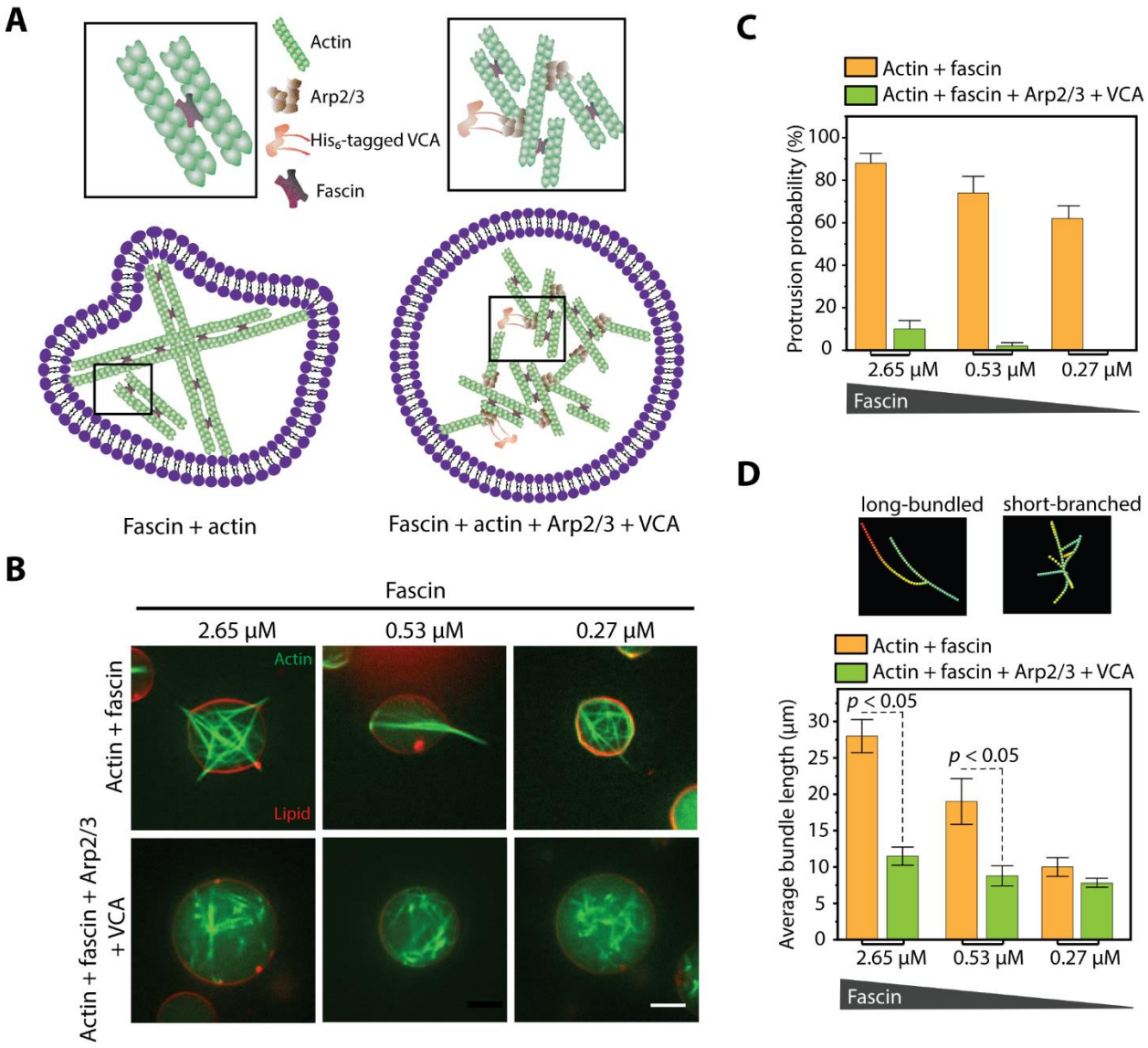

Figure 4-2 Co-encapsulation of fascin and Arp2/3 complex not bound to membrane (A) Schematic representation of actin bundles formed by fascin inside a GUV (left) and network formation by co-encapsulation of fascin with activated Arp2/3 complex not bound to the membrane (right). (B) Representative confocal fluorescence images of fascin-actin networks (5.3 µM actin) without (top) or with (bottom) Arp2/3 complex as a function of fascin concentration as indicated. In the cases where Arp2/3 complex was added, the concentrations of actin (5.3 µM), His_6-tagged VCA (0.5 µM), and Arp2/3 complex (1 µM) were kept constant for all three fascin

concentrations. GUVs had a composition of 70/30 DOPC/cholesterol. Scale bar is 10 μm. (C) The probability of protrusion formation for experimental conditions as indicated in (B). N > 25 for ≥2 replicates per category. Error bars denote counting error assuming a binomial distribution. (D) Length of actin bundles measured from 3D skeletonized filaments under different conditions shown in (B). Examples of what the traced bundles look like are shown. N > 25 for ≥2 replicates per category. Error bars represent standard error of the mean.

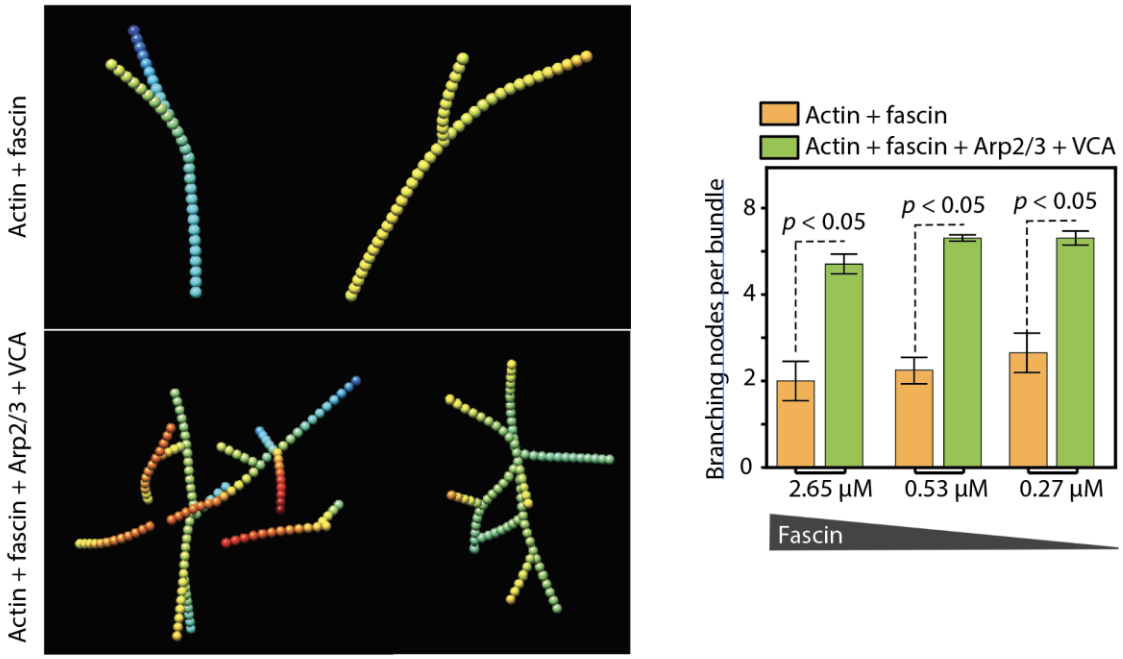

Figure 4-3 Network skeletonization Representative skeletonized bundles showing common form of branching for actin networks assembled by fascin-mediated bundling and actin network assembled by co-encapsulating both fascin and non-membrane-bound Arp2/3 complex (left). Branching nodes counted per bundle for different concentrations of fascin as indicated (right). N>25 for ≥2 replicates per category.

Since lumenal dendritic network strongly suppressed fascin-bunded network formation and the resultant GUV deformation, we wonder if membrane-bound dendritic network would have the same effect on bundled network formation. To test this, we encapsulated the same concentrations of Arp2/3 complex, His_6-tagged VCA, actin, and fascin used in the earlier experiment in actin polymerization buffer in Ni-NTA-containing GUVs. In contrast to the uniform actin cortex that we reported in Figure 4-1B when there is no fascin, we observed distinct network phenotypes that can be categorized into two major groups (Figure 4-4A). The first and most common structure appearing in more that 80% of the GUVs is polarization of membrane-bound dendritic actin aggregates. The second category, at about 20% of GUVs, had a cortex-like structure similar to GUVs with membrane-bound dendritic networks but without fascin added. We observed membrane-associated non-protruding bundles extending towards the lumen; this can occur with both polarized dendritic aggregates and cortex-like networks. Under this condition, we rarely saw GUV deformation.

Since it was clear now that dendritic and bundle network 'compete' in a confined environment, we asked whether reducing the amount of dendritic network might rescue GUV deformation by bundled actin. We fixed the concentrations of all proteins and varied the concentration of Arp2/3 complex from 2 μM to 500 nM and quantified the fraction of GUVs that exhibited membrane protrusion. With decreasing Arp2/3 complex concentration, we observed a decrease in cortex formation concomitant with an increase in bundle formation at the membrane (Figure 4-4B); interestingly, this resulted in an increase in protrusion probability from ~2% to ~20% (Figure 4-4C). This indicates that, although there is membrane binding of the dendritic network, the impact of fascin is more prevalent at lower concentrations of Arp2/3 complex due to decreased competition for finite actin inside the GUVs. To further illustrate this, when we

increased fascin concentration in the presence of membrane-bound dendritic networks, we observed a reduction of polarized dendritic aggregates and a concomitant increase of actin bundles (Figure 4-4B). These bundles were longer, straight and protrusive, reminiscent of fascin-bundled actin networks shown in Figure 4-2B. Consequently, the fraction of GUVs with protrusions increased to ~50% (Figure 4-4C). Altogether, these results support the idea that protrusions by bundled actin can be suppressed by dendritic actin networks, but a membrane-bound dendritic network can actually give rise to membrane deformation in the presence of fascin.

To further illustrate the role of competition for available actin monomers, we encapsulated the same concentrations of Arp2/3 complex, His_6-tagged VCA, and fascin, while varying the concentration of actin at 2.65 μM (half of previous concentration) and 10.6 μM (double the previous concentration). As shown in Figure 4-3B, the activity of fascin was suppressed at a low actin concentration resulting in predominantly uniform cortex and no protrusions were observed (Figure 4-4C); while a high actin concentration resulted in membrane-associated and polarized actin bundles. Ideses *et al.*, 2008 and Brill-Karniely *et al.*, 2009 describe that an increase in the length of individual actin filaments lowers the bending energy required to bring them to close proximity and transform them to thicker bundles through binding of fascin. This in in accord with our finding as increased concentration of actin facilitates the formation of longer filaments subsequently resulting in fascin-bundled actin.

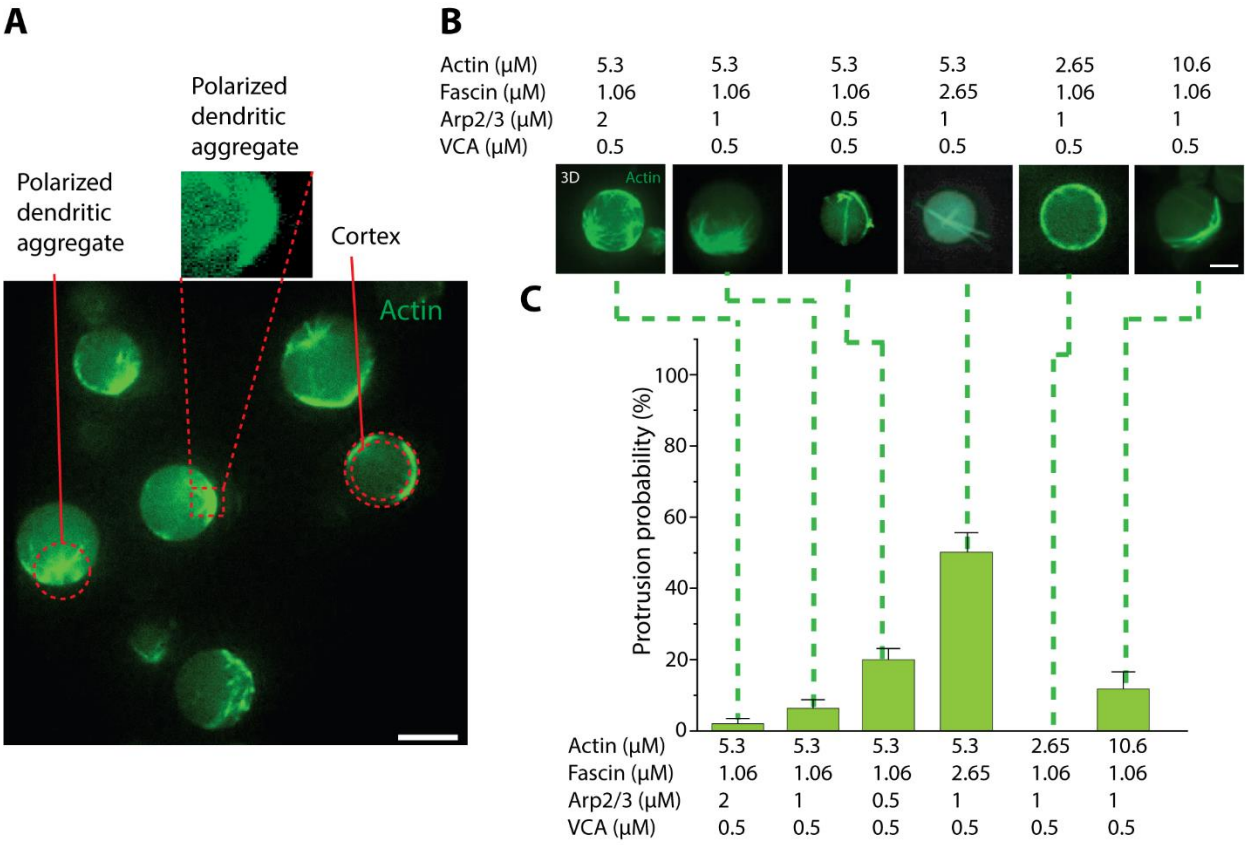

Figure 4-4 Co-encapsulation of fascin and membrane-bound Arp2/3 complex (A) A representative confocal fluorescence image showing distinct actin network structures by co-encapsulation of actin (5.3 μM), fascin (0.53 μM) and Arp2/3 complex (1 μM). Arp2/3 complex is activated by His_6-tagged VCA (0.5 μM) bound to the inner leaflet of the GUVs in the presence of 5% Ni-NTA lipid. (B) Representative confocal fluorescence images of actin networks inside single GUVs at different concentrations of actin, fascin, Arp2/3 complex, and His_6-tagged VCA as indicated. Scale bar is 10 μm. (C) Protrusion probability for each experimental condition as indicated and corresponding to images in (B). $N > 25$ for ≥2 replicates per category. Error bars denote counting error assuming a binomial distribution.

In summary, our work examined the interplay between dendritic and bundled actin networks by reconstituting them inside GUVs. We compared actin networks assembled by co-encapsulating fascin and Arp2/3 complex to actin networks assembled by encapsulating either of these actin binding proteins alone. Fascin is a short crosslinker that crosslinks actin filaments into parallel and tight bundles. Depending on the concentration of fascin and the size confinement space, fascin is known to induce membrane protrusions (307,314); whereas, membrane-bound activation of Arp2/3 complex nucleates actin to form a dendritic cortex (52). Consistent with prior work (52), reconstitution of a dendritic actin cortex on the external membrane leaflet results in membrane protrusions directed towards the GUV lumen. Interestingly, internally reconstituted dendritic cortex results in a uniform distribution of membrane-nucleated actin with no protrusions, and this has also been observed in a prior study using a different approach to activate Arp2/3 complex at the membrane (305). Localized deformations in the form of small changes in membrane curvature have been shown when reconstituting Arp2/3-nucleated cortex with regulated capping protein inside a GUV (309), yet no membrane protrusions were observed. The different outcomes from nucleating dendritic actin between outside and inside GUVs could be due to the curvature; from the outside, actin network is convex to the membrane whereas from the inside, actin network is concave to the membrane. In the convex case, the direction of actin protrusive force is in the same direction of membrane tension and thus making protrusion possible. Simon *et al.* reported that actin protrusions on GUVs can be tuned by membrane tension (308); and our experiments show that lowering membrane tension results in the emergence of protrusive actin structures from dendritic networks can be reconstituted from inside GUVs.

By co-encapsulating fascin and Arp2/3 complex, our results revealed that dendritic network formed in the GUV lumen suppresses the assembly of protrusive fascin-bundles by shortening bundle length and possibly by increasing branching of actin filaments, thereby stunting bundle growth. When the dendritic networks were assembled at the GUV membrane instead, we found emergence of polarized dendritic aggregates with membrane-associated bundles. It was not immediately clear as to why polarized aggregation of networks were prevalent; however, similar non-homogeneity in actin cortex has been shown with increasing crosslinker concentration (315,316). Reconstituted inside water-in-oil droplets, Tan *et al.* showed the transition from a uniformly distributed Arp2/3-nucleated actomyosin cortex into asymmetrically aggregated cortex by increasing the concentration of α-actinin. In the case of encapsulating fascin and membrane-activated Arp2/3 complex, we show that formation of polarized dendritic aggregates is common. Moreover, decreasing the concentration of Arp2/3 complex and increasing the concentration of fascin results in higher protrusion probability. This finding may have implications consistent with the convergent elongation model for filopodia initiation in cells, which posits the transition from a lamellipodia to filopodia by reorganization of dendritic network to initiate fascin-mediated actin bundling (317). To conclude, we speculate that the inhibition of actin bundle-induced membrane protrusions is due to competition for finite actin available inside the vesicles. This finding would be distinct in our experimental system compared to previous studies that did not have confinement. Distinct actin network architectures due to competing actin crosslinkers have been observed by reconstituting fascin and α-actinin (318). The precise mechanism by which protrusions are inhibited and how cortex aggregation is formed are still open for investigation. Future work can potentially dissect the dynamics of actin crosslinkers altering a uniform cortex into asymmetric aggregates.

4.5 Acknowledgement

Human fascin construct was a kind gift from Danijela Vignjevic (Curie Institute, France). We acknowledge helpful discussion with Nir Gov (Weizmann Institute of Science, Israel). The work is supported by the National Science Foundation (CBET-1844132). N.H.W. is supported by NIH's Microfluidics in the Biomedical Sciences Training Program (NIH NIBIB T32 EB005582). A.P.L. acknowledges support from National Institutes of Health (R01 EB030031-01) and National Science Foundation (MCB-099332).

Chapter 5 Differential Regulation of GUV Mechanics via Actin Network Architectures

This chapter was published in Biophysical Journal (2023). Author contributions: N.H.W. and A.P.L. designed research. N.H.W., B.W. and S.V. performed research. B.W. and S.V. contributed analytic tools. N.H.W. analyzed data. N.H.W., B.W., S.V., and A.P.L. wrote the paper.

5.1 Abstract

Actin networks polymerize and depolymerize to construct highly organized structures, thereby, endowing the mechanical phenotypes found in a cell. It is generally believed that the amount of filamentous actin and actin network architecture determine cytoplasmic viscoelasticity of the whole cell. However, the intrinsic complexity of a cell and presence of endogenous cellular components make it difficult to study the differential roles of distinct actin networks in regulating cell mechanics. Here, we model a cell by using giant unilamellar vesicles (GUVs) encapsulating actin filaments and networks assembled by various actin crosslinker proteins. Perturbation of these cytoskeletal vesicles using AC electric fields revealed that deformability depends on actin network architecture. While actin-free vesicles exhibited large electromechanical deformations, deformations of GUVs encapsulating actin filaments were significantly dampened. The suppression of electrodeformation of actin-GUVs can be similarly recapitulated by using aqueous PEG 8000 solutions at different concentrations to modulate solution viscoelasticity. Furthermore, alpha actinin-crosslinked actin networks resulted in

decreased GUV deformability in comparison to actin filament-encapsulating GUVs, and membrane-associated actin networks through the formation of dendritic actin cortex greatly dampened electrodeformation of GUVs. These results highlight the organization of actin networks regulates the mechanics of GUVs and shed insights into the origin of differential deformability of cells.

5.2 Introduction

The cell's ability to change shape to support cellular functions such as migration and division, and its ability to resist deformation to sustain structural integrity, depends on the cytoskeleton. Among different types of cytoskeletal polymers, actin filaments assemble into various networks aided by actin binding proteins that form large-angle-crosslinks, bundles, and branches (325,326). Although the flexural rigidity of actin filaments is as much as three orders of magnitude lower compared to that of microtubules (327), assembly of actin filaments into highly organized and dynamic networks gives rise to enhanced viscoelastic property (325,328,329). As a result, actin networks endow the mechanical phenotype of cells by differentially regulating the elasticity and cytoplasmic viscosity of cells (330). Prior research have linked the mechanical property of cells to the actin network (329,331). For example, it is reported that increased deformability of ovarian cancer cells, due to their actin organization, is directly correlated to metastatic transformation (332,333). Furthermore, retraction of epithelial cells to break cell-cell junction as a result of local actin disruption is linked to extravasation of cancer cells during metastatic invasion (334,335). It is also known that cytoplasmic viscosity of red blood cells affects their dynamics inside microvasculatures (336,337). The connection between cell

mechanics and cellular processes has led to substantial interest in perturbing the cytoskeleton as a means to regulate cellular processes.

Due to the simple experimental set up, many have utilized electromechanical perturbation of cells using both direct current (DC) and alternating current (AC) electric fields. Earlier studies using electroperturbation dealt with the interaction of pulsed DC electric field and cell membranes that resulted in electropermeabilization and electroporation (338). Controlled modulation of DC electric fields resulted in the formation of enlarged pores permitting the introduction of large molecules that are otherwise not permeable through cell membrane, thus giving rise to various applications including DNA transfection, drug delivery, cancer therapy (339–341), and gene therapy (342,343). Strong AC fields, on the other hand, are known to induce cellular deformation. The semi-permeable lipid bilayer of a cell's plasma membrane can be thought of as an electrical insulator. When an electric field is applied, ions inside a cell undergo charge separation resulting in dielectrophoresis due to a non-uniform electric field (344). Depending on the electric field strength and conductivity of the suspension environment, dielectrophoretic forces result in the deformation of cells (198). Many studies have resorted to AC electrodeformation to measure apparent stiffness of red blood cells and platelets (345,346), viscoelasticity of cancer cells (347,348), and to study the effect of actin depolymerization on the relaxation of electrodeformed cells (185).

Although prior studies have revealed the mechanical properties of cells are intimately tied to their actin networks, the differential role of actin, in the form of filaments and networks, on the deformability of cells remain incompletely understood. The intrinsic complexity of cells and numerous endogenous components make it difficult to study the differential roles of actin networks as a function of actin crosslinkers (50). Giant unilamellar vesicles (GUVs) present a

unique platform to model and reconstitute cellular processes in a membrane-confined environment (349). This experimental approach has been used to study the assembly of different types of actin networks (350), how actin network induces membrane remodeling (52,75,82,83,227), and to reveal actin binding protein competition and cooperation in actin network assembly (351,352). Others have also reconstituted a cortex-like shell in GUVs and measured their responses to mechanical compression (105).

The responses of GUVs to applied electric field have been extensively investigated (191–193,353–356). Subject to strong DC pulses, similar to cells, macropores formed in GUVs when the transmembrane potential threshold was exceeded (193). Vesicle closure after poration, curvature relaxation and other electrical properties of GUVs have been characterized for different bilayer compositions and salt concentrations used for both the external medium and the GUV lumen (193,194,353,357,358). Furthermore, it has been shown that when induced by a DC pulse, GUVs with an actin cortex have suppressed membrane permeability compared to cortex-free GUVs (106), presumably due to smaller and/or less macropore formation. Similar to cells, strong AC electric fields forced spherical GUVs to assume elliptical shapes with the major axis either parallel (prolate) or perpendicular (oblate) to the electric field (359). GUVs undergo these shape transformations depending on the salt concentration ratio between the GUV lumen and the solution outside of GUVs, and electric field strength and frequency (192,359,360). AC field electrodeformation transitions have been theoretically modeled under different conditions (361–363), and experimental studies based on electrodeformation have investigated bilayer properties such as membrane bending rigidity and bilayer viscosity (98,193). Although GUV membrane

properties have been well studied and characterized, how the mechanics of GUV is influenced by different actin network architectures remains incompletely understood.

Here, we investigate the effect of encapsulated actin filaments and crosslinked actin networks on the electrodeformability of GUVs in response to AC electric fields. We encapsulated actin-free buffer solution and filamentous actin inside GUVs. Subject to an AC electric field, we observed a significant difference in deformability between the two conditions. We modulated the viscosity of GUV lumen and found that the deformability of GUVs correlated with lumenal viscosity, a condition that mimics filamentous actin. Furthermore, crosslinked or membrane-cortex actin networks, at the same concentrations of F-actin, further dampened GUV electrodeformation. Overall, our results reveal that the differential mechanical properties of GUVs, and by extension to cells, can be modulated by actin network architectures.

5.3 Materials and Methods

Reagents

Purified actin was purchased (Cytoskeleton, Inc.). ATTO 488 actin was purchased from Hypermol (Germany). Actin crosslinker alpha-actinin from rabbit skeletal muscle and Arp2/3 complex from bovine brain were purchased form Cytoskeleton, Inc.. Hexa-histidine-VCA (His_6-tag VCA) was purified as described previously (352). General actin buffer (G-buffer) was prepared at 10x concentration and consists of 50 mM Tris-HCL pH 8.0, and 2 mM $CaCl_2$. Actin was diluted from a stock concentration of 10 mg/ml to a working concentration using G-buffer + 0.2 mM ATP and 0.5 mM DTT. Actin polymerization buffer (F-buffer) was prepared at 10x concentration and is composed of 500 mM KCl, 20 mM $MgCl_2$, and 10 mM ATP. 1,2-dioleoyl-sn-glycero-3-phosphocholine (DOPC), 1,2-dioleoyl-sn-glycero-3-[(N-(5-amino-1-

carboxypentyl)iminodiacetic acid)succinyl] (nickel salt) (DGS-NTA(Ni)), and cholesterol were purchased from Avanti Polar Lipids. PEG 8000 was purchased form Fisher Scientific. Density gradient medium (Optiprep) and other chemicals were purchased from Sigma Aldrich.

Electrodeformation setup

A simple homemade electroperturbation chamber was assembled to conduct GUV electrodeformation experiments. The setup is comprised of adhesive electrode tape and 3 x 1 in coverslip. Two copper tapes were used as electrodes and were attached to one face of the coverslip in a parallel manner with gaps ranging from 200-300 μm. Sinusoidal AC electric field was applied using an Agilent 33120A (Keysight Technologies, USA) function generator between electrodes adhered to coverslip. We used a fixed length of electrode tapes, and using voltmeter (Fluke, USA), we measured potential of 6.7 V when applying 10 V peak to peak sinusoidal AC. Lower than RMS voltage measured at the electrodes end may be attributed to resistance from adhesive and tape length. To apply identical AC field between slightly varying chambers between different devices, applied voltage was adjusted accordingly to the exact measured gap between the two electrodes such that 30 kV/m is the applied field strength between the electrodes. During electroperturbation experiments, GUVs were dispensed between the electrodes. The height of the copper tape, which is ~100 μm, was higher than nearly all sizes of generated and analyzed GUVs, therefore yields a uniform electric field across the length of the chamber. For all experiments, duration of AC field was kept within 3-4 seconds.

GUV generation

Encapsulation of aqueous material inside GUVs was achieved using the modified cDICE

method (70). As described previously (352), a 3D printed cDICE chamber is mounted onto a table top stirring motor and rotated at 1200 rpm. First, 770 µL outer aqueous glucose solution, of varying concentrations depending on osmotic condition, is dispensed into the chamber. For iso-osmotic conditions, concentration of glucose is tuned such that its osmolarity matches the measured osmolarity of the inner solution, whereas for hyperosmotic conditions (flaccid GUVs), the outer glucose solution is 400 mOsm higher than inner solution. Next an adequate amount of oli/lipid mixture is dispensed into the chamber. The lipid composition used in all conditions, except for reconstituting actin cortex, is 70 mol% DOPC with the addition of 30 mol% cholesterol. During reconstitution of the actin cortex, 5 mol% DGS NTA(Ni) was added to the lipid composition while lowering cholesterol to 25 mol%. Oil is composed of 80% silicon oil and 20% mineral oil. When oil and lipid solutions are mixed, a two-phase dispersion emerges due to the emulsification of mineral oil containing lipid aggregates. Upon the addition of the lipid/oil mix to the chamber, it forms an interface saturated by lipid aggregates. Separately, 770 µL of oil/lipid mix is dispensed in to an epitube containing 20 µL of prepared inner solution (encapsulant) and pipetted up and down until the solution becomes cloudy indicating formation of lipid monolayer saturated encapsulant emulsions. Finally, the solution is transferred to the cDICE chamber. Due to centrifugal forces generated by the rotating chamber, encapsulant emulsions are shuttled through the oil/lipid mix into the outer solution. When emulsions cross the lipid saturated interface, a second layer of lipid zips the emulsions and forms GUVs suspended in the outer aqueous solution.

Inner solution preparation

Various inner solution conditions were reconstituted to conduct GUV electroperturbation

experiments. Each condition contains 7.5% density gradient medium to facilitate GUV sedimentation. In viscosity contrast experiments, PEG 8000 was dissolved in DI water at specified concentration (2%, 4%, and 8% w/v). To reconstitute actin-polymerization-buffer GUVs, inner solution contained 1x F buffer and 3 mM ATP. For reconstitution of F-actin GUVs all components in the inner solution of actin-polymerization-buffer GUVs are preserved with the addition of 5.3 μM actin and 0.53 μM ATTO 488 actin. The electrical conductivity of G-buffer and F-buffer used to reconstitute globular actin and filamentous actin, respectively, was measured using a benchtop conductivity meter Orion Star A212 (Thermo Scientific, USA). Furthermore, viscosity measurements of actin and buffer solutions were conducted using Discovery HR-2 rheometer (TA Instruments, USA) at a shear rate of 100 s^{-1} and 25 °C. To reconstitute alpha-actinin-crosslink GUVs, all ingredients used to reconstitute F-actin were mixed and incubated for 15 minutes in ice. Then, 1.77 μM of alpha-actinin was added to the solution. Addition of alpha-actinin, or any actin crosslinker, should be immediately followed by the last step of the cDICE GUV generation method, which is making lipid monolayer stabilized inner solution emulsions by mixing actin solution with lipid/oil mix followed by dispensing into the cDICE chamber. For reconstitution of actin cortex, the lipid composition is slightly altered by the addition of 5 mol% DGS NTA(Ni). Similar to alpha-actinin-crosslinked actin network reconstitution, F-actin components were incubated in ice for 15 minutes. Then actin nucleation promotion factor, 0.5 μM His_6-tagged VCA, is added followed by addition of 0.5 μM of Arp2/3 complex. When confined by the lipid bilayer compartment, His_6-tagged VCA binds to nickel domain of DGS NTA(Ni) and activates Arp2/3 to form dendritic actin networks restricted at the lipid bilayer membrane.

Imaging

In our experiments, we used two different imaging setups: bright-field imaging equipped by a high-speed camera and fluorescence imaging using a confocal microscope. To acquire dense data points yielding contentious deformation profile of GUVs when subject to AC electric field, Olympus CKX41 (Olympus, USA) inverted microscope equipped with Phantom Miro ex1 (Phantom High Speed, USA) high-speed camera was used. Images were taken at a rate of 1200 fps using a 40x/0.55 NA objective lens and acquired using phantom camera control (PCC 1.2) software. To observe actin dynamics in response to electric field, we used an Olympus IX-81 inverted microscope equipped with a spinning disk confocal (Yokogawa CSU-X1), OBIS LS/LX lasers (Coherent, USA) and an iXON3 EMCCD camera (Andor Technology, USA). Each component was controlled by using MetaMorph (Molecular Devices, USA). Images were acquired using an oil immersion 40x/1.3 NA objective. While GUV samples were inside the electroperturbation chamber and subject to an AC electric field, ATTO 488 actin was excited using 488 nm laser at an exposure time of 170 ms, and time-lapse images were taken every 200 ms. Maximum deformation measured from confocal images were, along with bright-field images, used for statistical analysis of each GUV condition.

Statistical analysis

Using Origin software**,** one-way ANOVA tests were used to determine the statistical significance of major axis to minor axis ratios across different conditions. Furthermore, p values were determined using two-tailed Student's t-test. $p < 0.05$ is considered statistically significant. Number of vesicles measured range from 10 to 15 with at least three different devices used for a given condition.

5.4 Results

Actin network reconstitution in GUVs and electroperturbation device

To reconstitute various actin networks in cell-sized lipid vesicles, the modified continuous droplet interface crossing encapsulation (cDICE) method (70) (Fig. 5-1A) was used. In the presence of actin crosslinkers, actin networks formed rapidly and the modified cDICE method renders rapid encapsulation of actin networks to permit network assembly post-encapsulation. Actin filaments, components of actin cortex, and large-angle actin crosslinker (Fig. 5-1B) were encapsulated into heterogeneously sized GUVs composed of 70 mol% DOPC and 30 mol% cholesterol. 5 mol% DGS-NTA(Ni) was added when reconstituting actin cortex. Actin cortex was assembled by activating Arp2/3 complex at the inner leaflet of bilayer membrane via constitutively active His_6-tagged VCA domain of neural Wiskott Aldrich

syndrome protein (N-WASP). Crosslinked networks were formed using the large-angle actin crosslinker alpha-actinin.

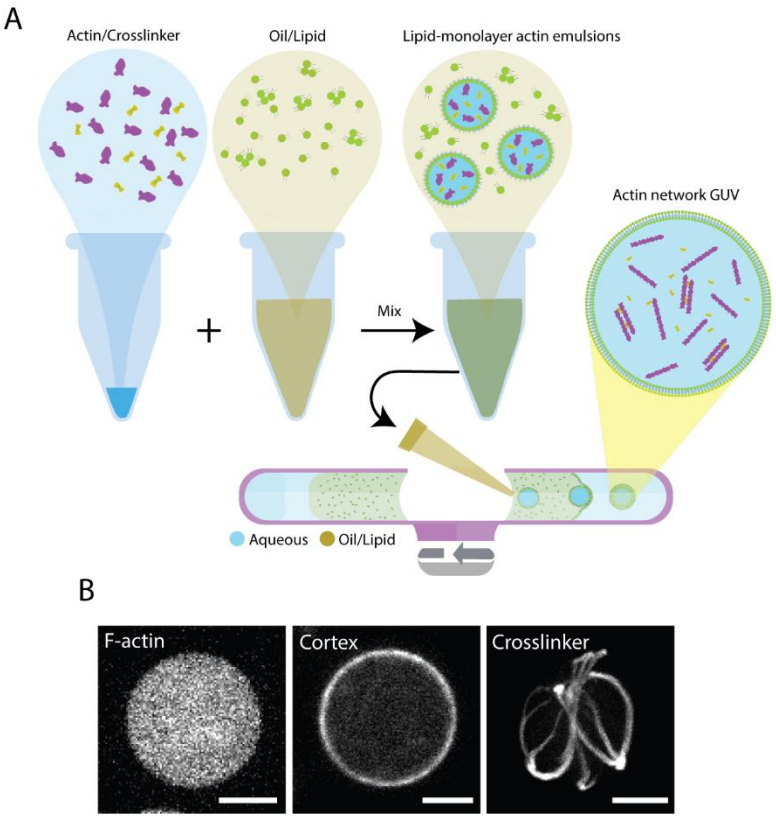

Figure 5-1 Reconstitution of different actin networks inside GUVs (A) Schematic of the modified cDICE method. Purple shapes represent actin monomers. Green shapes represent lipids. Yellow shapes, shown in actin/crosslinker solution schematic, represent an arbitrary actin crosslinker. (B) Representative images of actin network GUVs. (Left) Representative confocal image of encapsulated F-actin inside GUVs. (Middle) Arp2/3-complex assembled an actin cortex and associated to GUV lipid bilayer membrane. (Right) Aster-like actin network assembled by alpha-actinin encapsulated inside a GUV. Actin is labeled with ATTO 488 actin in all images. Scale bars, 10 μm.

A simple electroperturbation device with two parallelly aligned and spaced electrodes was assembled on a glass slide to subject GUVs to AC electric fields at 5 kHz (Fig. 5-2A, Fig 5-S1A,B). Electroperturbation experiments were performed by dispensing GUVs into the device chamber (i.e. space between electrodes), then applying a sinusoidal AC wave from a function

generator. Transition of vesicles from undeformed to deformed to undeformed states following a 30 kV/m AC field at 5 kHz for a duration of 3-4 s was captured using a high-speed camera mounted on a brightfield optical microscope. This setup allowed us to analyze fast real-time GUV shape transformation at a high temporal resolution.

Actin filaments dampen electrodeformability of GUVs

First, we validated our electroperturbation setup by replicating known GUV electroperturbation responses under different ionic conditions. During AC field electroperturbation, the orientation of elliptical deformation depends on the conductivity ratio $\Lambda = \frac{\sigma_{in}}{\sigma_{ex}}$, where σ_{in} is the conductivity of inner solution and σ_{ex} is the conductivity of outer solution (360). GUVs assume a prolate shape when $\Lambda > 1$ and subjected to a low frequency field and an oblate shape when $\Lambda < 1$ and subjected to a high frequency field. By tuning NaCl concentration in the inner and outer solutions and applying 30 kV/m, GUVs transformed from spherical to prorate (not shown) and spherical to oblate (not shown) shapes for $\Lambda > 1$ with a low frequency field (1kHz) and $\Lambda < 1$ with a high frequency field (50 kHz), respectively. Prolate deformations have major axis of ellipse parallel to the field direction, whereas oblate deformations have ellipse major axis orthogonal to the electric field.

To examine the impact of actin on GUV mechanics, we next investigated GUV deformability with and without the presence of encapsulated actin filaments (Fig. 5-2). As a control, we encapsulated actin polymerization buffer, without the presence of actin, under iso-osmotic condition. Actin polymerization buffer (hereon referred to as F-buffer) contains 1x F-buffer, 3 mM ATP, and 7.5% density gradient medium. This reaction condition contains all the reagents that are used to reconstitute filamentous actin (F-actin) and serves as the benchmark

control against actin-containing GUVs. The conductivity ratio between inner and outer solution was maintained since the salt concentrations were similar for the two conditions. Considering buffers used to reconstitute actin contain tens of mM of salt molecules, we have no reason to believe charged proteins like actin at concentrations below 10 μM will result in a significant change in conductivity. The conductivity of G-buffer and F-buffer solutions were ~1.2 and ~8.0 mS/cm, respectively (Fig. 5-S2), but we were unable to measure the conductivity of F-actin solution due to the volume required for conductivity measurements with our setup. As expected, GUVs with F-buffer assumed prolate deformation (Fig. 5-2B top). To show that the electrodeformation is not due to GUV deflation, which can induce exaggerated deformability during electroperturbation, a control electroperturbation experiment was performed on flaccid GUVs (from hyper-osmotic condition) containing F-buffer (Fig. 5-2B bottom). This resulted in greatly increased prolate deformation of GUVs compared to their iso-osmotic counterparts. We also observed an extended delay in relaxation time for flaccid GUVs. Extended relaxation time for flaccid vesicles may be attributed to excess membrane surface area with greater membrane undulation suppressing a quick recovery. As a control, when globular actin (G-actin) is

encapsulated instead, their maximum deformability is more similar to the case of F-buffer than F-actin (Fig 5-S3).

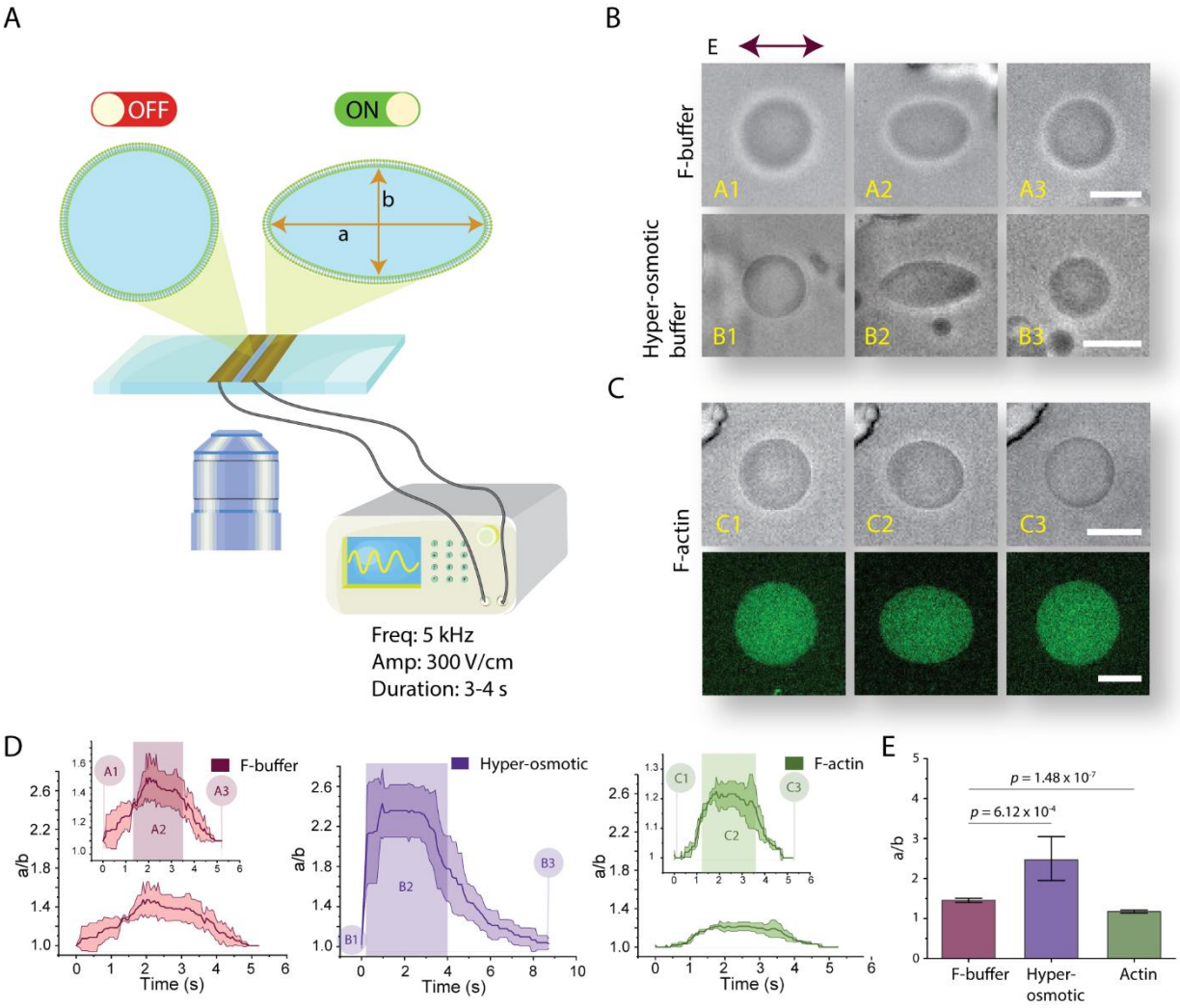

Figure 5-2 Electroperturbation of filamentous actin GUVs (A) Schematic of the electrodeformation setup mounted on an inverted microscope. A function generator is operated at 30 kV/m at 5 kHz and a sinusoidal wave was applied for a duration of 3-4 seconds. Schematic shows electrodes adhered onto a coverslip. GUVs transform from a spherical shape to an ellipse when the electric field is applied. (B) GUV deformation is dependent on osmolarity difference between inner and outer solutions. (Top) Brightfield images of electric field-induced shape transformation of actin-polymerization-buffer GUVs. (A1) GUV at an undeformed state prior to

AC field application; (A2) Steady-state deformation of GUVs during electoperturbation; (A3) actin-polymerization-buffer GUV post electrodeformation recovery. (B1, B2, B3) Electrodeformation of actin-polymerization-buffer GUV in a hyper-osmotic condition (flaccid GUV). (B2) shows exaggerated prolate deformation with pointed ends. (C) Electrodeformation of a F-actin GUV. (C2) shows visually apparent dampened deformation compared to A2 and B2. (C bottom) Representative fluorescence image of F-actin GUV labeled with ATTO 488 actin. (D) Deformation profile of GUV conditions in B and C for F-buffer, hyper-osmotic buffer, and F-actin conditions, as indicated. Labels (A1, A2, and A3…etc) correspond to GUV transformation stages during electroperturbation. Shaded rectangular box denotes approximate duration of electric field application. Shaded areas in the traces in each of the plots indicate ± SD, n = 3. (E) Comparison and statistical analysis of maximum GUV deformation of each GUV condition as indicated. Data represent mean maximum deformation and error bars denote ± SE. N_{buffer} = 11, N_{hyper} = 14, and N_{actin} = 12. Scale bars, 10 μm.

Next, we reconstituted F-actin inside GUVs. Strikingly, when applying the same AC electric field to GUVs containing 5.3 μM F-actin in iso-osmotic condition, deformation was significantly dampened (Fig. 5-2C). Comparing each of the above 3 conditions, the largest maximum mean deformation a/b ~ 2.42 (Fig. 5-2D middle) was attained by flaccid vesicles, followed by F-buffer GUVs at a/b ~ 1.45 (Fig. 5-2D left), and the largest deformation resistance resulted in maximum mean deformation a/b ~ 1.23 for F-actin GUVs (Fig. 5-2D right). As shown in Figure 5-2E, the average maximum deformation from a population of F-buffer GUVs was significantly larger than that of F-actin GUVs. Additionally, we encapsulated F-actin at 2.65 μM and 10.6 μM (Fig 5-S4) and found that GUVs were more deformable under the same

electroperturbation conditions at 2.65 μM F-actin compared to 5.3 μM and 10.6 μM although differences between 5.3 and 10.6 μM F-actin conditions were not significant (Fig 5-S4B). In our analysis, we selected GUVs of size range 10-30 μm that are representative of the GUV population generated using the modified cDICE method, and found no size dependent correlation between GUV size and GUV deformability (Fig. 5-S5).

Considering known GUV parameters and their respective electroperturbation responses, our observation was not readily explained. In each of the above cases, there were no observed instances of electroporation to affect deformation behavior which can commonly be identified by loss of volume, loss of contrast, or by micron-sized membrane ruptures that can be observed at high magnifications. The conductivity ratio, lipid bilayer composition, and osmolarity between F-buffer GUVs and F-actin GUVs were the same. Thus, the distinct deformability behaviors can only be attributed to the material property of the GUV lumen. As a viscoelastic material, previous works have shown that a F-actin solution has an increased viscoelasticity compared to aqueous buffer solutions similar to our polymerization buffer (~1 mPa.s) and the viscosity increases further with increasing actin concentration (364). We confirmed these by measuring the viscosity of F-buffer (1.33 mPa.s) and 5.3 μM F-actin (2.21 mPa.s) solutions with added 7.5% density gradient medium (Fig. 5-S6). Thus, we hypothesized that the dampened GUV deformation was due to changes in GUV lumenal viscoelasticity.

Changes in lumenal viscosity determines the electrodeformability of GUVs

To investigate the role of change in viscoelastic property GUV lumen on electrodeformability, we encapsulated poly(ethylene glycol) (PEG) polymer solutions, which are known to be viscoelastic (365,366). PEG 8000 solutions with concentrations ranging from 2-8%

w/v were encapsulated inside GUVs. Osmolarity of the outer solution was matched to the measured osmolarity of each aqueous PEG 8000 solutions in order to maintain iso-osmotic conditions. When GUVs containing 2% PEG 8000 were subjected to 30 kV/m AC field at 5 kHz for a duration of 3-4 seconds (Fig. 5-3A top), the maximum mean deformation was measured at a/b ~ 1.3 (Fig. 5-3B left). At 4% PEG 8000, the maximum mean deformation reduced to a/b ~ 1.14 (Fig. 5-3A middle, Fig. 5-3B right). In GUVs with 8% PEG 8000, no measurable GUV deformation was observed (Fig. 5-3A bottom), and thus there is no deformation profile included for the 8% PEG condition. Our results clearly demonstrated dampening of GUV deformation with increasing lumenal viscosity (Fig. 5-3C), consistent with our initial hypothesis that dampened deformation in F-actin GUVs is related altered lumenal viscosity.

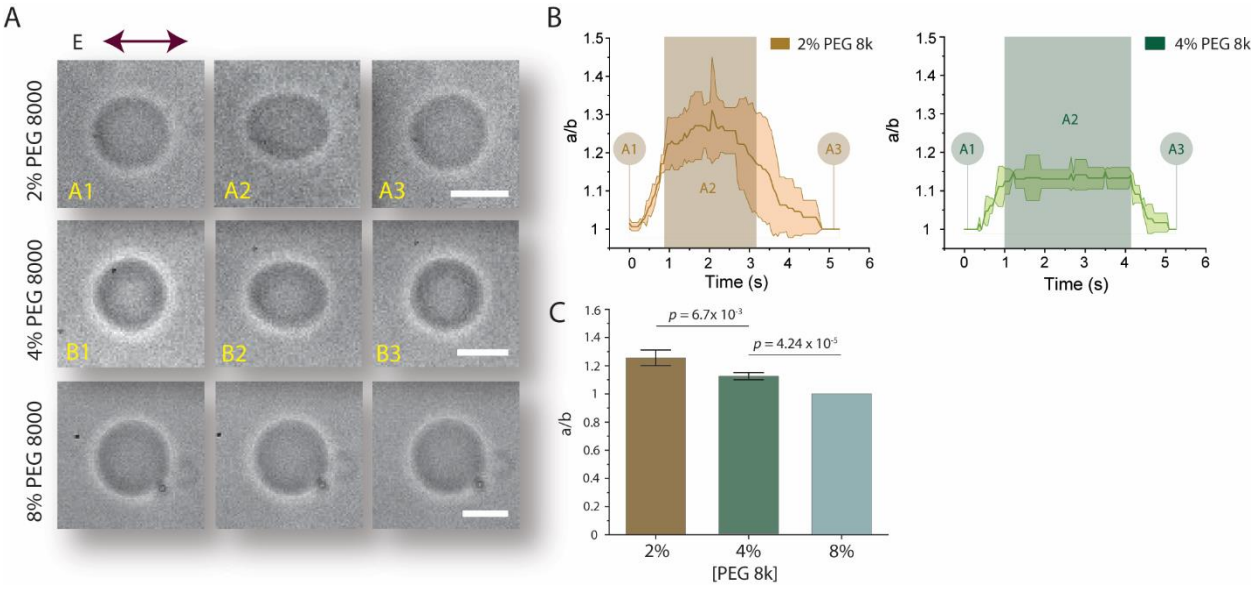

Figure 5-3 Relationship between viscosity contrast and electrodeformability of GUVs

Different PEG 8000 concentrations were encapsulated inside GUVs to vary viscosity contrast between GUV lumen and outer solution. (A) Brightfield images showing PEG 8000 GUV shape transitions from undeformed to elliptically deformed to spherical recovery. (Top) Electroperturbation of 2% w/v PEG 8000 GUV. (A1) A PEG 8000 GUV at an undeformed state

prior to AC field application. (A2) Steady-state deformation of GUVs during electoperturbation. (A3) GUV post electrodeformation recovery to assume spherical shape. (B1-B3) 4% w/v PEG 8000 GUV electrodeformation. (Bottom) Electroperturbation of 8% w/v PEG 8000 GUV. (B) Deformation profile of 2% and 4% w/v PEG 800 GUVs, n = 3. Shaded rectangular box denotes approximate duration of electric field application. Shaded areas in the traces in indicate ± SD. (C) Comparison and statistical analysis of maximum GUV deformation of each GUV conditions indicated. Note that max a/b ratio of 8% was 1 for all vesicles analyzed and thus has no error bars. Data represent mean maximum deformation and error bars denote ± SE. $N_{2\%}$= 13, $N_{4\%}$ = 11, and $N_{8\%}$ = 12. Scale bars, 10 μm.

The degree of deformability of 5.3 μM F-actin GUVs falls between deformability of GUVs encapsulating 2% PEG and 4% PEG solutions, and directly corresponds to the measured viscosity of F-actin solution at this concentration (2.21 mPa.s) that is in between the viscosity of 2 and 4% PEG solutions. Although these observations may be intuitive and in alignment with our initial hypothesis, to our knowledge, there are no prior studies that exploited cell-mimicking confinements like GUVs to investigate the effect of lumenal material property on their electrodeformability. Thus, here we illustrate a mechanism for cells to maintain structural

integrity by only modifying viscosity without necessitating crosslinking of cytoskeleton using additional actin binding proteins.

In silico investigation on the role viscosity contrast on GUV electrodeformability

We developed a computational method to further investigate the role of viscosity contrast (detailed in SI). Numerical experiments are set up by placing the GUV in an AC field $\boldsymbol{E}_\infty(t)$ with magnitude E_0, such that

$$\boldsymbol{E}_\infty(t) = E_0 \sin(2\pi\omega t)\,\hat{\boldsymbol{x}}$$

where ω is the AC field frequency. Using the GUV radius a as the characteristic length scale and the membrane charging time $t_m = aC_m/\sigma_{ex}$ as the characteristic time scale, we define the following dimensionless parameters:

viscosity ratio:	$\eta = \mu_{in}/\mu_{ex},$
conductivity ratio:	$\Lambda = \sigma_{in}/\sigma_{ex},$
electric field strength:	$\beta = \epsilon_{ex}E_0^2 t_m/\mu,$
AC field frequency	$\Omega = \omega t_m.$

An AC field of frequency Ω = 0.5 and strength β = 10 is applied at t = 0 and we measure the aspect ratio a/b of the GUV over time. We observe that, for a fixed conductivity ratio Λ, the prolate deformation of the GUV is delayed as the viscosity contrast η is increased (Fig. 5-4A). Additional experimental results, shown in Figure 5-S7**,** indicate that fixing the conductivity ratio Λ of 2% (Fig. 5-S7A) and 4% PEG 8000 (Fig. 5-S7B) concentrations to 0.9, by addition of 7.5 mM NaCl to 4% PEG 8000 inner solution, preserved deformation dampening as a result of

increasing η (Fig. 5-S7C,D,E). For a fixed viscosity contrast, the prolate deformation happens only when the conductivity ratio Λ is large enough (Fig. 5-4B). Consequently, dampening of the prolate deformation is observed as a combined effect of increasing η and decreasing Λ (Fig. 5-4C), which is consistent with the experimental results using PEG 8000 solutions with increasing concentrations (Fig. 5-3).

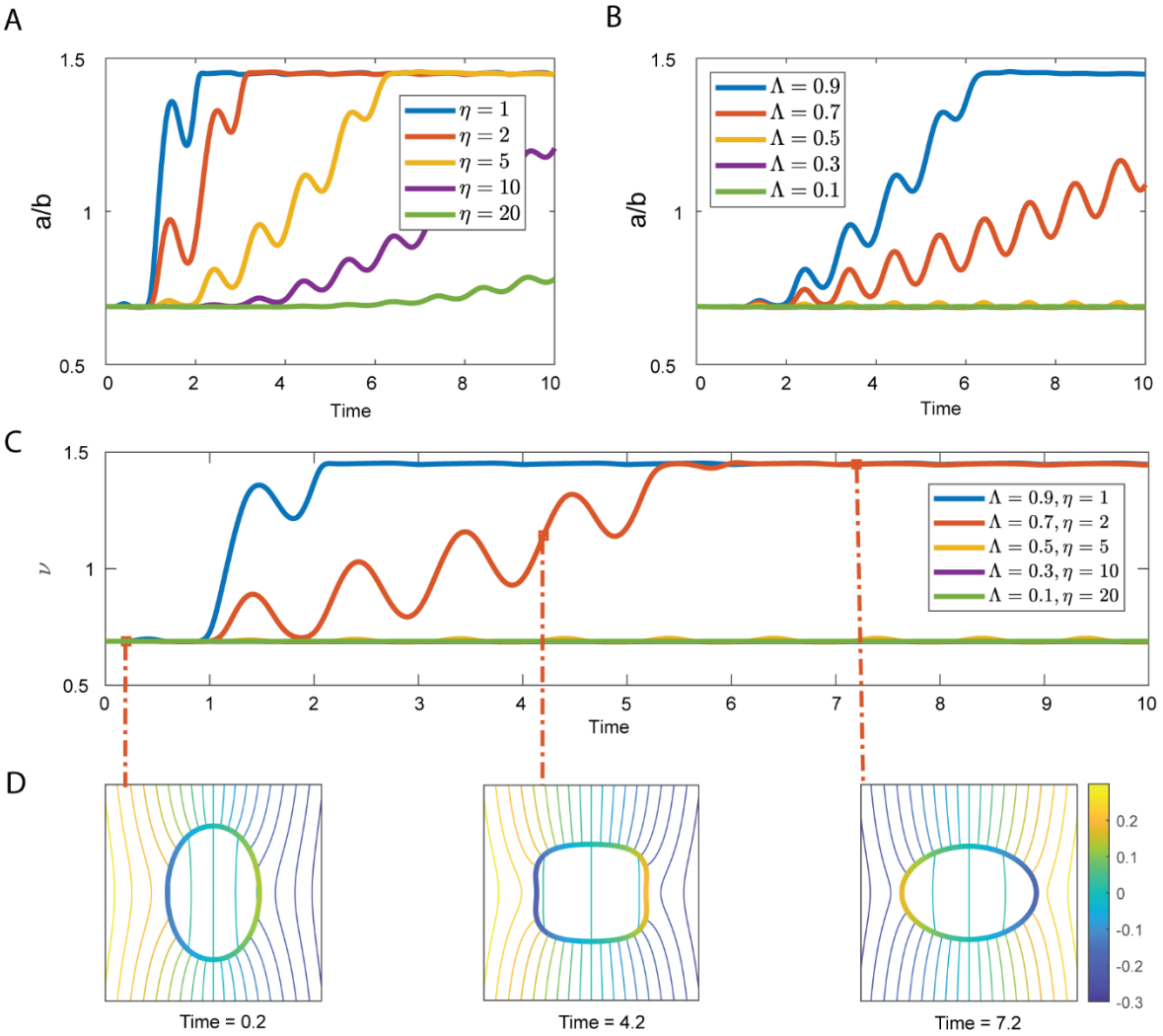

Figure 5-4 Numerical simulation of GUV prolate deformation in an AC field Coefficients (β = 10, Ω = 0.5) used for numerical simulations. (A) Electrodeformation for various viscosity contrasts η while the conductivity ratio is fixed (Λ = 0.9). We observe that the higher GUV luminal viscosity, the longer the time it takes to complete the prolate deformation. (B)

Conductivity ratio is varied while the viscosity contrast is fixed to $\eta = 5$. Prolate deformation takes longer as Λ is reduced and halts altogether below a threshold Λ. (C) Decreasing Λ and increasing η simultaneously results in a compounding effect on the prolate deformation, which is highlighted in this experiment. (D) Electric potential contour plots around the vesicle of $\Lambda = 0.7$, $\eta = 2$ at times $t = 0.2$ (flaccid GUV) $t = 4.2$ (transitionary phase) and $t = 7.2$ (prolate).

One advantage of the numerical approach presented in this section is its ability to collect a variety of quantities of interest that will be useful for further investigations. For example, we have shown in Figure 4D the contour plots of the electric potential around the vesicle that corresponds to different stages of the deformation, where it is clear that when the vesicle is being stretched during the transitioning stage, the electric field strength is almost uniformly zero inside the GUV. Transient square-like shaped deformation is a result of our simulation assuming impermeable membrane.

Structurally distinct actin networks differentially regulate GUV mechanics.

Mechanical features and responses of actin networks are governed by actin binding proteins and particularly actin crosslinkers. These crosslinkers not only assemble phenotypically distinct networks but also spatially organize actin networks allowing the cell to have variable mechanics across the cell volume. How might structurally distinct actin networks in a cell-mimicking confinement determine mechanical behavior? Here, we examined GUVs with Arp2/3-branched dendritic actin cortex (actin-cortex GUVs) or networks made with a large-angle actin crosslinker alpha-actinin (alpha-actinin-crosslink GUVs). Membrane-bound dendritic actin cortex was achieved by activation of Arp2/3 complex using membrane-associated nucleation

promotion factor (His_6-tagged VCA) on DGS NTA(Ni)-containing membrane. Encapsulating actin with His_6-tagged VCA-activated Arp2/3 complex generated uniform actin-cortex GUVs with a high efficiency (Fig. 5-5A right, 5-5C top). Absence of DGS NTA(Ni) prevents the localization of His_6-tagged VCA to the membrane consequently inhibiting the reconstitution of actin cortex (Fig. 5-5A, B). On the other hand, alpha-actinin addition led to a range of actin network morphologies, including rings, asters and random networks (Fig. 5-5C bottom). Although reconstitution of various actin networks is well established to study crosslinkers and network phenotypes (351,352,367,368), little is known about how these actin crosslinkers differentially regulate GUV deformability.

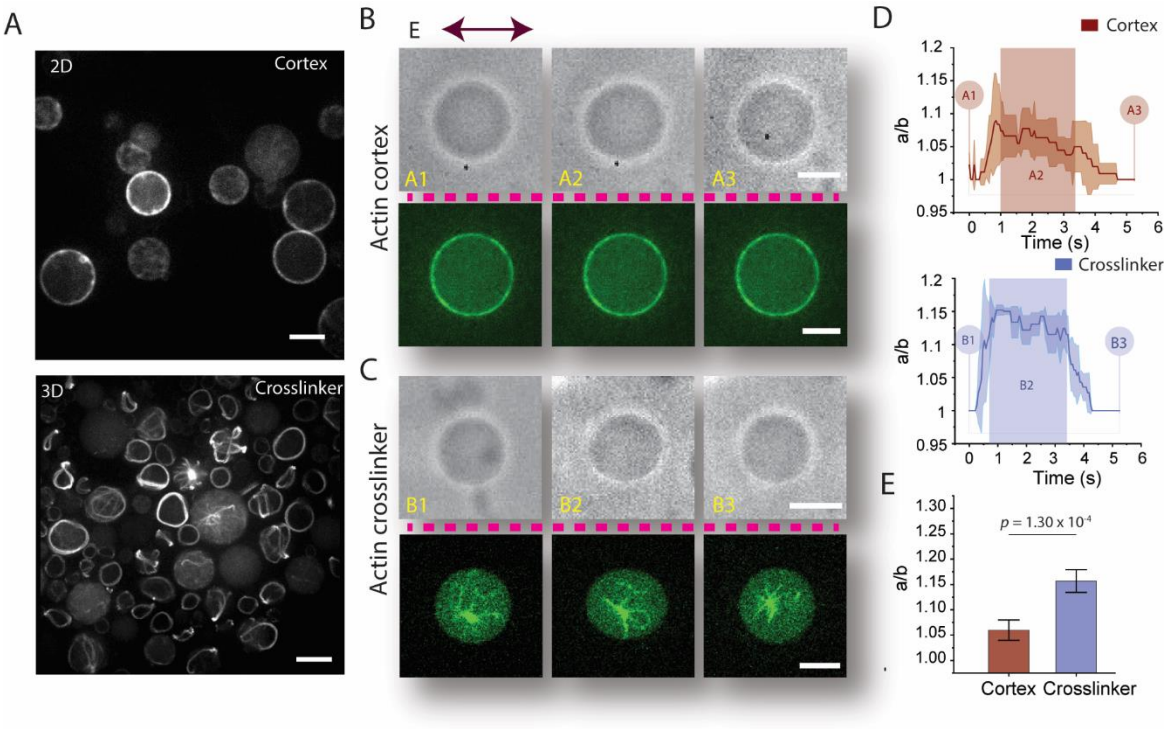

Figure 5-5 Actin networks reduce deformation induced by AC field electroperturbation (A) Comparison of actin-cortex reconstitution with and without 5% Ni-NTA DGS. (B) Plots of GUV intensity profile of across the dashed line in (A). (C) High efficiency reconstitution of actin-cortex GUVs and alpha-actinin-crosslink GUVs using the modified cDICE method. (Top)

Representative confocal image of Arp2/3 complex-assembled dendritic-actin-cortex GUVs. GUVs have a uniform actin cortex shell associated to the membrane via His_6-tag-nickel interaction. (Bottom) Representative confocal image of alpha-actinin-crosslink GUVs. Various actin network phenotypes commonly seen with actin networks with large-angle crosslinkers were observed. Both images show ATTO 488 actin to label actin networks. (D) Electroperturbation of actin-cortex GUV. (Top) Brightfield images showing shape transitions pre (A1), during (A2) and post (A3) application of AC electric field. (Bottom) Confocal images of ATTO 488 actin showing actin cortex GUVs corresponding to A1, A2, and A3. (E) Electroperturbation of alpha-actinin-crosslink GUV. (Top) Brightfield images showing shape transitions pre (B1), during (B2) and post (B3) application of AC electric field. (Bottom) Confocal images of ATTO 488 actin showing alpha-actinin-crosslink GUVs at different stages of electroperturbation. Images in D) and E) separated by dotted lines are not from the same vesicles. (F) Deformation profile of actin-cortex GUVs (Top) and alpha-actinin-crosslink GUVs (Bottom) GUVs. n = 3. Shaded rectangular box denotes approximate duration of electric field application. Shaded areas in the traces in indicate ± SD. (G) Statistical analysis of electrodeformed actin-cortex and alpha-actinin-crosslink GUVs. Data represent mean maximum deformation and error bars denote ± SE. $N_{cortex} = 12$ and $N_{crosslinker} = 11$. Scale bars, 10 μm.

We followed the same electroperturbation procedure employed in previous experiments and subjected actin cortex GUVs to an AC field. Electrodeformability of actin-cortex GUVs was greatly dampened and hardly visible to the naked eye (Fig. 5-5D). Under the same condition, GUVs with alpha-actinin-crosslinked networks were more deformed compared to actin-cortex GUVs (Fig. 5-5E). Electrodeformation was dampened to the largest extent by actin-cortex GUVs

with a max mean deformation a/b ~ 1.07 (Fig. 5-5F top), and alpha-actinin-crosslink GUVs had a max mean deformation of a/b ~ 1.15 (Fig. 5-5F bottom). Compared to the F-actin GUVs, both actin-cortex and alpha-actinin-crosslink GUVs had reduced deformability, with extreme dampening in actin-cortex GUVs (Fig. 5-5G). Looking closely at the deformation profile of actin-cortex GUVs, strangely, as shown in Figure 5D top, deformation was not sustained over the duration of AC field application, but rather GUVs started to recover immediately after reaching max deformation. Similar profile was not observed for alpha-actinin-crosslinked GUVs as they maintained deformation throughout the duration of applied AC field.

VCA is an acidic protein and its binding to the membrane may alter the dielectric property of GUV thereby its deformation under the electric field. When we included VCA and in the absence of Arp2/3 complex, we did not observe dampening of deformation (Fig 5-6A), indicating that the actin cortex itself was likely the major contributor to the observed deformation dampening. Consistent with this, leaving out NTA(Ni) lipid altogether also did not lead to a large deformation dampening (Fig 5-6A). We have presented these results comparing them to actin-cortex and F-actin GUVs (Fig 5-6B). Furthermore, we modulated the concentrations of NTA(Ni) and reduced NTA(Ni) lipids from 5% to 2.5%, we found a notable recovery of GUV deformability (Fig. 5-6C), yet with significantly enhanced deformation dampening compared to

alpha-actinin-crosslink GUVs (Fig. 5-6D). Presumably, controlling the density of actin cortex effectively tuned GUV deformability.

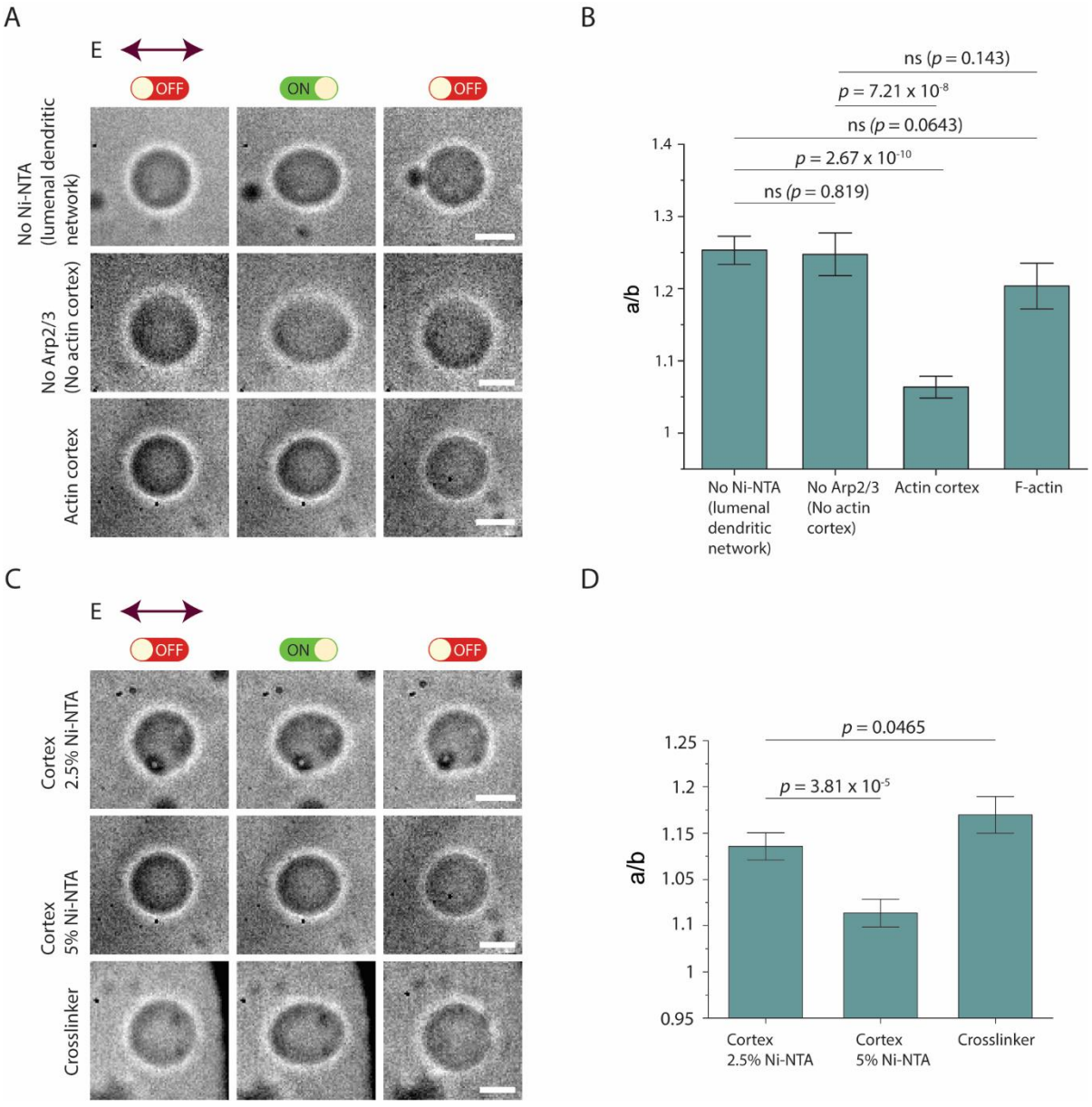

Figure 5-6 Electrodeformation of GUVs encapsulating different membrane and actin binding protein conditions (A) Brightfield images show transformation of GUVs from unperturbed (left column) to elliptically electrodeformed during application of electric field (middle column) to spherical recovery (right column). Images of GUV encapsulating 5.6 µM actin, VCA (0.5 µM), and Arp2/3 (0.5 µM) without Ni-NTA at the membrane (1st row), GUV

encapsulating actin VCA excluding Arp2/3 with 5% Ni-NTA at the membrane (2nd row), actin-cortex GUV (3rd row). (B) Maximum a/b ratio of GUVs from the three conditions indicated. (C) Electrodeformation of actin-cortex at varying Ni-NTA concentrations in lipid bilayer membrane and alpha-actinin-crosslinked GUVs. Brightfield images show transformation of GUVs from unperturbed (left column) to elliptically electrodeformed during application of electric field (middle column) to spherical recovery (right column). Images of actin-cortex GUVs reconstituted in 2.5% Ni-NTA (top), 5% Ni-NTA (middle), and alpha-actinin-crosslinked (1.77 μM) GUVs are displayed. (D) Maximum a/b ratio of GUVs from the three conditions indicated. For (B), data represent mean maximum deformation and error bars denote ± SE. $N_{2.5\%\ Ni\text{-}NTA}$ = 11, $N_{5\%\ Ni\text{-}NTA}$ = 13, $N_{crosslinker}$ = 12. For (D), data represent mean maximum deformation and error bars denote ± SE. $N_{No\ Ni\text{-}NTA}$ = 10, $N_{No\ Arp2/3}$ = 12, N_{Cortex} = 12, $N_{F\text{-}actin}$ = 13. Scale bars, 10 μm.

These results demonstrated differential mechanical properties of various isolated actin networks in a cell-like confinement. The mechanism by which actin networks achieve such mechanical variation is still open to investigation.

5.5 Discussion

In this work, we examined how the structural arrangement of lumenal contents determines electrodeformability of cell-mimicking GUVs subjected to an AC electric field. This mechanism is distinct from conditions that are known to impact the degree of electrodeformation which include conductivity contrast, osmotic contrast, lipid bilayer composition, lipid bilayer viscosity, and electric field intensity (98,191,360,361). In contrast, our results show that deformability of GUVs encapsulating actin filaments is suppressed compared to actin-free

GUVs. We demonstrated the deformation dampening of F-actin GUVs is likely manifested as increasing viscosity of the GUV lumen. Motivated by differential mechanics found in a cell, we further examined how actin cortex and crosslinked actin networks govern GUV electrodeformation. Evident from dampened deformation, our results illustrate differences in GUV deformability between different actin architectures, when they have identical total actin concentrations

The mechanism by which deformability of GUVs is dampened as a function of increasing viscosity is not apparently clear. To gain some insights, it is necessary to consider the inherent property of actin and PEG as polymer chains. Polymer chains such as actin and PEG, depending on the average polymer length and dispersity are known to entangle at random (369–371). Thus, one possible physical model that can be entertained as a plausible mechanism is from disordered polymer chain entanglement altering the strain-dependent (elastic) property of the GUV-encapsulant. Prior works have shown that there exists a relationship between polydispersity of polymer chains and their respective elasticity (372), thereby resulting in a change in permanent compressibility. Polymer chain entanglements constrain transient deformability of a viscoelastic composite such as the GUV-encapsulant composite by physically creating a barrier where entanglement networks are unable to relax/separate. Thus, it is within reason to consider the theory that an increase in viscosity in response to increasing the concentration of polymer chain is simultaneously changing the elastic property of actin encapsulating GUVs. In the future, other physical models and theories can be investigated as potential explanations for the dampening of deformation as a function of increasing viscosity of the GUV lumen. We acknowledge that cell cytoplasm is known to be highly viscous due to the high protein contents that is not just attributed by actin filaments. While our data suggests

viscosity could play a role, we believe the architecture (i.e., how they are organized and where) of the actin networks has a more dominant role here.

As revealed by our findings, actin-cortex GUVs have greater deformation resistance compared to GUVs with alpha-actinin-crosslinked networks. Prior findings by Wagner *et al.* show that actin crosslinkers increase viscosity of actin in bulk solutions (364). However, the structure and spatial scale of actin networks formed in bulk solutions are diametrically different from those assembled in a cell-like confinement. Thus, it would be premature to attribute our finding that actin crosslinkers differentially regulate GUV electrodeformability to simply viscosity difference. During electrodeformation, GUVs undergo two distinct deformation regimes namely entropic and elastic regimes (355). The extent of the deformation in the entropic regime is dependent on the degree of thermal undulations in the bilayer which varies depending on the lipid composition and osmotic contrast, whereas the elastic regime is dictated by field intensity and bilayer stretchability at the molecular level. These deformation regimes may potentially be altered as a result of the material property of the lumen and its interaction with the lipid bilayer membrane. Thus, it is important to consider mechanisms of how different actin networks may affect these deformation regimes beyond changes in lumenal viscosity. In this context, it will be interesting to study the effect of actin network on deswelled GUVs and how actin networks impact deswelled GUVs' deformation.

It is well established that the actin cortex regulates membrane rigidity (373,374). When thin actin-cortex shells were reconstituted in GUVs and subjected to hydrodynamic tube pulling, it was shown that the membrane tube length was reduced for thin actin shell GUVs (375). Considering this prior finding, it is possible that the mechanism of electrodeformability suppression by actin cortex is due to changes in membrane rigidity that restricts membrane

undulation in the entropic regime of deformation, and thereby restricting lipid mobility, consequently reducing bilayer stretching, in the elastic regime of electrodeformation. More likely though is that the elasticity of the cortex may contribute to the increased deformability resistance of actin-cortex GUVs. For alpha-actinin-crosslink GUVs, a different mechanism may be plausible to account for their suppressed electrodeformability. When F-actin GUVs are subject to an electric field, due to the scale of individual filaments with respect to GUV size and field pressure, actin filaments are unable to individually resist deformation, akin to sand grains in quicksand, and unable to undergo individual strain. However alpha-actinin assembles complex actin scaffolds that can reinforce the GUV, like a truss system, to resist field forces. Further investigation could possibly shed more light on the relationship between crosslink/bundle rigidity and electrodeformability and a more systematic study to titrate concentrations of crosslinkers will be informative.

For the numerical simulation of the electrodeformation of GUVs, the leaky-dielectric model is used, which characterizes some key physical and mechanical properties of GUVs, including conductivity contrast, membrane rigidity, and lumenal viscosity. Our numerical simulations provide additional supporting evidence, independent of experiments, that GUVs of increased lumenal viscosity experience greater deformation resistance. An important advantage of numerical simulation is its ability to collect various quantities of interest at ease, such as electric potential and velocity fields, offering more detailed characterizations of GUV electrodeformation. However, there are limitations to the current mathematical model. Firstly, due to its simplifying assumptions on the membrane structure, this model is incapable of capturing phenomena such as electropermeabilization and electroporation that occur under a strong electric field. Thus, our model restricts the membrane to an inextensible and intact

boundary, which also explains why vesicles appear non-spherical before application of electric field. Secondly, the current model does not account for the cytoskeleton structures in GUVs, which will be important for further investigating the effect of different actin networks as integral structural components on the electrodeformability of GUVs. We think that this also explains the mismatch between our experimental and simulated results. Limitations to simulate change in the elastic behavior of entangled actin could possibly be why we fail to observe deformation dampening at steady state. To resolve these limitations in the future, more sophisticated mathematical models need to be developed.

There are many fascinating mechanobiological inquiries that can be pursued using cytoskeletal GUVs. The cell is a very dynamic and structurally and functionally complex system with many proteins involved in a single function. The GUV furnishes a cell-like confinement system that is suitable for systematic construction of complex cellular functions module by module. Using our findings as a steppingstone, we anticipate future interest in examining the role of various other types of actin networks, and co-assembled networks of actin, intermediate filaments, and microtubules, in determining mechanophenotypes. The emergent mechanics of cytoskeleton is an underexplored area of cytoskeleton and membrane research. Our work provides a starting point to examine a myriad of other actin crosslinkers and their mechanical contribution to cell mechanical properties. Such efforts will help uncover deep insights into cell mechanics from the bottom up.

5.6 Acknowledgments

We thank Yashar Bashirzadeh for helpful discussion. We thank Professor Mark Burns and Anna Nelson for kindly letting us use their conductivity meter. We thank UM Battery Lab and Eleni

Temeche for assisting us with viscosity measurements. The work is supported by the National Science Foundation (CBET-1844132). N.H.W. was supported by NIH's Microfluidics in the Biomedical Sciences Training Program (NIH NIBIB T32 EB005582). S.V. acknowledges support from National Science Foundation (DMS-2012424). A.P.L. acknowledges support from National Institutes of Health (R01 EB030031-01) and National Science Foundation (EF1935265 and MCB220136).

Chapter 6 Rearrangement of GUV-Confined Actin Networks in Response to Micropipette Aspiration

6.1 Abstract

Studies have shown that actin networks to be force sensing, force generating and endowing the mechanical property of cells. Actin networks are capable of these specialized tasks due to their ability to rearrange and assemble into diverse networks via numerous actin binding proteins. However, how different actin networks reorganize under applied forces is not entirely understood. Recently, bottom-up reconstitution has enabled studies where dynamic and phenotypical characteristics of various actin networks can be recreated in an isolated cell-like environment. Here, by creating a giant unilamellar vesicle (GUV)-based cell model encapsulating actin networks, we aim to understand how actin networks rearrange in response to stresses in confined spaces. We reconstitute actin cortex and actin bundles separately and use micropipette aspiration to mechanically perturb and induce stress. Interestingly, we find that, when aspirated, protrusive actin bundles that are otherwise randomly oriented in the GUV lumen collapse and align along the axis of pipette. Furthermore, when uniform cortex-GUVs are aspirated, bleb-like cortex-free membrane is aspirated in the micropipette. These results reveal diverse responses in the rearrangement of actin networks when subjected to physical forces.

6.2 Introduction

The mechanical environment that cells experience while navigating their environment is constantly changing, and thus demanding cells to adapt by reassembling the cytoskeleton. There is compelling evidence that actin reorganizes network architecture in response to loading. Whether stretching, compressing or locally indenting, actin self-assembles in response to the mechanical stimuli. For instance, locally indenting the a cell using microneedle probes revealed quick response in the dynamics of actin cortex to reinforce the cell membrane (376). Others have also investigated responses of actin networks by probing actin binding protein localization. Under micropipette aspiration-induced loading, it was discovered that myosin and alpha-actinin localization were sensitive to area dilation induced by aspiration, while filamin had a pronounced response to high shear regions (377). Similarly, using numerous cell types, many have characterized the dynamics of actin networks in response to physical forces. However, although we can determine collective response of actin dynamics in response to mechanical cues in cells, it remains unclear how specific actin architectures respond differentially to contribute to the collective dynamics of the whole. Investigating differential dynamics of actin architectures assembled by various actin binding proteins is vital for dissecting the mechanical property of the cell for deeper understanding.

As mentioned in previous chapters, the challenge of modularly investigating cellular processes is the intrinsic complexity of the whole cell. Prior studies characterizing mechanical properties of actin have tackled this challenge by leveraging bottom-up reconstitution using GUV-based minimal cell models. For example, studies have investigated GUV shape change due to internal forces exerted by actin networks (52,75,309). Furthermore, many perturbation methods used for mechanophenotyping biological samples have been implemented to

mechanically perturb GUV-based minimal cell models (378). Using some of these perturbation methods, a limited number of studies have measured physical quantities such as compressibility modulus (105) and viscoelastic response (106), and deformability (81) of actin network-encapsulating GUVs. However, to date, how isolated actin architectures in a cell-like confinement dynamically respond to physical forces remain to be explored.

In this work, we aim to investigate the reorganization of actin networks assembled by different actin binding proteins and if they exhibit differential dynamic responses to loading. We reconstitute fascin-bundled networks and Arp2/3-branched dendritic cortex in GUVs. Using micropipettes, we induce a negative pressure to aspirate on single GUVs. In F-actin GUVs, we observed that actin filaments resist deformation and withstand forced access into the micropipette. Interestingly, we find that fascin-bundled networks rearrange and align parallel to the flow axis of the micropipette. However, addition of Arp2/3 complex inhibits bundle alignment, subsequently preventing the network from entering the micropipette. Finally, we reconstituted membrane-bound Arp2/3 assembled cortex and induced loading via aspiration. We discovered that dendritic networks preferentially reorganize along the GUV membrane, where low curvature regions exhibit pronounced dendritic network localization, while protrusion tips are devoid of cortical network and bleb-like.

6.3 Material and Methods

Reagents

Purified actin and Arp2/3 complex was purchased (Cytoskeleton Inc., USA). ATTO 488 actin was purchased from Hypermol (Germany). General actin buffer (G-buffer) and actin polymerization buffer (F-buffer) was prepared as directed by Cytoskeleton Inc. Fascin was

purified in the lab as detailed in (80). We also purified hexa-histidine-VCA (His_6-tag VCA). 10 mg/ml stock concentration of actin was diluted to 1 mg/ml and further serially diluted as needed to working concentrations using G-buffer + 0.5 mM DTT + 0.2 mM ATP. 1,2-dioleoyl-sn-glycero-3-phosphocholine (DOPC), 1,2-dioleoyl-sn-glycero-3-[(N-(5-amino-1-carboxypentyl)iminodiacetic acid)succinyl] (nickel salt) (DGS-NTA(Ni)), and cholesterol were purchased from Avanti Polar Lipids (USA). Optiprep, a density gradient medium, was purchased from Sigma Aldrich (USA).

Micropipette Aspiration

The micropipette aspiration setup consists of a pulled and cut micropipette tip mounted on a micropipette holder, pipette micromanipulator, a liquid reservoir, a filling syringe, and a pressure transducer. To prepare micropipettes, standard glass capillaries (WPI, USA) are pulled using a Sutter P-87 pipette puller (Sutter Instruments Co., USA). After pulling pipette tip, pipettes were manually cut to an acceptable size in the range of 2-6 μm using a heated glass rod. Glass rods are heated using a Bunsen burner and brought to contact with the pulled capillary at the tip. Instantly after contact, glass rod is pressed through the pipette in swift motion which should result in a clean pipette cut. This is principally similar to cutting pipettes using microforges. Next, pipettes are submerged in a 1% BSA solution to prevent GUV adhesion. Integration of the micropipette aspiration setup, shown in Figure 6-1A, is as follows. 1. Pipettes are mounted and secured into a pipette holder. 2. A three way valve connects a fluidic line between the filling syringe, the micropipette, and the fluid reservoir. 3. Reservoir is pneumatically connected to a high-speed pressure clamp (HSPC) (ALA Scientific Instruments, USA). Once this configuration is accomplished, the filling syringe, containing a solution

osmotically similar to the GUV condition, will be used to fill the micropipette line and reservoir. Elimination of all air bubble is vital for performing micropipette aspiration experiments. Once the sample is ready for imaging and aspiration, a slight positive pressure, not a 0 pressure, should be maintained either by keeping the reservoir at a slightly higher altitude, or applying a minimal positive pressure using the pressure transducer. This shall be maintained until the GUV of interest is located under the microscope. Finally, using a micromanipulator, the pipette will be brought to close proximity with the GUV plane. This should result in a slight pushing of the GUV from the positive pressure coming from the pipette tip. Once GUV is located, pressure transducer is used to apply appropriate negative pressure to induce aspiration onto the GUV.

Actin encapsulation inside GUVs

Actin encapsulation inside GUVs was achieved using the cDICE technique as described in (379). Oil and lipid composition, actin solution composition for bundle networks, branched bundles and actin cortex, are all described in detail in Chapter 4 of this thesis work.

Imaging

Micropipette aspiration of actin GUVs was captured using Olympus IX-81 inverted microscope equipped with a spinning disk confocal (Yokogawa CSU-X1), OBIS LS/LX lasers (Coherent, Saxonburg, PA, USA), and an iXON3 EMCCD camera (Andor Technology, South Windsor, CT, USA). Metamorph was used to control the above components and acquire images. 40X/1.3 NA objective was used for imaging samples. Fluorescence images of actin networks were acquired to visualize networks by exciting ATTO 488 actin at 200 ms exposure, while low light brightfield images were simultaneously taken to capture and track the micropipette tip as it

was operated using a micromanipulator. To record actin dynamics in response to changes in aspiration pressure, timelapse images were taken every 300 ms.

6.4 Results

Actin filaments inside GUVs display resistance to aspiration

To validate our micropipette aspiration setup (Fig. 6-1A), empty 70% DOPC/30% cholesterol GUVs with a trace amount of fluorescent lipid were aspirated at incremental pressure points (Fig. 6-1B). During preparation for micropipette aspiration, after filling all fluidic tunings with glucose solution, to assure air bubbles are not drawn into the tip in moments when the micropipette tip is not submerged into the sample solution containing GUVs, we made sure that there is a net positive pressure at the tip of the micropipette by slightly raising the reservoir with respect to the tip (Fig. 6-1A). Once the micropipette is positioned, using the micromanipulator, in the correct frame and plane where GUVs are, we use the motorized microscope stage to locate a GUV of interest with respect to the micropipette tip, which is in a fixed frame. Once aspirated, GUVs instantly seal the pipette and protrude. At each pressure increment, we observed aspirated protrusions elongating (Fig. 6-1B). We can also see that there is not a visible decrease in the GUV volume outside of the pipette despite increase in elongation of protrusion. This is consistent to prior observations (380) and is attributed to area dilation due to the elastic stretching of GUV lipid bilayer. Following validation of the micropipette aspiration setup, we investigated mechanical response of GUVs encapsulating actin filaments.

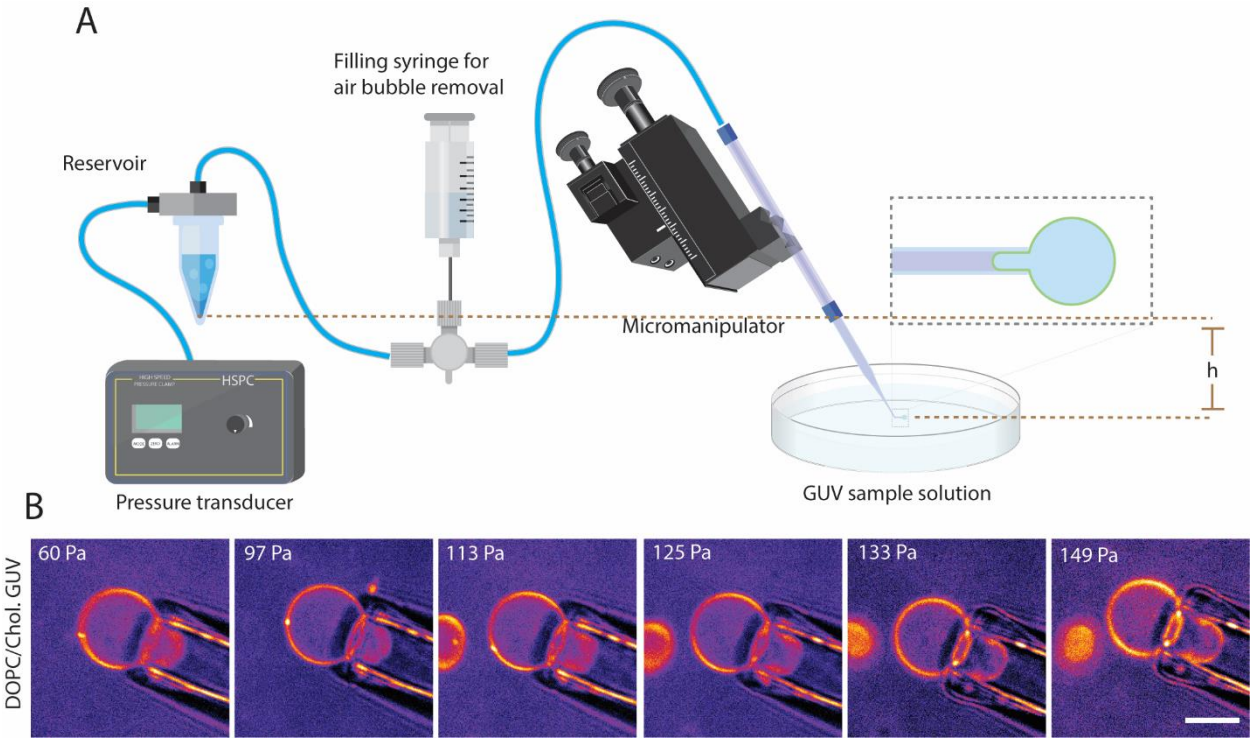

Figure 6-1 Validating micropipette aspiration setup

(A) Schematic of micropipette aspiration setup. (B) Validating micropipette aspiration using empty GUVs. Representative images, acquired using confocal microscope, show response of GUVs to incremental changes to aspiration pressure, left to right. Fluorescence images labeled membrane. Brief exposure to white light allowed for the simultaneous visualization of micropipette. Scale bar, 10 µm.

As the major determinants of cellular mechanics, we became interested in how actin filaments encapsulated inside GUVs respond to loads using micropipette aspiration. We reconstituted actin filaments by polymerizing 5.3 µM globular actin using F-buffer. Similar to empty GUVs, actin filaments were encapsulated in 70%/30% DOPC/cholesterol GUVs. Unaspirated and simply dispersed in a solution, fluorescence images of F-actin GUVs display uniform distribution of filaments throughout the GUV lumen. Interestingly, we saw that this

symmetry/uniformity breaks when actin-GUVs are aspirated (Fig. 6-2). As shown, the actin channel (Fig. 6-2A mid), actin density is lower throughout the protrusion compared to the lumen outside of the pipette. Line intensity profile (Fig 6-2A, right, Fig. 6-2B) of aspirated actin-GUVs show a decay in filamentous actin with the lowest recorded intensity at the very end of the protrusion. Actin filaments are flexible polymers with lengths ranging from submicron to few microns of length. Our findings, suggest that polymerized filaments at 5.3 µM exhibit a collective behavior, possibly through entanglement, of resistance to remain outside of pipette constriction.

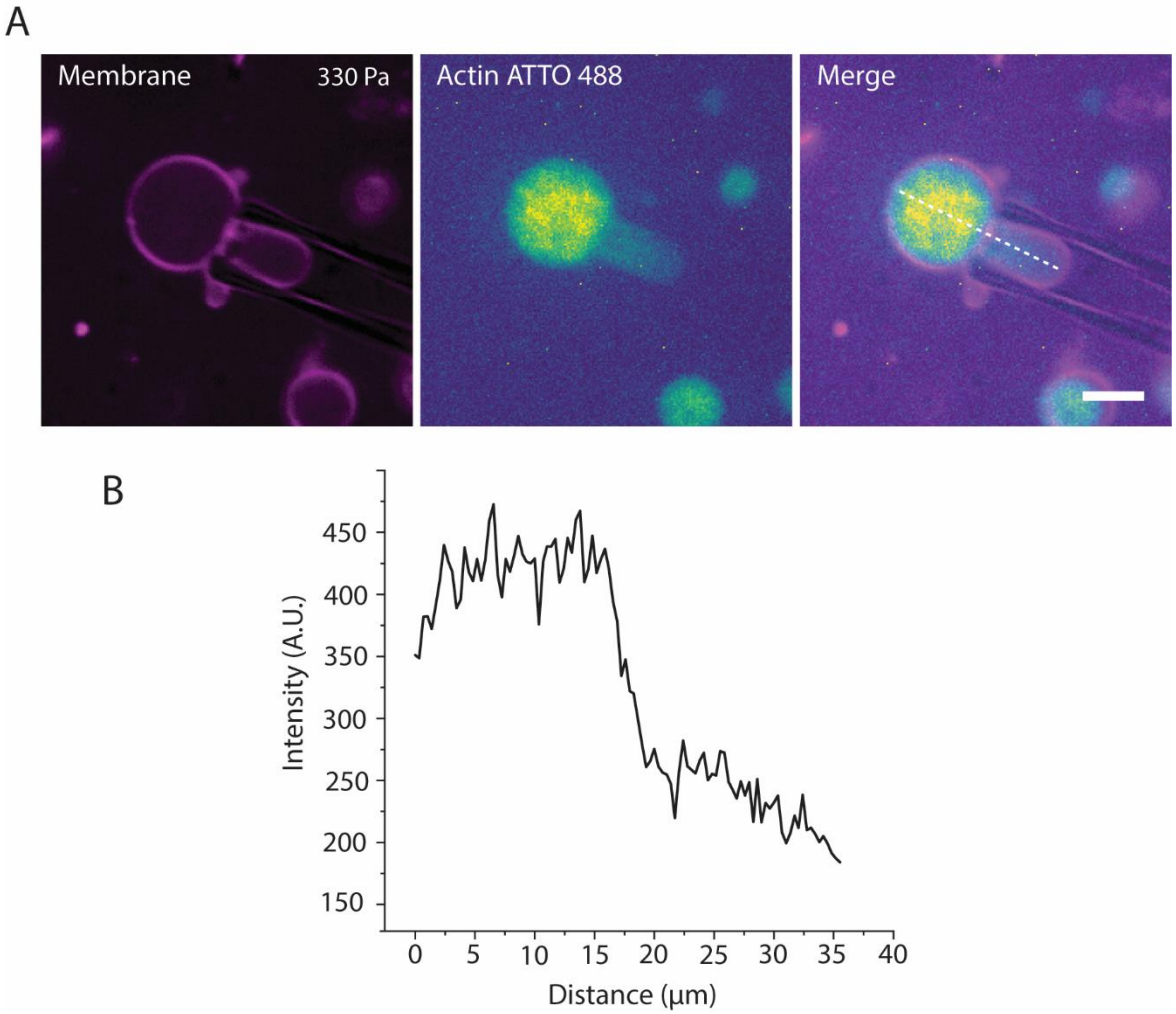

Figure 6-2 Micropipette aspiration of actin filament GUVs

(A) Representative fluorescence confocal images of GUV membrane, actin, and merged channels (left to right). Actin channel (middle) shows reduced actin intensity in the portion of GUV protruded into the micropipette (B) Line scan shows actin intensity profile along the line indicated in (A, right). Scale bar, 10 μm.

Fascin-bundled actin aligns along the axis of the flow in response to aspiration

Following our observation that actin filaments resist entering into micropipette upon aspiration, we continued to investigate how other actin architectures reorganize in response to aspiration-induced loading. First, we encapsulated fascin-bundled actin networks inside GUVs as illustrated in the schematic in Figure 3A. We reconstituted actin filaments by polymerizing 5.3 μM actin using F-buffer followed by adding fascin at 1:5 ratio to actin to initiate bundling. Encapsulation using the modified cDICE technique was done promptly before maturation of the bundled network. As have been confirmed before, fascin, at 1:5 ratio to actin, assembles stiff protrusive bundle in random orientation. These protrusive bundles, to our knowledge, do not reorient with respect to the GUV via diffusion, rather maintain a fixed architecture. Upon micropipette aspiration of a GUV initially at a distance from the pipette tip, we observed that GUV as a whole reoriented in a manner where the dominant bundle aligned with the axis of flow as it moved near the tip of the pipette (Fig. 3B). Here, we define dominant bundle as the bundle that deforms the GUV to its longest/major axis. Colors used in Figure 3A indicate time points every 200 ms. Hydrodynamically, this alignment is energetically favorable to minimize drag against fluidic current in a manner where the smallest surface area is orthogonal to the current.

One can imagine ideal shapes of water transport systems such as boats and ships and how they do not sail on their side.

Our most interesting finding is how fascin-bundled actin architecture dynamically reorganizes once it is trapped in the micropipette (Fig. 6-3C top). Once aspiration began, at the first instance of pressure increment, fascin bundled networks almost instantly reorganized where bundle ends inside the aspiration pipette converged to a single point (Fig. 6-3C) and the opposite ends of bundles that were in the unaspirated region of the GUV diverged in random directions. We call this the alignment initiation stage. Such arrangement is reminiscent of a matcha whisker. Fascin GUVs equilibrate in this arrangement exhibiting resistance for further insertion into the micropipette. Further increasing aspiration pressure, however, begins to align the fascin bundles along the axis of aspiration. At the final aspiration pressure of 533 Pa, initially randomly reoriented bundles, were fully aligned into one thick bundle fully constricted by the walls of the capillary. Our initial mechanistic hypothesis to this observation was that these bundles were not crosslinked to one another, and the fluidity of the membrane may facilitate lubrication for bundles to slide and rearrange.

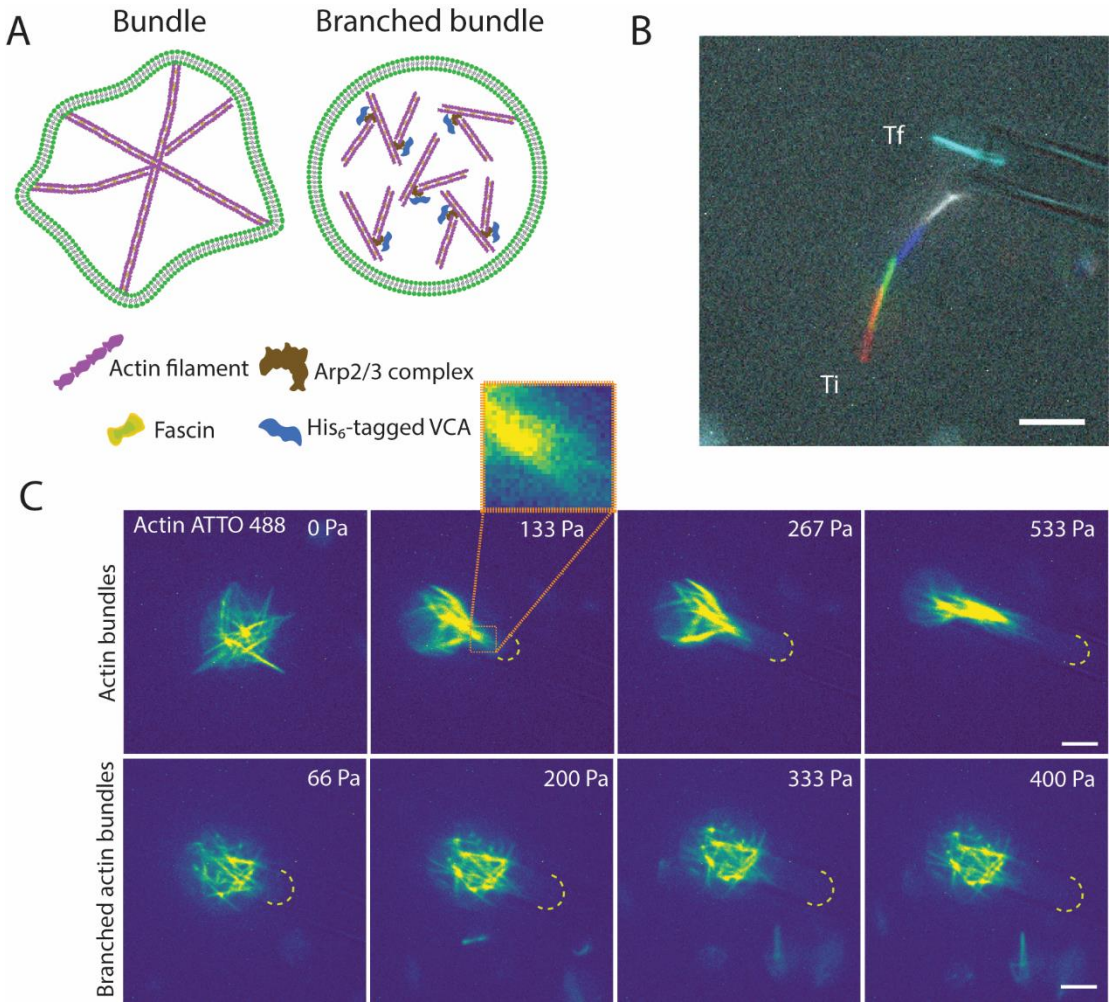

Figure 6-3 Micropipette aspiration of fascin-bundled actin networks

(A) Schematic showing assembly of bundled actin networks via fascin and branched bundled networks via fascin and Arp2/3 complex. (B) Reorientation of GUV encapsulated (membrane channel not shown) in response to aspiration-induced flow. Fluorescence timelapse confocal images of actin. Pseudo colors indicate time points at every 200 ms increment stating from initial time (Ti) to final time (Tf). (C) Dynamic responses of actin networks at different aspiration pressures. Randomly oriented fascin-bundled networks (top left) align along the axis of flow into thick bundles to access micropipette. Images show alignment dynamics in response to increasing aspiration pressures. (Bottom) Dynamic response of branched bundled actin networks to

aspiration. Despite an increase in pressure (left to right), there is no observed alignment of bundles. Scale bar, 10 μm.

To support this hypothesis, we performed an experiment where we encapsulated bundles that are branched (i.e., the bundles are physically linked to one another). We achieved this architecture by co-encapsulating fascin with Arp2/3 complex along with its activator VCA. From our prior work, we have demonstrated that co-encapsulation of Arp2/3 with fascin suppresses protrusive bundles via branching and shortening facsin bundles (80). When aspirated, branched bundled actin GUVs (Fig. 6-3C bottom) exhibited an entirely different response where there was no observed alignment of bundles. These architectures continued to resist inserting into the micropipette until the aspiration exceeded area dilation threshold resulting in bursting of GUV. This suggests that physical crosslinking between bundles dictates reorganization in response to aspiration load.

Preferential cortex reorganization along GUV membrane in response to aspiration

Next, we wanted to investigate how actin cortex, a membrane adjacent actin network, which is essential in driving motility and shape change, reorganize in response to micropipette aspiration. Unlike lumenal networks, such networks like the cortex are associated with the membrane through linking cofactors that commonly have membrane binding domains in cells. We reconstituted actin cortex by encapsulating membrane-bound dendritic networks as shown previously (81), in GUVs containing DOPC/cholesterol/Ni-NTA-DGS at 70%/25%/5% (Figure 4A). As reported by many and our own prior work, the shell of dendritic network assembles a uniform cortex. However, upon aspiration, we saw that an initially uniform cortex rearranged

preferentially along the GUV membrane. Towards the end of the protrusion at the tip, GUV became bleb-like and cortex-free (Fig 6-4B). On the contrary, actin cortex was more pronounced along the walls of the micropipette. Furthermore, while this needs to be supported with quantitative analysis and additional experiments in the future, cortex GUVs sustained larger pressure without bursting compared to fascin-bundled network GUVs. Our findings of preferential cortex reorganization suggests that, while membrane and membrane-associated actin networks work in tandem to assist cell function, their dynamic responses to loads can be mutually independent.

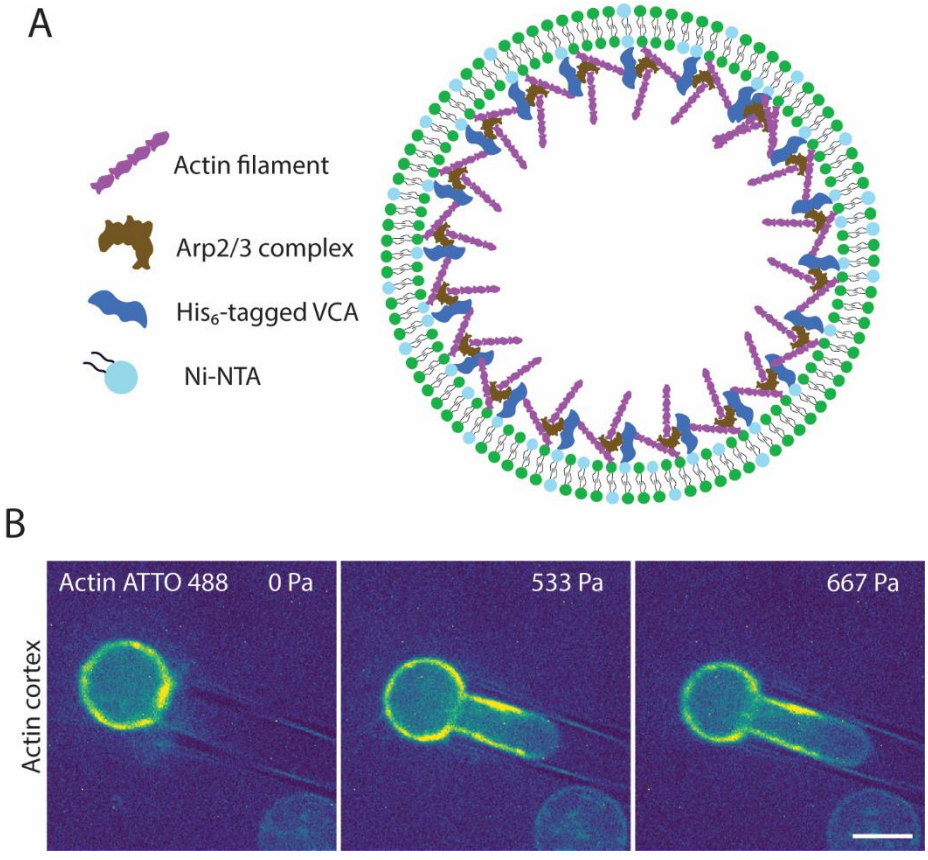

Figure 6-4 Micropipette aspiration of actin cortex GUVs

(A) Schematic illustrating assembly of actin cortex inside GUVs. (B) Representative fluorescence confocal images of actin cortex GUVs subjected to micropipette aspiration. Images,

left to right, indicate cortex response to increasing pressures. Initially uniform cortex (left) reorganizes when aspirated. While the actin cortex is pronounced in the low curvature region along the walls of the pipette, the protrusion tip is void of or display minimal cortex remnants. Scale bar, 10 μm.

6.5 Discussion

Although further experiments are required to identify the mechanism by which actin filaments withstand aspiration, there are logical mechanisms we believe may contribute to this phenomenon. Probable cause for this dynamic response of actin filaments to micropipette aspiration can be attributed to synergetic effect of stress stiffening and entanglement. Prior studies have claimed that actin filaments are intertwined long chain polymer strands and is also tightly packed thus having minimal bending fluctuations (381). Translating this to our observation, first, entanglement of actin filaments, which enhances its mechanical property, could be creating resistance of filamentous actin to micropipette-induced deformation. Second, It is understood that filamentous actin solution is a non-Newtonian fluid and has been known to show stress stiffening and relaxation (370). Thus, it is possible that, due to elevated lumenal stress in response to aspiration, entangled actin filaments stiffen and subsequently become unyielding to protrude into the constricted micropipette region. These likely mechanisms will be investigated in the future as a continuation of this work.

So how do protrusive bundles that elevate membrane tension seamlessly reorient into alignment to a larger bundle? For protrusive bundles to align, many things in the system must go right. Fascin bundles are not crosslinked to one another. This, we believe, is a prerequisite for bundles to reorient independent of one another. Second, the contact between highly protrusive stiff

bundles and the tensed boundary must be highly lubricated to facilitate rearrangement without membrane or bundle buckling when aspiration forces are applied. In principle, this is a possibility in our GUV system because lipid bilayer membranes are 2-dimensional fluids, in which the sliding of protrusive ends of bundles along the membrane is possible without necessarily wrinkling or folding the membrane as a result of nominal friction between membrane and bundles. Our hypothesis is that a lack of crosslinking between bundles and fluidity of membrane are operating jointly to assist the alignment of randomly oriented protrusive bundles into one single thick bundle. We have data shown in Figure 6-3C bottom to demonstrate how crosslinked bundles cannot easily reorient or align. Further investigation into both of these mechanisms is needed.

The preferential reorganization actin cortex in response to aspiration can be attributed to a number of mechanisms. First, stress distribution when aspirating on a viscoelastic object is locally variable. This can easily be confirmed from the umbrella/mushroom shape cells assume when aspirated using micropipettes. However, prior study modeling GUV aspiration using finite element analysis has demonstrated that this remains to be true in GUVs as well (382) This work has also shown that, elevated local stresses are experienced at the tip of the protrusion of the GUV. Given, it is possible dendritic networks are breaking up in response to elevated stresses at the tip of protrusion. Alternatively, we also know that an increase in membrane tension leads to phase separation in ternary lipid compositions which is what we have in DOPC/cholesterol/Ni-NTA composition. Thus, it remains a possibility where Ni-NTA localizes in reduced stress regions away from tip of the protrusion, thus resulting in the reorganization of cortex. We can understand this as actin reorganization in response to micropipette aspiration induced phase separation. It is worth noticing that a study has shown actin cortex assembly also can induce

phase separation in GUVs (311). Our future work will explore these possibilities to identify how precisely actin cortex preferentially organize when subject to micropipette aspiration.

In summary, the micropipette aspiration setup is a great tool to mechanically characterize biological samples such as GUV-based minimal cell models. It is also true that it mimics physical constrictions cells may experience in their native environment. Thus, making it an ideal tool to study how actin network reorganize differentially under load. Our findings indicate the dynamics of actin networks under load is variable as a function of architecture. Polymeric entanglement due to the nature of actin filaments and stress stiffening may endow a network resistance to deformation. Similarly, branching by actin binding proteins also reinforce structural integrity by withstanding loads. Lone protrusive bundles, similar to those assembled by fascin, on the other hand, rearrange to adapt to the new physical environment. Although these finding are insightful into understanding actin mechanics, it is also important to acknowledge that these are simplified systems with no actin turnover or reassembly machineries and thus do not entirely capture cellular events.

Chapter 7 Conclusion and Future Directions

7.1 Summary

The very fabric of everything physical can be described through its mechanics. In theory, from the smallest of the elementary particles to everything living and non-living on earth, to all else in the universe, the physics of their motion describes, quite literally, everything there is to know about a system of matter we can scientifically prove of its existence. Someway, somehow, the mechanics of atoms and molecules of countless arrangements, how they diffuse and interact at the scale of femto- to picoliter volumetric boundary, produced the emergence of what we now describe as life: the cell. Mimicking its substrate ingredients, the cell, in the classical sense where things are not sub-atomically small and do not behave in strange ways, is also very mechanical. Through its very mechanical interior parts, the cell moves, morphs, and subsequently interacts and exerts forces to the exterior. Here is where my interest in understanding cellular mechanics comes in, and throughout my thesis work, I have explored how the mechanics of a cell is endowed.

For a long while now, people have understood there is a cellular module, the cytoskeleton, especially delegated to force exertion and sensing, and that it is integral to some of the most important cellular functions. Actin, in particular, is among the most studied cytoskeletal proteins, that either principally orchestrates or facilitates cellular processes such as directed migration, division, and adhesion. The actin cytoskeleton is a self-assembling dynamic system able to construct structural architectures with spatial specificity. Numerous actin binding

proteins, globular actin binding and filament binding, regulate actin dynamics in different ways. Maintenance of actin monomers, nucleation of actin filaments, growth speed of filaments, assembly of filaments to networks, disassembly of networks and filaments through severing, and filament contraction through motors are all regulated by actin binding proteins. Regulation of actin through various actin binding proteins and pliability of networks enable actin to execute cellular processes through different mechanisms. Polarity of architectures such as contractile networks and protrusive motive force generators at the rear and the front of the cell, respectively, enables directed migration of a cell. Morphological changes leading to rounding up of the cell pre-mitosis, formation of contractile ring during mitosis, and morphological recovery post cytokinesis is regulated by assembly and disassembly of actin filaments and networks. Furthermore, cell adhesion, a process critical for cell-cell communication, differentiation and migration, is also facilitated by assembly of actin stress fibers. It is safe to say, a deeper understanding of how actin drives and facilitates cellular functions is critical for understanding the cell as a whole.

Over the past few years, I have been asking and attempting to answer questions that I hope will narrow down the gap in our understanding of actin mechanics. In mechanophenotyping actin networks, my findings demonstrated how actin respond in non-native physical environments, how actin binding protein interact to assemble networks and how actin networks differentially regulate the elastic modulus of a cell. I started out by studying cell mechanics in cells to investigate how actin networks respond to simulated microgravity. Appreciating how complex the cell is to modularly characterize actin networks as a function of respective actin binding proteins, I shifted gears to leverage GUV-based minimal cell models. Here, I was able to reconstitute actin networks inside cell-sized confinements with a fine control over elements of

actin network assembly. Using bottom-up minimal cell models, I discovered that actin binding proteins compete by suppressing dominant network features of one another and actin networks differentially regulate deformability and reorganize in response to external loads.

7.2 Chapter Summary

7.2.1 Cells in simulated microgravity

It was only in the late 60s, that cells in a human body experienced extended period of zero gravity for the very first time. This is such a foreign environment that our cells do not have genetic memory or molecular strategy to adapt. Consequently, astronauts have endured bodily changes and one of these is severe bone loss, especially experienced by those living at the International Space Station (ISS) for an extended period of time. In those candidates, studies have shown 50-60% elevation in bone turnover markers resulting in bone decay (258). As one of the sensory elements of forces, we asked, how does actin respond to the lack of forces?

The challenge in studying effects of microgravity on biological samples on the ground is gravity. Thus, it is imperative to counter gravity in order to attain microgravity. Diamagnetic levitation, acoustic levitation and clinostats are some of the ways to induce the effects of microgravity here on earth. Using a custom home-built device called random positioning machine (RPM), we simulated time-averaged microgravity of 0.0000123g. RPM has two rotational axis able to rotate in random directions at a maximum angular velocity of 42^{o}/s. Compared to other lab-friendly microgravity simulation devices such as 2D clinostat and 3D clinostat, RPM exerts minimal shearing effects from reduced speed of rotational motion. Our aim in this work is to understand how microgravity affects the mechanics of bone precursor cells. We subjected human fetal osteoblast cells (hFOBs), adherent in nature, to simulated microgravity for a period of 3 hours and 6 hours. Quantification of morphological changes revealed that simulated

microgravity had a rounding-up effect on hFOBs highly spread cells became more rounded with decreased surface area and increased circularity. Evidently, immunostained samples showed that actin appeared highly disorganized compared to cells in static 1g condition. Further probing phalloidin-stabilized actin filaments using flow cytometry indicated that actin is highly disassembled. Finally, we wanted to see the outcome of these changes in the mechanical property of the cell. Using a microfluidic micropipette aspiration device, we measured a significant reduction in the stiffness of hFOB cells subjected to simulated microgravity. Although these results solely cannot determine why and how bone turnover are elevated during space exploration, we believe that our findings render insights on how these mechanophenotypical changes play a role in regulating bone morphological cascades.

7.2.2 Network assembly competition

In Chapter 4, I investigated how fascin and Arp2/3 complex compete and cooperate to design an actin-based architecture in a minimal cell-mimic system. Here, I reverse engineered a minimal cell by reconstituting actin networks via encapsulating purified actin and actin binding proteins inside a giant unilamellar vesicle (GUV). It is known that both Arp2/3 complex and fascin are vital for directed migration of the cell by assembly of force generating actin networks at the leading edge of the cell. In GUVs, fascin assembles highly protrusive stiff bundles, while membrane-bound Arp2/3 complex constructs uniform dendritic networks forming a cortex. The question, however, remains, how do these actin binding proteins interact to construct a composite actin network inside GUVs?

To address this question, I co-encapsulated both fascin and Arp2/3 complex in the presence of actin filaments inside GUVs. At facsin concentrations high enough to induce pronounced membrane protrusions, co-encapsulation of lumenal Arp2/3 entirely dampened

fascin bundle-induced protrusions. Further skeletonizing and analyzing network architectures, we showed that Arp2/3 arrests elongation of protrusive bundles via branching. Next, we performed experiments where we co-encapsulated fascin with membrane-associated Arp2/3 complex. Consistent to lumenal Arp2/3, membrane-associated Arp2/3 also dampened formation of protrusive bundles. Interestingly, fascin also disrupts the uniform symmetry of Arp2/3 cortex by aggregating and polarizing membrane-associated actin networks. Given network polarity and lack of symmetry is a major driving force in directed migration, it is interesting to show that it can be reconstituted in minimal systems through competition of fascin and Arp2/3 complex. These results suggest that the competition for finite actin filaments inside a confinement is a determinant of the emerging architecture.

7.2.3 Differential actin mechanics

Structural and civil engineers have developed a library of truss systems for different construction purposes. Depending on how the truss elements, commonly metal or timber rod, are arranged, the structural property of the entire system greatly varies. So, how does varying assembly of actin filaments alter the mechanics of the whole system? The tools for designing varying actin structures are the actin binding proteins. Some branch, some crosslink, and some bundle. However, although some have shown how upregulation or knockdown of a specific actin binding protein affect the mechanics of a cells, the gap in understanding how different actin architectures dictate cell mechanics is unknown.

Here, I investigated how filamentous actin, actin crosslinks and cortical actin shell, differentially regulate the mechanics of cells using reconstitution inside GUV-based minimal cell models. For perturbing actin GUVs, we built a simple electroperturbation setup which, upon the application of electric field, elliptically deforms dielectric materials such as actin GUVs. First,

we compared the electrodeformability of actin-free GUVs with actin encapsulating GUVs by quantifying extent of elliptical deformation. Our finding reveals that actin filament GUVs significantly dampen deformation and we believe that this is potentially due to polymeric entanglement of actin filaments enhancing the viscoelastic property of the lumen and subsequently reduces the GUV composite's deformability. Next, we reconstituted alpha-actinin constructed actin crosslinks and Arp2/3 assembled actin cortex separately inside GUVs. Interestingly, while cortex GUVs exhibited maximum dampening, crosslinked actin GUVs exhibited a reduced deformability compared to filamentous actin GUVs. These results suggest that, depending on the arrangement of actin filaments and their interaction with the bounding membrane, mechanics of the cell is differentially regulated.

7.2.4 Load-induced network rearrangement

Especially for a dynamic system such as the actin, mechanical characterization is not complete without understanding how it responds to forces. In the last part of my dissertation, I investigated how actin networks respond to external loading. Here, similar to previous chapters, I encapsulated filamentous, bundled and cortical actin networks inside GUVs. To induce controlled external load, I used micropipette aspiration. In response to aspiration and constriction inside micropipettes, we found that filamentous actin GUVs resisted insertion into the pipette. Next, we aspirated on GUVs with fascin-bundled networks. Surprisingly, when aspirated, fascin-bundled actin network GUVs highly reorganized to align into a single thick bundle along the axis of aspiration. Finally, we aspirated on cortex actin GUVs. Here, our findings revealed that, perhaps due to a non-uniform stress distribution over GUVs, actin cortex preferentially reorganized along the membrane. Initially a uniform cortex, upon aspiration, the tip of the protrusion was devoid of actin cortex where regions with reduced membrane curvature exhibited

pronounced cortex localization. Although we do not claim that our observations recapitulate a cellular behavior, we believe that our findings shed some insights on how actin's dynamic response to external forces is a function of the network architecture.

7.3 Future directions

7.3.1 Actin/microtubule crosstalk in minimal systems

To best understand the cytoskeletal module, progressively increasing the complexity of minimal systems towards making the more cell-like while still maintaining modular control is key. An interesting direction to explore in the future would be reconstituting actin-microtubule crosstalk. In cells, these two systems work together to execute a cellular process. For instance, during cell division, the formation of microtubule mitotic spindles, disassembly of lumenal actin networks and formation of contractile ring, are inseparable from one another and anything other than this synergy would hinder division and subsequently life. As the matrix of the cytoplasm, these two fibers are highly interconnected and interdependent. Microtubule growth guided by actin networks, elongation impedance of microtubule via peripheral actin networks and stabilization through anchoring, linkage through protein complexes able to bind to both actin and microtubule, are some of examples by which microtubule and actin networks crosstalk. Bottom-up reconstitution presents a unique platform to investigate the crosstalk between actin and microtubule. For instance, reconstituting cell division can be achieved by leveraging our improved understanding of Arp2/3 complex assembled dendritic cortex mechanics, and further investigating how to reconstitute mitotic spindles in minimal cell models. Merging these two systems of actin and microtubule networks, it is a possibility within reach to recapitulate cellular division in GUV-based minimal systems.

7.3.2 Spatial modularity towards migrating minimal cells

The next challenge in using GUV-based minimal cell models is reconstituting cell function. How do we reconstitute migration, endocytosis or transient shape change? Building from the ground up and studying the role of individual components in a cell process, we can assemble minimal machineries required to recapitulate a cellular process leveraging minimal cell models to dissect and investigate how each element interacts with one another. For instance, to reconstitute a migrating minimal cell, we can aim to design an adherent GUV via reconstituting transmembrane cell adhesion molecules (CAMs). We can further elevate level of complexity and include actin networks linked to CAMs. Progressively adding a component at a time, it could potentially be possible to attain a minimal system housing polar actin assembly able to generate motive forces at the leading edge of the minimal cell with contractile rear while maintain a controlled adhesion to a substrate.

7.3.3 Inducible cell mimics

In a cell, actin dynamics is highly responsive to numerous mechanical, chemical and electrical cues. For instance, activation of Piezo1 in response to a mechanical cue has been shown to induce enhanced mean intensity of a fluorescently labeled actin filament in macrophages, suggesting increased filament assembly (383). Such examples beg the question, can we induce a downstream signaling cascade in a minimal system? Using minimal systems, a study has demonstrated that ATP generation can be triggered to assemble actin filaments by co-encapsulating mitochondria with actin solution inside GUVs (384). In this work, ATP is generation is triggered by externally introducing pyruvate which subsequently enters the GUV through incorporated membrane pores. Similarly, we can study how mechanical cues such as

pressure, changes in action potential, contact through cell-minimal cell junctions and numerous other cues regulate cytoskeletal assembly.

7.3.4 Synthetic cells?

A grand scientific and philosophical question that remains a secret is how life came to be. Although, in theory, we are equipped to untangle every component in a living cell. Yet, even knowing all the elements life is made of, can we reconstitute our way to creating synthetic cellular life? Perhaps this is a very difficult question to address, and I will not attempt to answer. However, I do believe that in our attempt to understand the machinery of life module by module one at a time, we would at least have a better grasp of what exactly our limitations are.

7.4 Conclusions

The mechanics of the cell drives processes that promote its survival. Actin, among the cytoskeletal proteins, is principally responsible for cell division, migration, adhesion, morphology and facilitates numerous other cellular processes. The findings described in this thesis highlight the mechanophenotypical properties of actin networks by studying their formation and response to external cues. In chapters of this thesis, I explored actin mechanics by investigating competition between actin binding proteins for network assembly, characterizing the differential material property of actin networks in confinement, and studying the dynamic response of actin networks in response to external forces. I believe that the contents of this thesis have supplemented our understanding of how actin networks endow cellular mechanics. Although a truly powerful system to modularly dissect biology, the lack of synthesis of molecules in response to cues and lack of dynamic turnovers engender limitations to GUV-based

minimal cell models. I believe that these limitations will be overcome as we gradually and effectively understand the cellular machinery module by module.

Appendix 1: Supplementary Information Text for Chapter 5

Numerical method

The parameters used in this numerical analysis are summarized in **Table S1**. Consider a GUV comprised of charge-free bilipid membrane with its interior and exterior filled with a fluid of viscosities μ_{in} and μ_{ex} respectively. To model the electrohydrodynamics, we will employ the leaky dielectric model (385), which combines the Ohm's law for electric current conservation and the Stokes equations for fluid motion. The fluid velocity u satisfies

$$-\mu\nabla p + \Delta \boldsymbol{u} = 0, \quad \nabla \cdot \mathbf{u} = 0,$$

in the interior and exterior of the vesicles subject to a far-field condition and a no-slip boundary condition at the GUV boundary γ. In addition, at γ, the membrane elastic forces balance the electric and hydrodynamic forces, that is, $\mathbf{f}_{mem} = \mathbf{f}_{el} + \mathbf{f}_{hd}$. The membrane elastic forces are obtained by taking the gradient of the Helfrich energy, $E_m = \frac{1}{2}(\int_\gamma \ \kappa_b \kappa^2 d\gamma)$, that is used for modeling the membrane energy. Here, κ_b is the bending modulus and κ is the planar membrane curvature. The local inextensibility of the membrane is enforced by letting the surface divergence of the interfacial velocity vanish, that is,

$$\nabla\gamma \cdot \dot{\boldsymbol{x}} = 0,$$

where **x** is assumed to be the position of the interface. This constraint will be enforced via augmented Lagrangian approach. Thereby, it gives rise to an additional interfacial force due to tension λ, the Lagrange multiplier. The combined expression is given by,

$$\boldsymbol{f}_{el} = -\kappa_b \left(\kappa_{ss} + \frac{\kappa^3}{2} \right) \boldsymbol{n} + (\lambda \boldsymbol{x}_s)_s,$$

where **n** is the outward normal to vesicle interface. The remaining component we require to close the system of equations for vesicle EHD is the electric force $\mathbf{f}_{el}$ acting on the fluid. It is given by the jump in the normal component of the Maxwell stress tensor:

$$\boldsymbol{f}_{el} = \left[\left[\boldsymbol{n} \cdot \left(\epsilon \boldsymbol{E} \otimes \boldsymbol{E} - \frac{1}{2} \epsilon \left| |\boldsymbol{E}| \right|^2 \boldsymbol{I} \right) \right] \right],$$

where ε is the permittivity, **E** is the electric field and [·] is the difference between interior and exterior fields. The ambient electric field is conservative and can be computed from the electric potential, $\mathbf{E} = -\nabla\varphi$, by solving the Laplace equation, $-\Delta\varphi = 0$, in the interior and exterior of the vesicle interface. The boundary conditions at the fluid-membrane interface are obtained by charge and current conservation across the membrane (361). The charge accumulation is governed by: (i) Charge convection by the fluid motion along the surface, (ii) Membrane conductance, with strength G_m, arising from the presence of pores, pumps and ion channels. (iii) Membrane capacitance C_m. Together, the interfacial conditions can be written as

$$\left[\left[\sigma E_n + \epsilon \dot{E}_n \right] \right] = 0$$

$$C_m \dot{V}_m + G_m V_m = \sigma_{ex} E_{n,ex} + \epsilon_{ex} \dot{E}_{n,ex}$$

where σ is the fluid conductivity, E_n is the normal electric field at the membrane interface and $V_m = [[\varphi]]$ is the potential difference across the membrane. The values used for this numerical analysis are summarized in **Table S2**.

In summary, given the initial shape of a GUV, we need to solve for the electric potential and the fluid velocity at the interface, advance the interface position via the kinematic condition, and update the membrane electric variables using (363). We employ the boundary integral formulation developed in (386) for solving the Stokes equations and that of (363,387) for the electric potential problem, with appropriate modifications to account for the imposed AC electric field (as opposed to DC field considered in those works).

Dimensionless parameters used for numerical simulation

Outer solution property

ε_{ex} of 200mM glucose = 79.4 (388) absolute ε_{ex} = 7.03 x 10^{-10}

σ_{ex} of 200 mM glucose = 0.179 mS/m (388)

μ_{ex} of 200 mM glucose = 1mPa.s (389)

Membrane property

C_m = 1μF/cm^2 (390)

A ~10 μm

G_m = 0, assuming intact lipids (390)

κ = 10^{-19} J

Applied Electric field

E_o = 30 kV/m

ω = 5 kHz

Inner solution property (PEG8000 2%, 4%, 8%)

ε_{in} PEG8000 = 80.2, absolute ε_{ex} = 7.1 x 10^{-10}

μ_{in} of 2% PEG = 1.05 mPa.s

μ_{in} of 4% PEG = 3.02 mPa.s

μ_{in} of 8% PEG = 6.94 mPa.s (391)

σ_{in} of 2% PEG = 16.7 dS/cm

σ_{in} of 4% PEG = 14.1 dS/cm

σ_{in} of 8% PEG = 11.7 dSc/m (392)

Electrical conductivity values of aqueous PEG 8000 solutions were acquired from Burnett et. al. (10). In this article, electrical conductivity of PEG 8000 was measured for various PEG 8000 concentrations in Hoagland solution. Within the range of 0-10% w/v PEG8000 concentration, electrical conductivity was measured to have a linear correlation with PEG8000 concentration. To calculate the conductivity of PEG 8000 dissolved in water, we linearly interpolated for unknown values of x% w/v PEG8000 electrical conductivity in water using electrical conductivity of water and Hoagland solution as the independent variables.

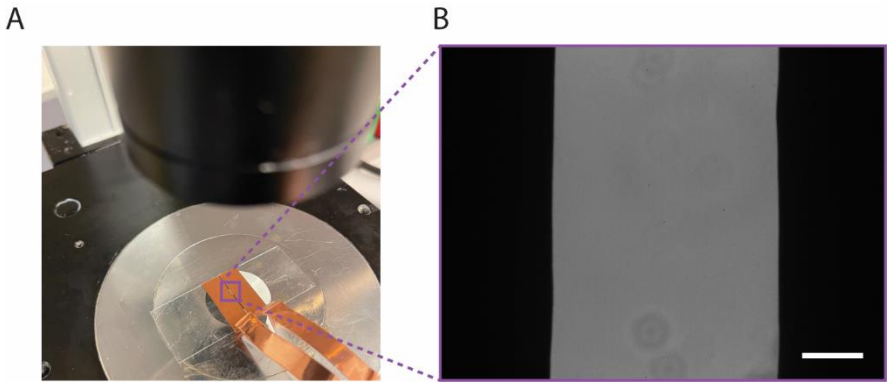

Figure 5-S1 Electrodeformation chamber (A) Electrodefomation chamber made by using copper tapes that are parallelly spaced and uniformly adhered to a coverslip glass. (B) Electrodeformation chamber image acquired using a 20X objective. Dark regions on both sides indicate copper electrodes. Scale bar is 50 μm.

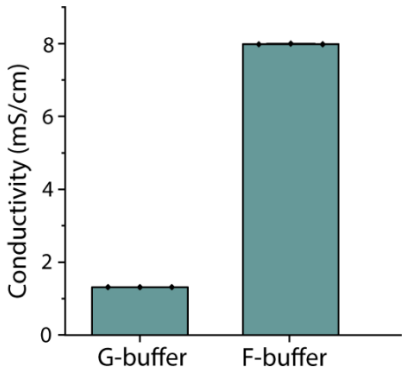

Figure 5-S2 Buffer Conductivity Measured conductivity of buffers used to reconstitute globular actin (G-actin) and filamentous actin (F-actin). Mean ± standard deviation, n = 3.

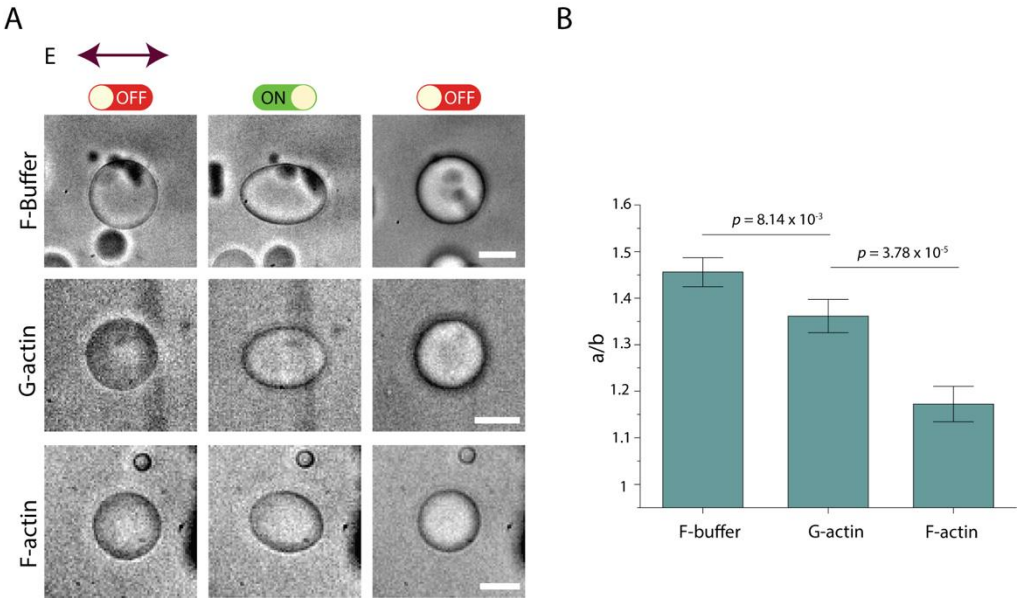

Figure 5-S3 Electrodeformation of GUVs containing F-buffer, 5.3 µM G-actin in G-buffer and 5.3 µM F-actin in F-buffer (A) Brightfield images show transformation of GUVs from unperturbed (left column) to elliptically electrodeformed during application of electric field (middle column) to spherical recovery (right column). F-buffer (top), G-actin (middle), and F-actin (bottom) are compared. (B) Maximum a/b ratio of GUVs from the three conditions

indicated. Data represent mean maximum deformation and error bars denote ± SE. $N_{F\text{-}buffer} = 11$, $N_{G\text{-}actin} = 13$, $N_{F\text{-}actin} = 12$. Scale bars, 10 μm.

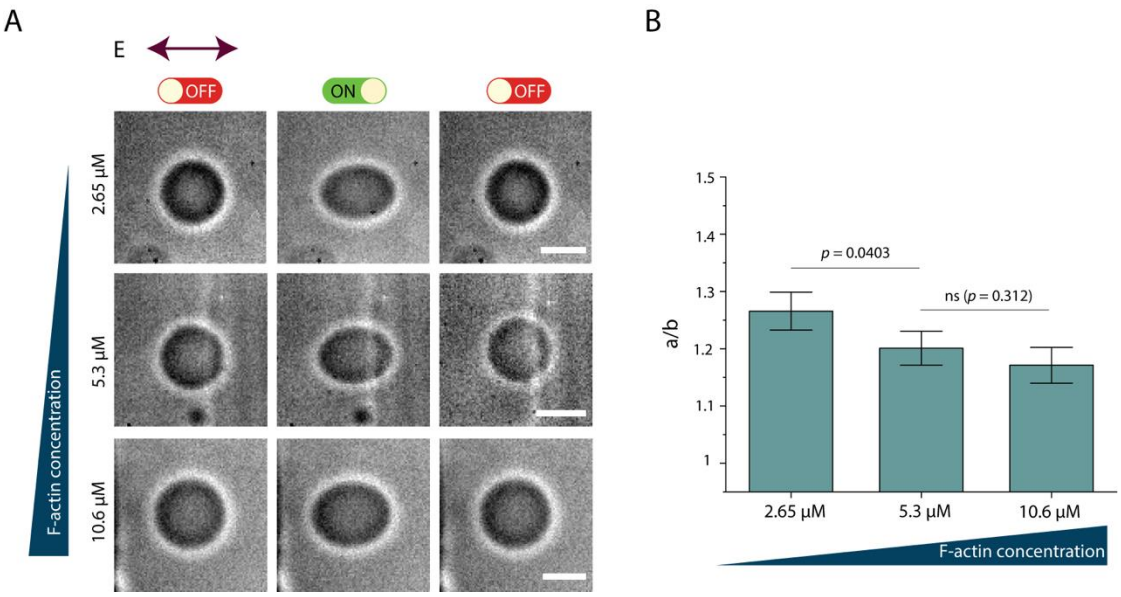

Figure 5-S4 Electrodeformation of GUVs encapsulating F-actin at varying actin concentrations (A) Brightfield images show transformation of GUVs from unperturbed (left column) to elliptically electrodeformed during application of electric field (middle column) to spherical recovery (right column). Images of GUVs with 2.65 µM (top), 5.3 µM (middle), and 10.6 µM (bottom) actin are displayed. (B) Maximum a/b ratio of GUVs from the three conditions indicated. Data represent mean maximum deformation and error bars denote ± SE. $N_{2.65\ \mu M} = 12$, $N_{5.3\ \mu M} = 12$, $N_{10.6\ \mu M} = 11$. Scale bars, 10 µm.

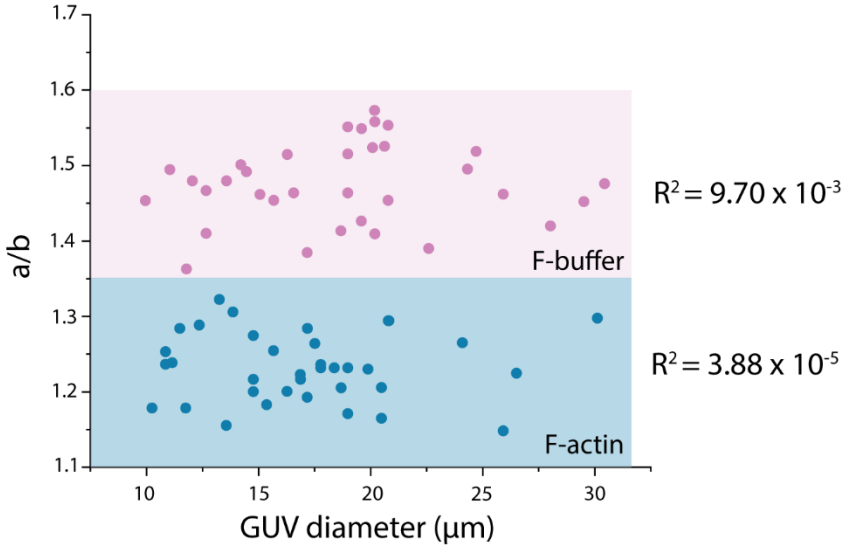

Figure 5-S5 Size-electrodeformation relationship Lack of correlation between GUV size and steady-state GUV deformation during electroperturbation for both GUVs with F-buffer and with 5.3 µM F-actin. Blue data points and shaded area indicate GUV population encapsulating F-actin and pink data points and shaded area indicate GUV population encapsulating F-buffer. $N_{F\text{-}actin}$ = 32, $N_{F\text{-}buffer}$ = 30.

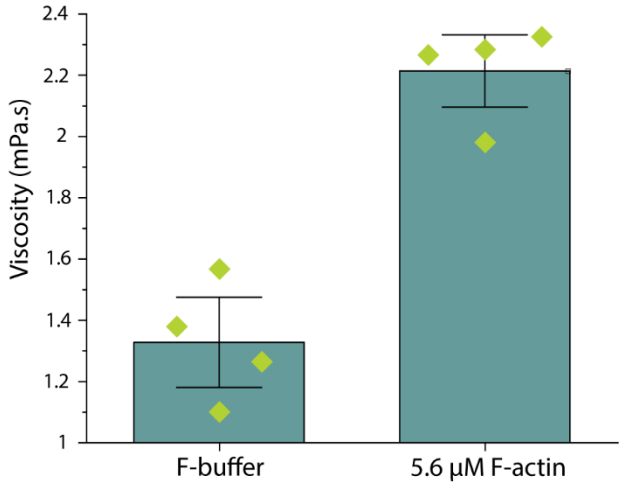

Figure 5-S6 Viscosity measurement of F-buffer and F-actin Measured viscosity of actin polymerization buffer (F-buffer) and 5.3 µM F-actin. Mean ± standard deviation, n = 4.

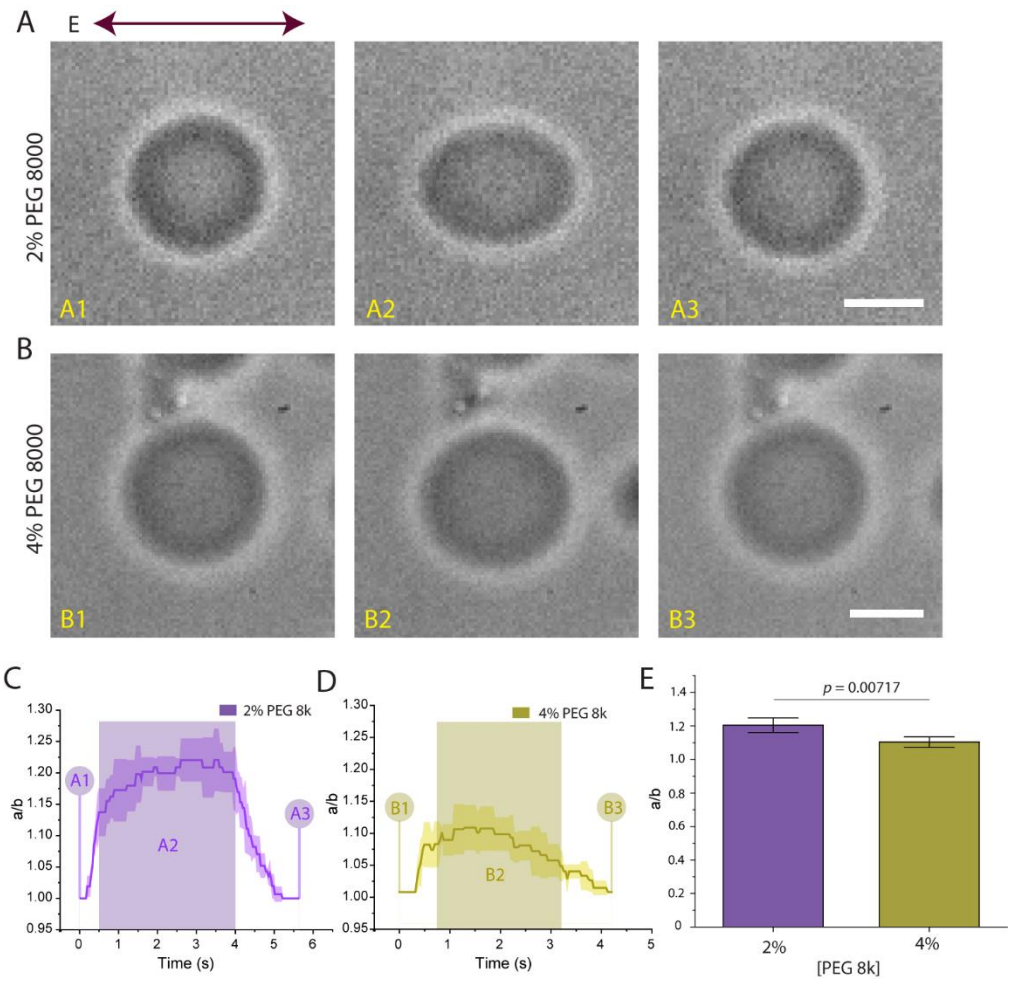

Figure 5-S7 Electroperturbation of GUVs at variable viscosity contrast (η) with a fixed conductivity ratio Λ (A) A sequence of brightfield images shows transformation of 2% PEG 8000 encapsulating GUVs from spherical (A1) to prolate deformed (A2) back to spherical recovery (A3). (B) Electrodeformation of 4% PEG 8000 encapsulating GUVs. Conductivity ratio Λ was matched to that of 2% PEG 8000 by addition of 7.5 mM NaCl. (C,D) Deformation profile of 2 or 4% PEG 8000-containing GUVs in response to 30 kV/m AC field. (E) Comparison and statistical analysis of maximum GUV deformation of each GUV condition as indicated. Data represent mean maximum deformation and error bars denote ± SE. $N_{2\%}$= 10, $N_{4\%}$ = 10. Scale bars, 10 µm.

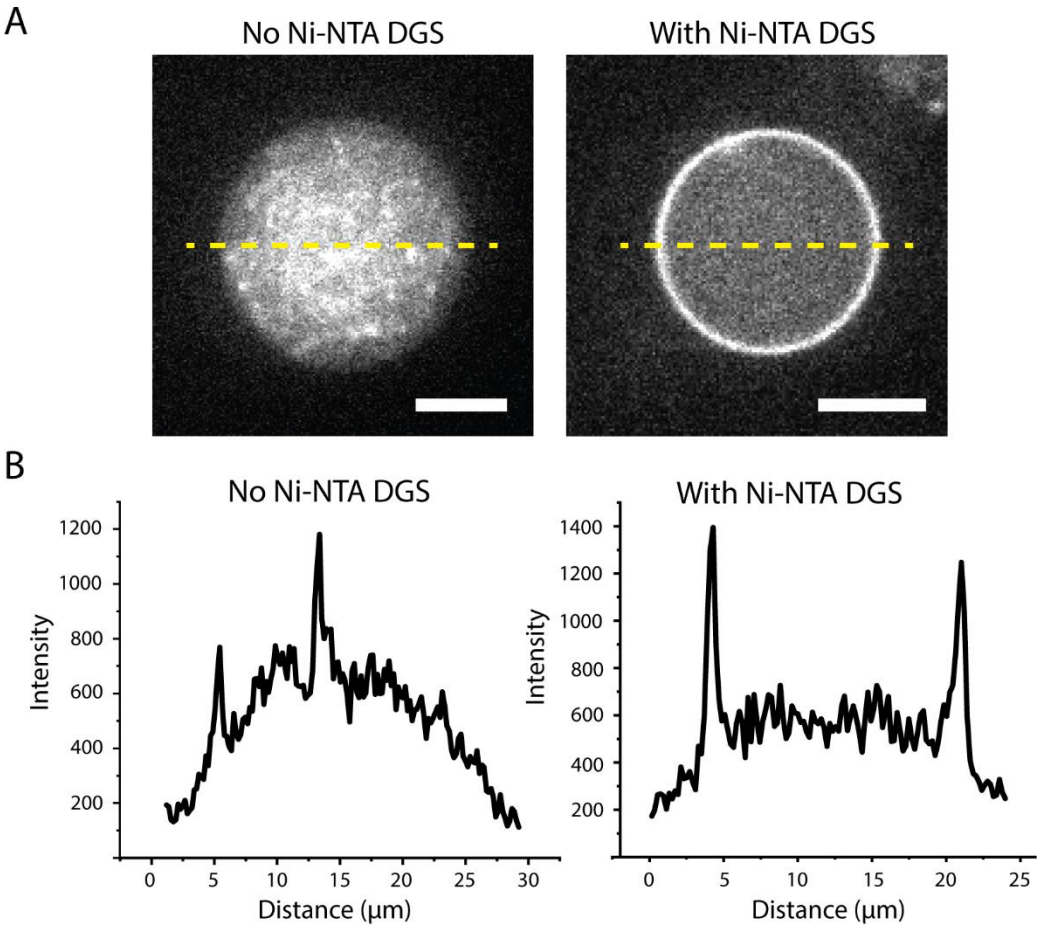

Figure 5-S8 Actin cortex reconstitution (A) Comparison of actin-cortex reconstitution with and without 5% Ni-NTA DGS. (B) Plots of GUV intensity profile of across the dashed line in (A). Scale bars, 10 μm.

Table S1. Appendix of parameters used in numerical analysis of vesicle electroperturbation

Parameters	**Description**
ε_{ex}	Inner solution permittivity
ε_{in}	Outer solution permittivity
σ_{ex}	Outer solution conductivity
σ_{in}	Inner solution conductivity
μ_{in}	Inner solution dynamic viscosity
μ_{ex}	Outer solution dynamic viscosity
C_m	Membrane capacitance
a	Vesicle radius
E_o	Electric field strength
ω	Frequency
G_m	Membrane conductivity
κ	Membrane bending modulus

Bibliography

1. Fletcher DA, Mullins RD. Cell mechanics and the cytoskeleton. Nature [Internet]. 2010;463(7280):485–92. Available from: https://doi.org/10.1038/nature08908
2. Akhmanova A, Steinmetz MO. Control of microtubule organization and dynamics: two ends in the limelight. Nat Rev Mol cell Biol. 2015;16(12):711–26.
3. de Forges H, Bouissou A, Perez F. Interplay between microtubule dynamics and intracellular organization. Int J Biochem Cell Biol. 2012;44(2):266–74.
4. Kumar P, Wittmann T. + TIPs: SxIPping along microtubule ends. Trends Cell Biol. 2012;22(8):418–28.
5. Moores CA, Yu M, Guo J, Beraud C, Sakowicz R, Milligan RA. A mechanism for microtubule depolymerization by KinI kinesins. Mol Cell. 2002;9(4):903–9.
6. Walczak CE, Gayek S, Ohi R. Microtubule-depolymerizing kinesins. Annu Rev Cell Dev Biol. 2013;29:417–41.
7. Dillon RH, Fauci LJ, Omoto C, Yang X. Fluid dynamic models of flagellar and ciliary beating. Ann N Y Acad Sci. 2007;1101(1):494–505.
8. Vaisberg EA, Koonce MP, McIntosh JR. Cytoplasmic dynein plays a role in mammalian mitotic spindle formation. J Cell Biol. 1993;123(4):849–58.
9. Htet ZM, Gillies JP, Baker RW, Leschziner AE, DeSantis ME, Reck-Peterson SL. LIS1 promotes the formation of activated cytoplasmic dynein-1 complexes. Nat Cell Biol. 2020;22(5):518–25.

10. Reed NA, Cai D, Blasius TL, Jih GT, Meyhofer E, Gaertig J, et al. Microtubule acetylation promotes kinesin-1 binding and transport. Curr Biol. 2006;16(21):2166–72.

11. Sanchez AD, Feldman JL. Microtubule-organizing centers: from the centrosome to non-centrosomal sites. Curr Opin Cell Biol. 2017;44:93–101.

12. Karsenti E, Vernos I. The mitotic spindle: a self-made machine. Science (80-). 2001;294(5542):543–7.

13. Walczak CE, Heald R. Mechanisms of mitotic spindle assembly and function. Int Rev Cytol. 2008;265:111–58.

14. Zhou F, Cohan CS. How actin filaments and microtubules steer growth cones to their targets. J Neurobiol. 2004;58(1):84–91.

15. Honore S, Pasquier E, Braguer D. Understanding microtubule dynamics for improved cancer therapy. Cell Mol Life Sci C. 2005;62:3039–56.

16. Fennell BJ, Naughton JA, Barlow J, Brennan G, Fairweather I, Hoey E, et al. Microtubules as antiparasitic drug targets. Expert Opin Drug Discov. 2008;3(5):501–18.

17. Paramio JM, Birgitte Lane E. Keratin intermediate filaments and diseases of the skin. Intermed filaments. 2006;74–82.

18. Fuchs E, Cleveland DW. A structural scaffolding of intermediate filaments in health and disease. Science (80-). 1998;279(5350):514–9.

19. Herrmann H, Bär H, Kreplak L, Strelkov S V, Aebi U. Intermediate filaments: from cell architecture to nanomechanics. Nat Rev Mol cell Biol. 2007;8(7):562–73.

20. Hovnanian A, Pollack E, Hilal L, Rochat A, Prost C, Barrandon Y, et al. A missense mutation in the rod domain of keratin 14 associated with recessive epidermolysis bullosa simplex. Nat Genet. 1993;3(4):327–32.

21. Davidson PM, Lammerding J. Broken nuclei–lamins, nuclear mechanics, and disease. Trends Cell Biol. 2014;24(4):247–56.

22. Khaitlina SY. Functional specificity of actin isoforms. 2001;

23. Perrin BJ, Ervasti JM. The actin gene family: function follows isoform. Cytoskeleton. 2010;67(10):630–4.

24. Kabsch W, Mannherz HG, Suck D, Pai EF, Holmes KC. Atomic structure of the actin: DNase I complex. Nature. 1990;347(6288):37–44.

25. Pollard TD. Actin and actin-binding proteins. Cold Spring Harb Perspect Biol. 2016;8(8):a018226.

26. Korn ED, Carlier M-F, Pantaloni D. Actin polymerization and ATP hydrolysis. Science (80-). 1987;238(4827):638–44.

27. Funk J, Merino F, Venkova L, Heydenreich L, Kierfeld J, Vargas P, et al. Profilin and formin constitute a pacemaker system for robust actin filament growth. Elife. 2019;8:e50963.

28. Krishnan K, Moens PDJ. Structure and functions of profilins. Biophys Rev. 2009;1:71–81.

29. Cooper JA, Sept D. New insights into mechanism and regulation of actin capping protein. Int Rev Cell Mol Biol. 2008;267:183–206.

30. Pavlov D, Muhlrad A, Cooper J, Wear M, Reisler E. Actin filament severing by cofilin. J

Mol Biol. 2007;365(5):1350–8.

31. Goode BL, Eck MJ. Mechanism and function of formins in the control of actin assembly. Annu Rev Biochem. 2007;76:593–627.

32. Vizcarra CL, Bor B, Quinlan ME. The role of formin tails in actin nucleation, processive elongation, and filament bundling. J Biol Chem. 2014;289(44):30602–13.

33. Jayo A, Parsons M. Fascin: a key regulator of cytoskeletal dynamics. Int J Biochem Cell Biol. 2010;42(10):1614–7.

34. Elkhatib N, Neu MB, Zensen C, Schmoller KM, Louvard D, Bausch AR, et al. Fascin plays a role in stress fiber organization and focal adhesion disassembly. Curr Biol. 2014;24(13):1492–9.

35. Pelletier O, Pokidysheva E, Hirst LS, Bouxsein N, Li Y, Safinya CR. Structure of actin cross-linked with α-actinin: a network of bundles. Phys Rev Lett. 2003;91(14):148102.

36. Liu J, Taylor DW, Taylor KA. A 3-D reconstruction of smooth muscle α-actinin by CryoEm reveals two different conformations at the actin-binding region. J Mol Biol. 2004;338(1):115–25.

37. Burridge K, Wittchen ES. The tension mounts: stress fibers as force-generating mechanotransducers. J Cell Biol. 2013;200(1):9–19.

38. Pollard TD, Beltzner CC. Structure and function of the Arp2/3 complex. Curr Opin Struct Biol. 2002;12(6):768–74.

39. Pollard TD. Regulation of actin filament assembly by Arp2/3 complex and formins. Annu Rev Biophys Biomol Struct. 2007;36:451–77.

40. Suraneni P, Rubinstein B, Unruh JR, Durnin M, Hanein D, Li R. The Arp2/3 complex is required for lamellipodia extension and directional fibroblast cell migration. J Cell Biol.

2012;197(2):239–51.

41. Woods A, Wang G, Beier F. Regulation of chondrocyte differentiation by the actin cytoskeleton and adhesive interactions. J Cell Physiol. 2007;213(1):1–8.

42. O'Connor RS, Hao X, Shen K, Bashour K, Akimova T, Hancock WW, et al. Substrate rigidity regulates human T cell activation and proliferation. J Immunol. 2012;189(3):1330–9.

43. Schwager SC, Taufalele P V, Reinhart-King CA. Cell–cell mechanical communication in cancer. Cell Mol Bioeng. 2019;12:1–14.

44. Moore SW, Sheetz MP. Biophysics of substrate interaction: influence on neural motility, differentiation, and repair. Dev Neurobiol. 2011;71(11):1090–101.

45. Nemir S, West JL. Synthetic materials in the study of cell response to substrate rigidity. Ann Biomed Eng. 2010;38:2–20.

46. Simonis N, Rual J-F, Carvunis A-R, Tasan M, Lemmens I, Hirozane-Kishikawa T, et al. Empirically controlled mapping of the Caenorhabditis elegans protein-protein interactome network. Nat Methods. 2009;6(1):47–54.

47. Chaudhuri O, Parekh SH, Fletcher DA. Reversible stress softening of actin networks. Nature. 2007;445(7125):295–8.

48. Ideses Y, Brill-Karniely Y, Haviv L, Ben-Shaul A, Bernheim-Groswasser A. Arp2/3 branched actin network mediates filopodia-like bundles formation in vitro. PLoS One. 2008;3(9):e3297.

49. Landino J, Leda M, Michaud A, Swider ZT, Prom M, Field CM, et al. Rho and F-actin self-organize within an artificial cell cortex. Curr Biol. 2021;31(24):5613–21.

50. Bashirzadeh Y, Liu AP. Encapsulation of the cytoskeleton: towards mimicking the

mechanics of a cell. Soft Matter. 2019;15(42):8425–36.

51. Vahey MD, Fletcher DA. The biology of boundary conditions: Cellular reconstitution in one, two, and three dimensions. Curr Opin Cell Biol. 2014;26(1):60–8.

52. Liu AP, Richmond DL, Maibaum L, Pronk S, Geissler PL, Fletcher DA. Membrane-induced bundling of actin filaments. Nat Phys. 2008;4(10):789–93.

53. Noireaux V, Liu AP. The New Age of Cell-Free Biology. 2020;

54. Hayashi K, Iwata M. Stiffness of cancer cells measured with an AFM indentation method. J Mech Behav Biomed Mater. 2015;49:105–11.

55. Fu J, Wang Y-K, Yang MT, Desai RA, Yu X, Liu Z, et al. Mechanical regulation of cell function with geometrically modulated elastomeric substrates. Nat Methods. 2010;7(9):733.

56. Evans E, Needham D. Physical properties of surfactant bilayer membranes: thermal transitions, elasticity, rigidity, cohesion and colloidal interactions. J Phys Chem. 1987;91(16):4219–28.

57. Evans E, Heinrich V, Ludwig F, Rawicz W. Dynamic tension spectroscopy and strength of biomembranes. Biophys J. 2003;85(4):2342–50.

58. Delorme N, Fery A. Direct method to study membrane rigidity of small vesicles based on atomic force microscope force spectroscopy. Phys Rev E - Stat Nonlinear, Soft Matter Phys. 2006;74(3):030901.

59. Carvalho K, Lemière J, Faqir F, Manzi J, Blanchoin L, Plastino J, et al. Actin polymerization or myosin contraction: two ways to build up cortical tension for symmetry breaking. Philos Trans R Soc B Biol Sci. 2013;368(1629):20130005.

60. Brungs S, Hauslage J, Hilbig R, Hemmersbach R, Anken R. Effects of simulated

weightlessness on fish otolith growth: clinostat versus rotating-wall vessel. Adv Sp Res. 2011;48(5):792–8.

61. Groaz A, Moghimianavval H, Tavella F, Giessen TW, Vecchiarelli AG, Yang Q, et al. Engineering spatiotemporal organization and dynamics in synthetic cells. Wiley Interdiscip Rev Nanomedicine Nanobiotechnology. 2021;13(3):e1685.

62. Koga S, Williams DS, Perriman AW, Mann S. Peptide–nucleotide microdroplets as a step towards a membrane-free protocell model. Nat Chem. 2011;3(9):720–4.

63. Tang T-YD, Antognozzi M, Vicary JA, Perriman AW, Mann S. Small-molecule uptake in membrane-free peptide/nucleotide protocells. Soft Matter. 2013;9(31):7647–56.

64. Jiao D, Geng J, Loh XJ, Das D, Lee T, Scherman OA. Supramolecular peptide amphiphile vesicles through host–guest complexation. Angew Chemie Int Ed. 2012;51(38):9633–7.

65. Rideau E, Wurm FR, Landfester K. Giant polymersomes from non-assisted film hydration of phosphate-based block copolymers. Polym Chem. 2018;9(44):5385–94.

66. Zhang L, Eisenberg A. Multiple morphologies of" crew-cut" aggregates of polystyrene-b-poly (acrylic acid) block copolymers. Science (80-). 1995;268(5218):1728–31.

67. Sharma B, Moghimianavval H, Hwang SW, Liu AP. Synthetic cell as a platform for understanding membrane-membrane interactions. Vol. 11, Membranes. 2021.

68. Liu X, Zhou P, Huang Y, Li M, Huang X, Mann S. Hierarchical proteinosomes for programmed release of multiple components. Angew Chemie. 2016;128(25):7211–6.

69. Ganar KA, Leijten L, Deshpande S. Actinosomes: Condensate-Templated Containers for Engineering Synthetic Cells. ACS Synth Biol. 2022;

70. Bashirzadeh Y, Wubshet N, Litschel T, Schwille P, Liu AP. Rapid Encapsulation of Reconstituted Cytoskeleton inside Giant Unilamellar Vesicles. J Vis Exp Jove.

2021;(177).

71. Göpfrich K, Haller B, Staufer O, Dreher Y, Mersdorf U, Platzman I, et al. One-Pot Assembly of Complex Giant Unilamellar Vesicle-Based Synthetic Cells. ACS Synth Biol. 2019;

72. Stachowiak JC, Richmond DL, Li TH, Liu AP, Parekh SH, Fletcher DA. Unilamellar vesicle formation and encapsulation by microfluidic jetting. Proc Natl Acad Sci. 2008;105(12):4697–702.

73. Majumder S, Wubshet N, Liu AP. Encapsulation of complex solutions using droplet microfluidics towards the synthesis of artificial cells. J Micromechanics Microengineering. 2019;29(8):83001.

74. Ganzinger KA, Merino-Salomón A, García-Soriano DA, Butterfield AN, Litschel T, Siedler F, et al. FtsZ reorganization facilitates deformation of giant vesicles in microfluidic traps. Angew Chemie Int Ed. 2020;59(48):21372–6.

75. Litschel T, Kelley CF, Holz D, Koudehi MA, Vogel SK, Burbaum L, et al. Reconstitution of contractile actomyosin rings in vesicles. Nat Commun. 2021;12(1):1–10.

76. Majumder S, Garamella J, Wang Y-L, DeNies M, Noireaux V, Liu AP. Cell-sized mechanosensitive and biosensing compartment programmed with DNA. Chem Commun. 2017;53(53):7349–52.

77. Krishnan S, Ziegler D, Arnaut V, Martin TG, Kapsner K, Henneberg K, et al. Molecular transport through large-diameter DNA nanopores. Nat Commun. 2016;7(1):1–7.

78. Yuan F, Alimohamadi H, Bakka B, Trementozzi AN, Day KJ, Fawzi NL, et al. Membrane bending by protein phase separation. Proc Natl Acad Sci. 2021 Mar 16;118(11).

79. Chaudhary H, Subramaniam V, Claessens MMAE. Direct Visualization of Model

Membrane Remodeling by α-Synuclein Fibrillization. ChemPhysChem. 2017;18(12):1620–6.

80. Wubshet NH, Bashirzadeh Y, Liu AP. Fascin-induced actin protrusions are suppressed by dendritic networks in giant unilamellar vesicles. Mol Biol Cell. 2021 Aug 19;32(18):1634–40.

81. Wubshet NH, Wu B, Veerapaneni S, Liu AP. Differential regulation of GUV mechanics via actin network architectures. bioRxiv. 2022;

82. Bashirzadeh Y, Moghimianavval H, Liu AP. Encapsulated actomyosin patterns drive cell-like membrane shape changes. Iscience. 2022;25(5):104236.

83. Bashirzadeh Y, Wubshet NH, Liu AP. Confinement Geometry Tunes Fascin-Actin Bundle Structures and Consequently the Shape of a Lipid Bilayer Vesicle. Front Mol Biosci. 2020;7.

84. Hayashi M, Nishiyama M, Kazayama Y, Toyota T, Harada Y, Takiguchi K. Reversible morphological control of tubulin-encapsulating giant liposomes by hydrostatic pressure. Langmuir. 2016;32(15):3794–802.

85. Fujii S, Matsuura T, Sunami T, Kazuta Y, Yomo T. In vitro evolution of α-hemolysin using a liposome display. Proc Natl Acad Sci. 2013;110(42):16796–801.

86. Moghimianavval H, Patel C, Mohapatra S, Hwang S, Kayikcioglu T, Bashirzadeh Y, et al. Engineering Functional Membrane–Membrane Interfaces by InterSpy. Small. 2022;2202104.

87. Bartelt SM, Steinkühler J, Dimova R, Wegner S V. Light-guided motility of a minimal synthetic cell. Nano Lett. 2018;18(11):7268–74.

88. Kohyama S, Merino-Salomón A, Schwille P. In vitro assembly, positioning and

contraction of a division ring in minimal cells. Nat Commun [Internet]. 2022;13(1):6098. Available from: https://doi.org/10.1038/s41467-022-33679-x

89. Berhanu S, Ueda T, Kuruma Y. Artificial photosynthetic cell producing energy for protein synthesis. Nat Commun 2019 101 [Internet]. 2019 Mar 22 [cited 2021 Sep 8];10(1):1–10. Available from: https://www.nature.com/articles/s41467-019-09147-4

90. Wesołowska O, Michalak K, Maniewska J, Hendrich AB. Giant unilamellar vesicles-a perfect tool to visualize phase separation and lipid rafts in model systems. Acta Biochim Pol. 2009;56(1).

91. Solmaz ME, Sankhagowit S, Biswas R, Mejia CA, Povinelli ML, Malmstadt N. Optical stretching as a tool to investigate the mechanical properties of lipid bilayers. RSC Adv. 2013;3(37):16632–8.

92. Karal MAS, Ahamed M, Rahman M, Ahmed M, Shakil M, Siddique-e-Rabbani K. Effects of electrically-induced constant tension on giant unilamellar vesicles using irreversible electroporation. Eur Biophys J. 2019;48(8):731–41.

93. OSTER GF, MOORE H-PH. The budding of membranes. In: Cell to Cell Signalling. Elsevier; 1989. p. 171–87.

94. Winocour PD, Watala C, Perry DW, Kinlough-Rathbone RL. Decreased platelet membrane fluidity due to glycation or acetylation of membrane proteins. Thromb Haemost. 1992;68(11):577–82.

95. Maurya SR, Chaturvedi D, Mahalakshmi R. Modulating lipid dynamics and membrane fluidity to drive rapid folding of a transmembrane barrel. Sci Rep. 2013;3(1):1–6.

96. Kato N, Ishijima A, Inaba T, Nomura F, Takeda S, Takiguchi K. Effects of lipid composition and solution conditions on the mechanical properties of membrane vesicles.

Membranes (Basel). 2015;5(1):22–47.

97. Endress E, Bayerl S, Prechtel K, Maier C, Merkel R, Bayerl TM. The effect of cholesterol, lanosterol, and ergosterol on lecithin bilayer mechanical properties at molecular and microscopic dimensions: a solid-state NMR and micropipet study. Langmuir. 2002;18(8):3293–9.

98. Gracia RS, Bezlyepkina N, Knorr RL, Lipowsky R, Dimova R. Effect of cholesterol on the rigidity of saturated and unsaturated membranes: fluctuation and electrodeformation analysis of giant vesicles. Soft Matter. 2010;6(7):1472–82.

99. Elani Y, Purushothaman S, Booth PJ, Seddon JM, Brooks NJ, Law R V, et al. Measurements of the effect of membrane asymmetry on the mechanical properties of lipid bilayers. Chem Commun. 2015;51(32):6976–9.

100. Girard P, Prost J, Bassereau P. Passive or active fluctuations in membranes containing proteins. Phys Rev Lett. 2005;94(8):88102.

101. Mora NL, Findlay HE, Brooks NJ, Purushothaman S, Ces O, Booth PJ. The membrane transporter lactose permease increases lipid bilayer bending rigidity. Biophys J. 2021;120(17):3787–94.

102. Kang JY, Choi I, Seo M, Lee JY, Hong S, Gong G, et al. Enhancing membrane modulus of giant unilamellar lipid vesicles by lateral co-assembly of amphiphilic triblock copolymers. J Colloid Interface Sci. 2020;561:318–26.

103. Lira RB, Dimova R, Riske KA. Giant unilamellar vesicles formed by hybrid films of agarose and lipids display altered mechanical properties. Biophys J. 2014;107(7):1609–19.

104. Okano T, Inoue K, Koseki K, Suzuki H. Deformation modes of giant unilamellar vesicles encapsulating biopolymers. ACS Synth Biol. 2018;7(2):739–47.

105. Schäfer E, Kliesch T-T, Janshoff A. Mechanical properties of giant liposomes compressed between two parallel plates: impact of artificial actin shells. Langmuir. 2013;29(33):10463–74.

106. Perrier DL, Vahid A, Kathavi V, Stam L, Rems L, Mulla Y, et al. Response of an actin network in vesicles under electric pulses. Sci Rep. 2019;9(1):1–11.

107. Vlès F. Recherches sur une déformation mécanique des œufs d'Oursin. Arch Zool exp gin. 1933;75:421–63.

108. Mitchison JM, Swann MM. The mechanical properties of the cell surface: III. The sea-urchin egg from fertilization to cleavage. J Exp Biol. 1955;32(4):734–50.

109. Rand RP, Burton AC. Mechanical properties of the red cell membrane: I. Membrane stiffness and intracellular pressure. Biophys J. 1964;4(2):115–35.

110. Evans EA, Hochmuth RM. Mechanochemical properties of membranes. In: Current topics in membranes and transport. Elsevier; 1978. p. 1–64.

111. Biro M, Maître J-L. Dual pipette aspiration: a unique tool for studying intercellular adhesion. In: Methods in Cell biology. Elsevier; 2015. p. 255–67.

112. Needham D. Micropipette Manipulation of Lipid Bilayer Membranes BT - Encyclopedia of Biophysics. In: Roberts GCK, editor. Berlin, Heidelberg: Springer Berlin Heidelberg; 2013. p. 1524–38. Available from: https://doi.org/10.1007/978-3-642-16712-6_562

113. Boytsov D, Hannesschlaeger C, Horner A, Siligan C, Pohl P. Micropipette Aspiration-Based Assessment of Single Channel Water Permeability. Biotechnol J. 2020;15(7):1900450.

114. Prévost C, Zhao H, Manzi J, Lemichez E, Lappalainen P, Callan-Jones A, et al. IRSp53 senses negative membrane curvature and phase separates along membrane tubules. Nat

Commun. 2015;6(1):1–11.

115. Bo L, Waugh RE. Determination of bilayer membrane bending stiffness by tether formation from giant, thin-walled vesicles. Biophys J. 1989;55(3):509–17.

116. Needham D, Nunn RS. Elastic deformation and failure of lipid bilayer membranes containing cholesterol. Biophys J. 1990;58(4):997–1009.

117. Henriksen JR, Ipsen JH. Measurement of membrane elasticity by micro-pipette aspiration. Eur Phys J E. 2004;14(2):149–67.

118. Portet T, Gordon SE, Keller SL. Increasing membrane tension decreases miscibility temperatures; an experimental demonstration via micropipette aspiration. Biophys J. 2012;103(8):L35–7.

119. Sorre B, Callan-Jones A, Manneville J-B, Nassoy P, Joanny J-F, Prost J, et al. Curvature-driven lipid sorting needs proximity to a demixing point and is aided by proteins. Proc Natl Acad Sci. 2009;106(14):5622–6.

120. Needham D, Evans E. Structure and mechanical properties of giant lipid (DMPC) vesicle bilayers from 20. degree. C below to 10. degree. C above the liquid crystal-crystalline phase transition at 24. degree. C. Biochemistry. 1988;27(21):8261–9.

121. Bagatolli LA, Needham D. Quantitative optical microscopy and micromanipulation studies on the lipid bilayer membranes of giant unilamellar vesicles. Chem Phys Lipids. 2014;181:99–120.

122. Prévost C, Tsai F-C, Bassereau P, Simunovic M. Pulling membrane nanotubes from giant unilamellar vesicles. JoVE (Journal Vis Exp. 2017;(130):e56086.

123. Roy D, Steinkühler J, Zhao Z, Lipowsky R, Dimova R. Mechanical Tension of Biomembranes Can Be Measured by Super Resolution (STED) Microscopy of Force-

Induced Nanotubes. Nano Lett. 2020;20(5):3185–91.

124. Alessandrini A, Facci P. AFM: a versatile tool in biophysics. Meas Sci Technol. 2005;16(6):R65.

125. Schäfer E, Vache M, Kliesch T-T, Janshoff A. Mechanical response of adherent giant liposomes to indentation with a conical AFM-tip. Soft Matter. 2015;11(22):4487–95.

126. Marchetti M, Wuite GJL, Roos WH. Atomic force microscopy observation and characterization of single virions and virus-like particles by nano-indentation. Curr Opin Virol. 2016;18:82–8.

127. Braet F, de Zanger R, Seynaeve C, Baekeland M, Wisse E. A comparative atomic force microscopy study on living skin fibroblasts and liver endothelial cells. Microscopy. 2001;50(4):283–90.

128. Ricci D, Tedesco M, Grattarola M. Mechanical and morphological properties of living 3T6 cells probed via scanning force microscopy. Microsc Res Tech. 1997;36(3):165–71.

129. Rotsch C, Jacobson K, Radmacher M. Dimensional and mechanical dynamics of active and stable edges in motile fibroblasts investigated by using atomic force microscopy. Proc Natl Acad Sci. 1999;96(3):921–6.

130. Collinsworth AM, Zhang S, Kraus WE, Truskey GA. Apparent elastic modulus and hysteresis of skeletal muscle cells throughout differentiation. Am J Physiol Physiol. 2002;283(4):C1219–27.

131. Lekka M, Gil D, Pogoda K, Dulińska-Litewka J, Jach R, Gostek J, et al. Cancer cell detection in tissue sections using AFM. Arch Biochem Biophys. 2012;518(2):151–6.

132. Xu W, Mezencev R, Kim B, Wang L, McDonald J, Sulchek T. Cell stiffness is a biomarker of the metastatic potential of ovarian cancer cells. PLoS One. 2012;7(10).

133. Haga H, Sasaki S, Kawabata K, Ito E, Ushiki T, Sambongi T. Elasticity mapping of living fibroblasts by AFM and immunofluorescence observation of the cytoskeleton. Ultramicroscopy. 2000;82(1–4):253–8.

134. Lamour G, Allard A, Pelta J, Labdi S, Lenz M, Campillo C. Mapping and modeling the nanomechanics of bare and protein-coated lipid nanotubes. Phys Rev X. 2020;10(1):11031.

135. Zhang CY, Zhang YW. Effects of membrane pre-stress and intrinsic viscoelasticity on nanoindentation of cells using AFM. Philos Mag. 2007;87(23):3415–35.

136. Al-Rekabi Z, Contera S. Multifrequency AFM reveals lipid membrane mechanical properties and the effect of cholesterol in modulating viscoelasticity. Proc Natl Acad Sci. 2018;115(11):2658–63.

137. Parekh SH, Chaudhuri O, Theriot JA, Fletcher DA. Loading history determines the velocity of actin-network growth. Nat Cell Biol. 2005;7(12):1219–23.

138. Dyson M, Woodward B, Pond JB. Flow of red blood cells stopped by ultrasound. Nature. 1971;232(5312):572–3.

139. Baker NV. Segregation and sedimentation of red blood cells in ultrasonic standing waves. Nature. 1972;239(5372):398–9.

140. Armstrong JPK, Puetzer JL, Serio A, Guex AG, Kapnisi M, Breant A, et al. Engineering anisotropic muscle tissue using acoustic cell patterning. Adv Mater. 2018;30(43):1802649.

141. Gesellchen F, Bernassau AL, Dejardin T, Cumming DRS, Riehle MO. Cell patterning with a heptagon acoustic tweezer–application in neurite guidance. Lab Chip. 2014;14(13):2266–75.

142. Kim MG, Park J, Lim HG, Yoon S, Lee C, Chang JH, et al. Label-free analysis of the

characteristics of a single cell trapped by acoustic tweezers. Sci Rep. 2017;7(1):1–9.

143. Hammarström B, Evander M, Barbeau H, Bruzelius M, Larsson J, Laurell T, et al. Non-contact acoustic cell trapping in disposable glass capillaries. Lab Chip. 2010;10(17):2251–7.

144. Collins DJ, Morahan B, Garcia-Bustos J, Doerig C, Plebanski M, Neild A. Two-dimensional single-cell patterning with one cell per well driven by surface acoustic waves. Nat Commun. 2015;6(1):1–11.

145. Ma Z, Zhou Y, Collins DJ, Ai Y. Fluorescence activated cell sorting via a focused traveling surface acoustic beam. Lab Chip. 2017;17(18):3176–85.

146. Ren L, Chen Y, Li P, Mao Z, Huang P-H, Rufo J, et al. A high-throughput acoustic cell sorter. Lab Chip. 2015;15(19):3870–9.

147. Franke T, Braunmüller S, Schmid L, Wixforth A, Weitz DA. Surface acoustic wave actuated cell sorting (SAWACS). Lab Chip. 2010;10(6):789–94.

148. Sorkin R, Bergamaschi G, Kamsma D, Brand G, Dekel E, Ofir-Birin Y, et al. Probing cellular mechanics with acoustic force spectroscopy. Mol Biol Cell. 2018;29(16):2005–11.

149. Kang JH, Miettinen TP, Chen L, Olcum S, Katsikis G, Doyle PS, et al. Noninvasive monitoring of single-cell mechanics by acoustic scattering. Nat Methods. 2019;16(3):263–9.

150. Hwang JY, Kim J, Park JM, Lee C, Jung H, Lee J, et al. Cell deformation by single-beam acoustic trapping: a promising tool for measurements of cell mechanics. Sci Rep. 2016;6(1):1–8.

151. Mishra P, Hill M, Glynne-Jones P. Deformation of red blood cells using acoustic radiation forces. Biomicrofluidics. 2014;8(3):34109.

152. Silva GT, Tian L, Franklin A, Wang X, Han X, Mann S, et al. Acoustic deformation for the extraction of mechanical properties of lipid vesicle populations. Phys Rev E. 2019;99(6):63002.

153. Wang X, Tian L, Du H, Li M, Mu W, Drinkwater BW, et al. Chemical communication in spatially organized protocell colonies and protocell/living cell micro-arrays. Chem Sci. 2019;10(41):9446–53.

154. Guo F, Mao Z, Chen Y, Xie Z, Lata JP, Li P, et al. Three-dimensional manipulation of single cells using surface acoustic waves. Proc Natl Acad Sci. 2016;113(6):1522–7.

155. Guex AG, Di Marzio N, Eglin D, Alini M, Serra T. The waves that make the pattern: A review on acoustic manipulation in biomedical research. Mater Today Bio. 2021;10:100110.

156. Wang X, Tian L, Ren Y, Zhao Z, Du H, Zhang Z, et al. Chemical information exchange in organized protocells and natural cell assemblies with controllable spatial positions. Small. 2020;16(27):1906394.

157. Ashkin A, Dziedzic JM. Optical trapping and manipulation of viruses and bacteria. Science (80-). 1987;235(4795):1517–20.

158. Ashkin A, Dziedzic JM, Yamane T. Optical trapping and manipulation of single cells using infrared laser beams. Nature. 1987;330(6150):769–71.

159. Guck J, Ananthakrishnan R, Moon TJ, Cunningham CC, Käs J. Optical deformability of soft biological dielectrics. Phys Rev Lett. 2000;84(23):5451.

160. Maloney JM, Nikova D, Lautenschläger F, Clarke E, Langer R, Guck J, et al. Mesenchymal stem cell mechanics from the attached to the suspended state. Biophys J. 2010;99(8):2479–87.

161. Mierke CT. The role of the optical stretcher is crucial in the investigation of cell mechanics regulating cell adhesion and motility. Front Cell Dev Biol. 2019;7:184.

162. Guck J, Ananthakrishnan R, Mahmood H, Moon TJ, Cunningham CC, Käs J. The optical stretcher: a novel laser tool to micromanipulate cells. Biophys J. 2001;81(2):767–84.

163. Guck J, Schinkinger S, Lincoln B, Wottawah F, Ebert S, Romeyke M, et al. Optical deformability as an inherent cell marker for testing malignant transformation and metastatic competence. Biophys J. 2005;88(5):3689–98.

164. Remmerbach TW, Wottawah F, Dietrich J, Lincoln B, Wittekind C, Guck J. Oral cancer diagnosis by mechanical phenotyping. Cancer Res. 2009;69(5):1728–32.

165. Huang L, Liang F, Feng Y, Zhao P, Wang W. On-chip integrated optical stretching and electrorotation enabling single-cell biophysical analysis. Microsystems Nanoeng. 2020;6(1):1–14.

166. Yao Z, Kwan CC, Poon AW. An optofluidic “tweeze-and-drag” cell stretcher in a microfluidic channel. Lab Chip. 2020;20(3):601–13.

167. Zheng Y, Sun Y. Microfluidic devices for mechanical characterisation of single cells in suspension. Micro Nano Lett. 2011;6(5):327–31.

168. Nava G, Bragheri F, Yang T, Minzioni P, Osellame R, Cristiani I, et al. All-silica microfluidic optical stretcher with acoustophoretic prefocusing. Microfluid Nanofluidics. 2015;19(4):837–44.

169. Delabre U, Feld K, Crespo E, Whyte G, Sykes C, Seifert U, et al. Deformation of phospholipid vesicles in an optical stretcher. Soft Matter. 2015;11(30):6075–88.

170. Solmaz ME, Biswas R, Sankhagowit S, Thompson JR, Mejia CA, Malmstadt N, et al. Optical stretching of giant unilamellar vesicles with an integrated dual-beam optical trap.

Biomed Opt Express. 2012;3(10):2419–27.

171. Wu S-H, Sankhagowit S, Biswas R, Wu S, Povinelli ML, Malmstadt N. Viscoelastic deformation of lipid bilayer vesicles. Soft Matter. 2015;11(37):7385–91.

172. Sankhagowit S, Wu S-H, Biswas R, Riche CT, Povinelli ML, Malmstadt N. The dynamics of giant unilamellar vesicle oxidation probed by morphological transitions. Biochim Biophys Acta (BBA)-Biomembranes. 2014;1838(10):2615–24.

173. Trank JW. A statistical study of the effects of electric fields on the movements of mammalian sperm cells. IRE Trans Med Electron. 1959;(3):174–9.

174. Teige K, Starý Z. Aggregation of Red Blood Cells in a Strong Electric Field. Nature. 1946;158(4022):794.

175. Sale AJH, Hamilton WA. Effects of high electric fields on micro-organisms: III. Lysis of erythrocytes and protoplasts. Biochim Biophys Acta (BBA)-Biomembranes. 1968;163(1):37–43.

176. Hamilton WA, Sale AJH. Effects of high electric fields on microorganisms: II. Mechanism of action of the lethal effect. Biochim Biophys Acta (BBA)-General Subj. 1967;148(3):789–800.

177. Nuccitelli R, Tran K, Sheikh S, Athos B, Kreis M, Nuccitelli P. Optimized nanosecond pulsed electric field therapy can cause murine malignant melanomas to self-destruct with a single treatment. Int J Cancer. 2010;127(7):1727–36.

178. Breton M, Mir LM. Microsecond and nanosecond electric pulses in cancer treatments. Bioelectromagnetics. 2012;33(2):106–23.

179. Nuccitelli R, Chen X, Pakhomov AG, Baldwin WH, Sheikh S, Pomicter JL, et al. A new pulsed electric field therapy for melanoma disrupts the tumor’s blood supply and causes

complete remission without recurrence. Int J cancer. 2009;125(2):438–45.

180. Tekle E, Astumian RD, Chock PB. Electroporation by using bipolar oscillating electric field: an improved method for DNA transfection of NIH 3T3 cells. Proc Natl Acad Sci. 1991;88(10):4230–4.

181. Glasspool-Malone J, Somiari S, Drabick JJ, Malone RW. Efficient nonviral cutaneous transfection. Mol Ther. 2000;2(2):140–6.

182. Oshima Y, Sakamoto T, Yamanaka I, Nishi T, Ishibashi T, Inomata H. Targeted gene transfer to corneal endothelium in vivo by electric pulse. Gene Ther. 1998;5(10):1347–54.

183. Scheurich P, Zimmermann U, Mischel M, Lamprecht I. Membrane fusion and deformation of red blood cells by electric fields. Zeitschrift für Naturforsch C. 1980;35(11–12):1081–5.

184. Engelhardt H, Gaub H, Sackmann E. Viscoelastic properties of erythrocyte membranes in high-frequency electric fields. Nature. 1984;307(5949):378–80.

185. Wong PK, Tan W, Ho C-M. Cell relaxation after electrodeformation: effect of latrunculin A on cytoskeletal actin. J Biomech. 2005;38(3):529–35.

186. Urbano RL, Clyne AM. An inverted dielectrophoretic device for analysis of attached single cell mechanics. Lab Chip. 2016;16(3):561–73.

187. Guido I, Xiong C, Jaeger MS, Duschl C. Microfluidic system for cell mechanics analysis through dielectrophoresis. Microelectron Eng. 2012;97:379–82.

188. Chen J, Abdelgawad M, Yu L, Shakiba N, Chien W-Y, Lu Z, et al. Electrodeformation for single cell mechanical characterization. J Micromechanics Microengineering. 2011;21(5):54012.

189. MacQueen LA, Buschmann MD, Wertheimer MR. Mechanical properties of mammalian

cells in suspension measured by electro-deformation. J Micromechanics Microengineering. 2010;20(6):65007.

190. Dimova R, Riske KA, Damijan M. Electrodeformation, electroporation, and electrofusion of giant unilamellar vesicles. Handb Electroporation (ed M Damijan) Springer. 2016;

191. Faizi HA, Dimova R, Vlahovska PM. Electromechanical characterization of biomimetic membranes using electrodeformation of vesicles. Electrophoresis. 2021;42(20).

192. Aranda S, Riske KA, Lipowsky R, Dimova R. Morphological transitions of vesicles induced by alternating electric fields. Biophys J. 2008;95(2):L19–21.

193. Riske KA, Dimova R. Electro-deformation and poration of giant vesicles viewed with high temporal resolution. Biophys J. 2005;88(2):1143–55.

194. Riske KA, Knorr RL, Dimova R. Bursting of charged multicomponent vesicles subjected to electric pulses. Soft Matter. 2009;5(10):1983–6.

195. Needham D, Hochmuth RM. Electro-mechanical permeabilization of lipid vesicles. Role of membrane tension and compressibility. Biophys J. 1989;55(5):1001–9.

196. Tekle E, Astumian RD, Friauf WA, Chock PB. Asymmetric pore distribution and loss of membrane lipid in electroporated DOPC vesicles. Biophys J. 2001;81(2):960–8.

197. Faizi HA, Dimova R, Vlahovska PM. Viscosity of fluid membranes measured from vesicle deformation. bioRxiv. 2021;

198. Du E, Dao M, Suresh S. Quantitative biomechanics of healthy and diseased human red blood cells using dielectrophoresis in a microfluidic system. Extrem Mech Lett. 2014;1:35–41.

199. Adams JC. Roles of fascin in cell adhesion and motility. Curr Opin Cell Biol. 2004;16(5):590–6.

200. Puri S, Thaokar RM. Study of dependence of elasticity on the microstructure of microcapsules using electro-deformation technique. Colloids Surfaces A Physicochem Eng Asp. 2019;569:179–89.

201. Hohne DN, Younger JG, Solomon MJ. Flexible microfluidic device for mechanical property characterization of soft viscoelastic solids such as bacterial biofilms. Langmuir. 2009;25(13):7743–51.

202. Lee D, Erickson A, You T, Dudley AT, Ryu S. Pneumatic microfluidic cell compression device for high-throughput study of chondrocyte mechanobiology. Lab Chip. 2018;18(14):2077–86.

203. Lee LM, Liu AP. A microfluidic pipette array for mechanophenotyping of cancer cells and mechanical gating of mechanosensitive channels. Lab Chip. 2015;15(1):264–73.

204. Wubshet NH, Arreguin-Martinez E, Nail M, Annamalai H, Koerner R, Rousseva M, et al. Simulating microgravity using a random positioning machine for inducing cellular responses to mechanotransduction in human osteoblasts. Rev Sci Instrum. 2021;92(11):114101.

205. Islam M, Mezencev R, McFarland B, Brink H, Campbell B, Tasadduq B, et al. Microfluidic cell sorting by stiffness to examine heterogenic responses of cancer cells to chemotherapy. Cell Death Dis. 2018;9(2):1–12.

206. Wang G, Mao W, Byler R, Patel K, Henegar C, Alexeev A, et al. Stiffness dependent separation of cells in a microfluidic device. PLoS One. 2013;8(10):e75901.

207. Luo YN, Chen DY, Zhao Y, Wei C, Zhao XT, Yue WT, et al. A constriction channel based microfluidic system enabling continuous characterization of cellular instantaneous Young's modulus. Sensors Actuators B Chem. 2014;202:1183–9.

208. Xue C, Wang J, Zhao Y, Chen D, Yue W, Chen J. Constriction channel based single-cell mechanical property characterization. Micromachines. 2015;6(11):1794–804.

209. Pappas D. Microfluidics and cancer analysis: cell separation, cell/tissue culture, cell mechanics, and integrated analysis systems. Analyst. 2016;141(2):525–35.

210. Adamo A, Sharei A, Adamo L, Lee B, Mao S, Jensen KF. Microfluidics-based assessment of cell deformability. Anal Chem. 2012;84(15):6438–43.

211. Chen J, Li J, Sun Y. Microfluidic approaches for cancer cell detection, characterization, and separation. Lab Chip. 2012;12(10):1753–67.

212. Jia H, Litschel T, Heymann M, Eto H, Franquelim HG, Schwille P. Shaping giant membrane vesicles in 3D-printed protein hydrogel cages. Small. 2020;16(27):1906259.

213. Elias M, Dutoya A, Laborde A, Lecestre A, Montis C, Caselli L, et al. Microfluidic characterization of biomimetic membrane mechanics with an on-chip micropipette. Micro Nano Eng. 2020;8:100064.

214. Korlach J, Reichle C, Müller T, Schnelle T, Webb WW. Trapping, deformation, and rotation of giant unilamellar vesicles in octode dielectrophoretic field cages. Biophys J. 2005;89(1):554–62.

215. Robinson T, Kuhn P, Eyer K, Dittrich PS. Microfluidic trapping of giant unilamellar vesicles to study transport through a membrane pore. Biomicrofluidics. 2013;7(4):44105.

216. Bhatia T, Robinson T, Dimova R. Membrane permeability to water measured by microfluidic trapping of giant vesicles. Soft Matter. 2020;16(31):7359–69.

217. Yandrapalli N, Robinson T. Ultra-high capacity microfluidic trapping of giant vesicles for high-throughput membrane studies. Lab Chip. 2019;19(4):626–33.

218. Stark DJ, Killian TC, Raphael RM. A microfabricated magnetic force transducer-

microaspiration system for studying membrane mechanics. Phys Biol. 2011;8(5):56008.

219. Pivetal J, Osman O, Vezy C, Frénéa-Robine M, Dumas-Bouchiat F, Dempsey NM, et al. Trapping of Magnetically-Labelled Liposomes on Flat Micro-Patterned Hard Magnetic Films. In: AIP Conference Proceedings. American Institute of Physics; 2010. p. 192–7.

220. Limozin L, Roth A, Sackmann E. Microviscoelastic moduli of biomimetic cell envelopes. Phys Rev Lett. 2005;95(17):178101.

221. Wiemann JT, Shen Z, Ye H, Li Y, Yu Y. Membrane poration, wrinkling, and compression: deformations of lipid vesicles induced by amphiphilic Janus nanoparticles. Nanoscale. 2020;12(39):20326–36.

222. Li S, Malmstadt N. Deformation and poration of lipid bilayer membranes by cationic nanoparticles. Soft Matter. 2013;9(20):4969–76.

223. Yu Y, Granick S. Pearling of lipid vesicles induced by nanoparticles. J Am Chem Soc. 2009;131(40):14158–9.

224. Wei X, Jiang W, Yu J, Ding L, Hu J, Jiang G. Effects of SiO2 nanoparticles on phospholipid membrane integrity and fluidity. J Hazard Mater. 2015;287:217–24.

225. Chabanon M, Ho JCS, Liedberg B, Parikh AN, Rangamani P. Pulsatile lipid vesicles under osmotic stress. Biophys J. 2017;112(8):1682–91.

226. Oglęcka K, Rangamani P, Liedberg B, Kraut RS, Parikh AN. Oscillatory phase separation in giant lipid vesicles induced by transmembrane osmotic differentials. Elife. 2014;3:e03695.

227. Maan R, Loiseau E, Bausch AR. Adhesion of active cytoskeletal vesicles. Biophys J. 2018;115(12):2395–402.

228. Bagatolli LA, Gratton E. Two-photon fluorescence microscopy observation of shape

changes at the phase transition in phospholipid giant unilamellar vesicles. Biophys J. 1999;77(4):2090–101.

229. Betaneli V, Worch R, Schwille P. Effect of temperature on the formation of liquid phase-separating giant unilamellar vesicles (GUV). Chem Phys Lipids. 2012;165(6):630–7.

230. Crowder SW, Leonardo V, Whittaker T, Papathanasiou P, Stevens MM. Material cues as potent regulators of epigenetics and stem cell function. Cell Stem Cell. 2016;18(1):39–52.

231. Chen L, Wei S, Chiu J. Mechanical regulation of epigenetics in vascular biology and pathobiology. J Cell Mol Med. 2013;17(4):437–48.

232. Vining KH, Mooney DJ. Mechanical forces direct stem cell behaviour in development and regeneration. Nat Rev Mol Cell Biol. 2017;18(12):728.

233. Steward AJ, Kelly DJ. Mechanical regulation of mesenchymal stem cell differentiation. J Anat. 2015;227(6):717–31.

234. Wang J, Chen H, Seth A, McCulloch CA. Mechanical force regulation of myofibroblast differentiation in cardiac fibroblasts. Am J Physiol Circ Physiol. 2003;285(5):H1871–81.

235. Owens GK. Role of mechanical strain in regulation of differentiation of vascular smooth muscle cells. Circ Res. 1996;79(5):1054–5.

236. Handorf AM, Zhou Y, Halanski MA, Li W-J. Tissue stiffness dictates development, homeostasis, and disease progression. Organogenesis. 2015;11(1):1–15.

237. Suki B, Lutchen KR, Ingenito EP. On the progressive nature of emphysema: roles of proteases, inflammation, and mechanical forces. Am J Respir Crit Care Med. 2003;168(5):516–21.

238. Burr DB, Robling AG, Turner CH. Effects of biomechanical stress on bones in animals. Bone. 2002;30(5):781–6.

239. Lee TC, Taylor D. Bone remodelling: Should we cry wolff? Ir J Med Sci. 1999;168(2):102.

240. Yu W, Qu H, Hu G, Zhang Q, Song K, Guan H, et al. A microfluidic-based multi-shear device for investigating the effects of low fluid-induced stresses on osteoblasts. PLoS One. 2014;9(2).

241. Pavalko FM, Chen NX, Turner CH, Burr DB, Atkinson S, Hsieh Y-F, et al. Fluid shear-induced mechanical signaling in MC3T3-E1 osteoblasts requires cytoskeleton-integrin interactions. Am J Physiol Physiol. 1998;275(6):C1591–601.

242. Shao Y, Tan X, Novitski R, Muqaddam M, List P, Williamson L, et al. Uniaxial cell stretching device for live-cell imaging of mechanosensitive cellular functions. Rev Sci Instrum. 2013;84(11):114304.

243. Heureaux J, Chen D, Murray VL, Deng CX, Liu AP. Activation of a bacterial mechanosensitive channel in mammalian cells by cytoskeletal stress. Cell Mol Bioeng. 2014;7(3):307–19.

244. Hayakawa K, Tatsumi H, Sokabe M. Actin stress fibers transmit and focus force to activate mechanosensitive channels. J Cell Sci. 2008;121(4):496–503.

245. Heureaux-Torres J, Luker KE, Haley H, Pirone M, Lee LM, Herrera Y, et al. The effect of mechanosensitive channel MscL expression in cancer cells on 3D confined migration. APL Bioeng. 2018;2(3):32001.

246. Gilbert PM, Havenstrite KL, Magnusson KEG, Sacco A, Leonardi NA, Kraft P, et al. Substrate elasticity regulates skeletal muscle stem cell self-renewal in culture. Science (80-). 2010;329(5995):1078–81.

247. Lv H, Li L, Sun M, Zhang Y, Chen L, Rong Y, et al. Mechanism of regulation of stem cell

differentiation by matrix stiffness. Stem Cell Res Ther. 2015;6(1):103.

248. Watanabe T, Kuramochi H, Takahashi A, Imai K, Katsuta N, Nakayama T, et al. Higher cell stiffness indicating lower metastatic potential in B16 melanoma cell variants and in (−)-epigallocatechin gallate-treated cells. J Cancer Res Clin Oncol. 2012;138(5):859–66.

249. Swaminathan V, Mythreye K, O'Brien ET, Berchuck A, Blobe GC, Superfine R. Mechanical stiffness grades metastatic potential in patient tumor cells and in cancer cell lines. Cancer Res. 2011;71(15):5075–80.

250. Sundaresan A, Risin D, Pellis NR. Cell growth in microgravity. Rev Cell Biol Mol Med. 2006;

251. Ingber D. How cells (might) sense microgravity. FASEB J. 1999;13(9001):S3–15.

252. Liu AP, Chaudhuri O, Parekh SH. New advances in probing cell–extracellular matrix interactions. Integr Biol. 2017;9(5):383–405.

253. Charras GT, Horton MA. Single cell mechanotransduction and its modulation analyzed by atomic force microscope indentation. Biophys J. 2002;82(6):2970–81.

254. Yen M-H, Chen Y-H, Liu Y-S, Lee OK-S. Alteration of Young's modulus in mesenchymal stromal cells during osteogenesis measured by atomic force microscopy. Biochem Biophys Res Commun. 2020;526(3):827–32.

255. Krüger J, Singh K, O'Neill A, Jackson C, Morrison A, O'Brien P. Development of a microfluidic device for fluorescence activated cell sorting. J micromechanics microengineering. 2002;12(4):486.

256. Wang MM, Tu E, Raymond DE, Yang JM, Zhang H, Hagen N, et al. Microfluidic sorting of mammalian cells by optical force switching. Nat Biotechnol. 2005;23(1):83–7.

257. Saliba A-E, Saias L, Psychari E, Minc N, Simon D, Bidard F-C, et al. Microfluidic sorting

and multimodal typing of cancer cells in self-assembled magnetic arrays. Proc Natl Acad Sci. 2010;107(33):14524–9.

258. Garrett-Bakelman FE, Darshi M, Green SJ, Gur RC, Lin L, Macias BR, et al. The NASA Twins Study: A multidimensional analysis of a year-long human spaceflight. Science (80-). 2019;364(6436):eaau8650.

259. Wuest SL, Richard S, Kopp S, Grimm D, Egli M. Simulated microgravity: critical review on the use of random positioning machines for mammalian cell culture. Biomed Res Int. 2015;2015.

260. Ulbrich C, Wehland M, Pietsch J, Aleshcheva G, Wise P, van Loon J, et al. The impact of simulated and real microgravity on bone cells and mesenchymal stem cells. Biomed Res Int. 2014;2014.

261. Clément G, Pavy-Le Traon A. Centrifugation as a countermeasure during actual and simulated microgravity: a review. Eur J Appl Physiol. 2004;92(3):235–48.

262. Grimm D, Wehland M, Pietsch J, Aleshcheva G, Wise P, van Loon J, et al. Growing tissues in real and simulated microgravity: new methods for tissue engineering. Tissue Eng Part B Rev. 2014;20(6):555–66.

263. Herranz R, Larkin OJ, Dijkstra CE, Hill RJA, Anthony P, Davey MR, et al. Microgravity simulation by diamagnetic levitation: effects of a strong gradient magnetic field on the transcriptional profile of Drosophila melanogaster. BMC Genomics. 2012;13(1):52.

264. Simon MD, Geim AK. Diamagnetic levitation: Flying frogs and floating magnets. J Appl Phys. 2000;87(9):6200–4.

265. Hammer BE, Kidder LS, Williams PC, Xu WW. Magnetic levitation of MC3T3 osteoblast cells as a ground-based simulation of microgravity. Microgravity Sci Technol.

2009;21(4):311.

266. Gao H, Ayyaswamy PS, Ducheyne P. Dynamics of a microcarrier particle in the simulated microgravity environment of a rotating-wall vessel. Microgravity Sci Technol. 1997;10(3):154–65.

267. Schwarz RP, Goodwin TJ, Wolf DA. Cell culture for three-dimensional modeling in rotating-wall vessels: an application of simulated microgravity. J tissue Cult methods. 1992;14(2):51–7.

268. Rucci N, Migliaccio S, Zani BM, Taranta A, Teti A. Characterization of the osteoblast-like cell phenotype under microgravity conditions in the NASA-approved rotating wall vessel bioreactor (RWV). J Cell Biochem. 2002;85(1):167–79.

269. Svejgaard B, Wehland M, Ma X, Kopp S, Sahana J, Warnke E, et al. Common effects on cancer cells exerted by a random positioning machine and a 2d clinostat. PLoS One. 2015;10(8).

270. Qian AR, Li D, Han J, Gao X, Di SM, Zhang W, et al. Fractal dimension as a measure of altered actin cytoskeleton in MC3T3-E1 cells under simulated microgravity using 3-D/2-D clinostats. IEEE Trans Biomed Eng. 2012;59(5):1374–80.

271. Eiermann P, Kopp S, Hauslage J, Hemmersbach R, Gerzer R, Ivanova K. Adaptation of a 2-D clinostat for simulated microgravity experiments with adherent cells. Microgravity Sci Technol. 2013;25(3):153–9.

272. Russomano T, Cardoso RB, Falcao FP, Dalmarco G, dos Santos CR V, dos Santos LGF, et al. Development and Validation of a 3D Clinostat for the Study of Cells during Microgravity Simulation. In: 2005 IEEE Engineering in Medicine and Biology 27th Annual Conference. IEEE; 2006. p. 564–6.

273. Yamashita M, Yamashita A, Yamada M. Three dimensional (3D-) clinostat and its operational characteristics. Biol Sci Space. 1997;11(2):112–8.

274. Hauslage J, Cevik V, Hemmersbach R. Pyrocystis noctiluca represents an excellent bioassay for shear forces induced in ground-based microgravity simulators (clinostat and random positioning machine). NPJ microgravity. 2017;3(1):1–7.

275. Klaus DM, Todd P, Schatz A. Functional weightlessness during clinorotation of cell suspensions. Adv Sp Res. 1998;21(8–9):1315–8.

276. Qian A-R, Gao X, Zhang W, Li J-B, Wang Y, Di S-M, et al. Large gradient high magnetic fields affect osteoblast ultrastructure and function by disrupting collagen I or fibronectin/αβ1 integrin. PLoS One. 2013;8(1).

277. van Loon JJWA. Some history and use of the random positioning machine, RPM, in gravity related research. Adv Sp Res. 2007;39(7):1161–5.

278. Kim YJ, Jeong AJ, Kim M, Lee C, Ye S-K, Kim S. Time-averaged simulated microgravity (taSMG) inhibits proliferation of lymphoma cells, L-540 and HDLM-2, using a 3D clinostat. Biomed Eng Online. 2017;16(1):48.

279. Shao M-Z, Badler N. Spherical sampling by archimedes' theorem. Tech Reports. 1996;184.

280. Shamos MI, Hoey D. Geometric intersection problems. In: 17th Annual Symposium on Foundations of Computer Science (sfcs 1976). IEEE; 1976. p. 208–15.

281. Wood J, Kim S. Plane Sweep Algorithm. 2008.

282. Lee LM, Liu AP. The application of micropipette aspiration in molecular mechanics of single cells. J Nanotechnol Eng Med. 2014;5(4).

283. Sarkar D, Nagaya T, Koga K, Nomura Y, Gruener R, Seo H. Culture in vector-averaged

gravity under clinostat rotation results in apoptosis of osteoblastic ROS 17/2.8 cells. J Bone Miner Res. 2000;15(3):489–98.

284. Li QS, Lee GYH, Ong CN, Lim CT. AFM indentation study of breast cancer cells. Biochem Biophys Res Commun. 2008;374(4):609–13.

285. Nassef MZ, Kopp S, Wehland M, Melnik D, Sahana J, Krüger M, et al. Real microgravity influences the cytoskeleton and focal adhesions in human breast cancer cells. Int J Mol Sci. 2019;20(13):3156.

286. Chen Z, Luo Q, Lin C, Kuang D, Song G. Simulated microgravity inhibits osteogenic differentiation of mesenchymal stem cells via depolymerizing F-actin to impede TAZ nuclear translocation. Sci Rep. 2016;6(1):1–11.

287. Dai Z, Wu F, Chen J, Xu H, Wang H, Guo F, et al. Actin microfilament mediates osteoblast Cbfa1 responsiveness to BMP2 under simulated microgravity. PLoS One. 2013;8(5):e63661.

288. Lee LM, Lee JW, Chase D, Gebrezgiabhier D, Liu AP. Development of an advanced microfluidic micropipette aspiration device for single cell mechanics studies. Biomicrofluidics. 2016;10(5):54105.

289. Lammerding J. Mechanics of the nucleus. Compr Physiol. 2011;1(2):783–807.

290. Schafer DA. Coupling actin dynamics and membrane dynamics during endocytosis. Curr Opin Cell Biol. 2002;14(1):76–81.

291. Farsad K, De Camilli P. Mechanisms of membrane deformation. Curr Opin Cell Biol. 2003;15(4):372–81.

292. Schmidt A, Hall MN. Signaling to the actin cytoskeleton. Annu Rev Cell Dev Biol. 1998;14(1):305–38.

293. Kadzik RS, Homa KE, Kovar DR. F-Actin Cytoskeleton Network Self-Organization Through Competition and Cooperation. Annu Rev Cell Dev Biol. 2020;36:35–60.

294. Vignjevic D, Kojima S, Aratyn Y, Danciu O, Svitkina T, Borisy GG. Role of fascin in filopodial protrusion. J Cell Biol. 2006;174(6):863–75.

295. Welch MD. The world according to Arp: regulation of actin nucleation by the Arp2/3 complex. Trends Cell Biol. 1999;9(11):423–7.

296. Knudsen KA, Soler AP, Johnson KR, Wheelock MJ. Interaction of alpha-actinin with the cadherin/catenin cell-cell adhesion complex via alpha-catenin. J Cell Biol. 1995;130(1):67–77.

297. Otey CA, Pavalko FM, Burridge K. An interaction between alpha-actinin and the beta 1 integrin subunit in vitro. J Cell Biol. 1990;111(2):721–9.

298. Robinson RC, Turbedsky K, Kaiser DA, Marchand J-B, Higgs HN, Choe S, et al. Crystal structure of Arp2/3 complex. Science (80-). 2001;294(5547):1679–84.

299. Higgs HN, Pollard TD. Regulation of actin polymerization by Arp2/3 complex and WASp/Scar proteins. J Biol Chem. 1999;274(46):32531–4.

300. Weaver AM, Heuser JE, Karginov A V, Lee W, Parsons JT, Cooper JA. Interaction of cortactin and N-WASp with Arp2/3 complex. Curr Biol. 2002;12(15):1270–8.

301. Goley ED, Welch MD. The ARP2/3 complex: an actin nucleator comes of age. Nat Rev Mol cell Biol. 2006;7(10):713–26.

302. Haviv L, Brill-Karniely Y, Mahaffy R, Backouche F, Ben-Shaul A, Pollard TD, et al. Reconstitution of the transition from lamellipodium to filopodium in a membrane-free system. Proc Natl Acad Sci. 2006;103(13):4906–11.

303. Vignjevic D, Yarar D, Welch MD, Peloquin J, Svitkina T, Borisy GG. Formation of

filopodia-like bundles in vitro from a dendritic network. J Cell Biol. 2003;160(6):951–62.

304. Machesky LM, Li A. Fascin: Invasive filopodia promoting metastasis. Commun Integr Biol. 2010;3(3):263–70.

305. Pontani L-L, Van der Gucht J, Salbreux G, Heuvingh J, Joanny J-F, Sykes C. Reconstitution of an actin cortex inside a liposome. Biophys J. 2009;96(1):192–8.

306. Mullins RD, Heuser JA, Pollard TD. The interaction of Arp2/3 complex with actin: nucleation, high affinity pointed end capping, and formation of branching networks of filaments. Proc Natl Acad Sci. 1998;95(11):6181–6.

307. Tsai F-C, Koenderink GH. Shape control of lipid bilayer membranes by confined actin bundles. Soft Matter. 2015;11(45):8834–47.

308. Simon C, Kusters R, Caorsi V, Allard A, Abou-Ghali M, Manzi J, et al. Actin dynamics drive cell-like membrane deformation. Nat Phys. 2019;15(6):602–9.

309. Dürre K, Keber FC, Bleicher P, Brauns F, Cyron CJ, Faix J, et al. Capping protein-controlled actin polymerization shapes lipid membranes. Nat Commun. 2018;9(1):1–11.

310. Brieher WM, Coughlin M, Mitchison TJ. Fascin-mediated propulsion of Listeria monocytogenes independent of frequent nucleation by the Arp2/3 complex. J Cell Biol. 2004;165(2):233–42.

311. Liu AP, Fletcher DA. Actin polymerization serves as a membrane domain switch in model lipid bilayers. Biophys J. 2006;91(11):4064–70.

312. Lipowsky R. Coupling of bending and stretching deformations in vesicle membranes. Adv Colloid Interface Sci. 2014;208:14–24.

313. Brill-Karniely Y, Ideses Y, Bernheim-Groswasser A, Ben-Shaul A. From branched networks of actin filaments to bundles. ChemPhysChem. 2009;10(16):2818–27.

314. Bashirzadeh Y, Wubshet NH, Liu AP. Confinement Geometry Tunes Fascin-Actin Bundle Structures and Consequently the Shape of a Lipid Bilayer Vesicle. Front Mol Biosci. 2020;7.

315. Maciver SK, Wachsstock DH, Schwarz WH, Pollard TD. The actin filament severing protein actophorin promotes the formation of rigid bundles of actin filaments crosslinked with alpha-actinin. J Cell Biol. 1991;115(6):1621–8.

316. Tan TH, Malik-Garbi M, Abu-Shah E, Li J, Sharma A, MacKintosh FC, et al. Self-organized stress patterns drive state transitions in actin cortices. Sci Adv. 2018;4(6):eaar2847.

317. Svitkina TM, Bulanova EA, Chaga OY, Vignjevic DM, Kojima S, Vasiliev JM, et al. Mechanism of filopodia initiation by reorganization of a dendritic network. J Cell Biol. 2003;160(3):409–21.

318. Bashirzadeh Y, Redford SA, Lorpaiboon C, Groaz A, Litschel T, Schwille P, et al. Actin crosslinker competition and sorting drive emergent GUV size-dependent actin network architecture. bioRxiv. 2020;

319. Pardee JD, Aspudich J. [18] Purification of muscle actin. Methods Enzymol. 1982;85:164–81.

320. Schneider CA, Rasband WS, Eliceiri KW. NIH Image to ImageJ: 25 years of image analysis. Nat Methods. 2012;9(7):671–5.

321. Schindelin J, Arganda-Carreras I, Frise E, Kaynig V, Longair M, Pietzsch T, et al. Fiji: an open-source platform for biological-image analysis. Nat Methods. 2012;9(7):676–82.

322. Xu T, Vavylonis D, Huang X. 3D actin network centerline extraction with multiple active contours. Med Image Anal. 2014;18(2):272–84.

323. Xu T, Vavylonis D, Tsai F-C, Koenderink GH, Nie W, Yusuf E, et al. SOAX: a software for quantification of 3D biopolymer networks. Sci Rep. 2015;5(1):1–10.

324. Pettersen EF, Goddard TD, Huang CC, Couch GS, Greenblatt DM, Meng EC, et al. UCSF Chimera—a visualization system for exploratory research and analysis. J Comput Chem. 2004;25(13):1605–12.

325. Tseng Y, Kole TP, Lee JSH, Fedorov E, Almo SC, Schafer BW, et al. How actin crosslinking and bundling proteins cooperate to generate an enhanced cell mechanical response. Biochem Biophys Res Commun. 2005;334(1):183–92.

326. Lieleg O, Claessens MMAE, Bausch AR. Structure and dynamics of cross-linked actin networks. Soft Matter. 2010;6(2):218–25.

327. Gittes F, Mickey B, Nettleton J, Howard J. Flexural rigidity of microtubules and actin filaments measured from thermal fluctuations in shape. J Cell Biol. 1993;120(4):923–34.

328. Gardel ML, Shin JH, MacKintosh FC, Mahadevan L, Matsudaira P, Weitz DA. Elastic behavior of cross-linked and bundled actin networks. Science (80-). 2004;304(5675):1301–5.

329. Gardel ML, Nakamura F, Hartwig J, Crocker JC, Stossel TP, Weitz DA. Stress-dependent elasticity of composite actin networks as a model for cell behavior. Phys Rev Lett. 2006;96(8):88102.

330. Stossel TP. Contribution of actin to the structure of the cytoplasmic matrix. J Cell Biol. 1984;99(1):15s-21s.

331. Schaefer A, Te Riet J, Ritz K, Hoogenboezem M, Anthony EC, Mul FPJ, et al. Actin-binding proteins differentially regulate endothelial cell stiffness, ICAM-1 function and neutrophil transmigration. J Cell Sci. 2014;127(20):4470–82.

332. Ketene AN, Schmelz EM, Roberts PC, Agah M. The effects of cancer progression on the viscoelasticity of ovarian cell cytoskeleton structures. Nanomedicine Nanotechnology, Biol Med. 2012;8(1):93–102.

333. Hu J, Zhou Y, Obayemi JD, Du J, Soboyejo WO. An investigation of the viscoelastic properties and the actin cytoskeletal structure of triple negative breast cancer cells. J Mech Behav Biomed Mater. 2018;86:1–13.

334. Kumar S, Weaver VM. Mechanics, malignancy, and metastasis: the force journey of a tumor cell. Cancer Metastasis Rev. 2009;28(1):113–27.

335. Miles FL, Pruitt FL, van Golen KL, Cooper CR. Stepping out of the flow: capillary extravasation in cancer metastasis. Clin Exp Metastasis. 2008;25(4):305–24.

336. Gokhin DS, Nowak RB, Khoory JA, Piedra A de la, Ghiran IC, Fowler VM. Dynamic actin filaments control the mechanical behavior of the human red blood cell membrane. Mol Biol Cell. 2015;26(9):1699–710.

337. Qiang Y, Liu J, Du E. Dielectrophoresis testing of nonlinear viscoelastic behaviors of human red blood cells. Micromachines. 2018;9(1):21.

338. Tekle E, Astumian RD, Chock PB. Selective and asymmetric molecular transport across electroporated cell membranes. Proc Natl Acad Sci. 1994;91(24):11512–6.

339. Nuccitelli R, Pliquett U, Chen X, Ford W, Swanson RJ, Beebe SJ, et al. Nanosecond pulsed electric fields cause melanomas to self-destruct. Biochem Biophys Res Commun. 2006;343(2):351–60.

340. Gothelf A, Mir LM, Gehl J. Electrochemotherapy: results of cancer treatment using enhanced delivery of bleomycin by electroporation. Cancer Treat Rev. 2003;29(5):371–87.

341. Heller R, Gilbert R, Jaroszeski MJ. Clinical applications of electrochemotherapy. Adv Drug Deliv Rev. 1999;35(1):119–29.

342. Golzio M, Teissié J, Rols M-P. Direct visualization at the single-cell level of electrically mediated gene delivery. Proc Natl Acad Sci. 2002;99(3):1292–7.

343. Heller LC, Heller R. In vivo electroporation for gene therapy. Hum Gene Ther. 2006;17(9):890–7.

344. Grosse C, Schwan HP. Cellular membrane potentials induced by alternating fields. Biophys J. 1992;63(6):1632–42.

345. Leung SL, Lu Y, Bluestein D, Slepian MJ. Dielectrophoresis-mediated electrodeformation as a means of determining individual platelet stiffness. Ann Biomed Eng. 2016;44(4):903–13.

346. Gass G V, Chernomordik L V, Margolis LB. Local deformation of human red blood cells in high frequency electric field. Biochim Biophys Acta (BBA)-Molecular Cell Res. 1991;1093(2–3):162–7.

347. Teng Y, Pang M, Huang J, Xiong C. Mechanical characterization of cancer cells during TGF-β1-induced epithelial-mesenchymal transition using an electrodeformation-based microchip. Sensors Actuators B Chem. 2017;240:158–67.

348. Teng Y, Zhu K, Xiong C, Huang J. Electrodeformation-based biomechanical chip for quantifying global viscoelasticity of cancer cells regulated by cell cycle. Anal Chem. 2018;90(14):8370–8.

349. Litschel T, Schwille P. Protein reconstitution inside giant unilamellar vesicles. Annu Rev Biophys. 2021;50:525–48.

350. Merkle D, Kahya N, Schwille P. Reconstitution and anchoring of cytoskeleton inside giant

unilamellar vesicles. ChemBioChem. 2008;9(16):2673–81.

351. Bashirzadeh Y, Redford SA, Lorpaiboon C, Groaz A, Litschel T, Schwille P, et al. Actin crosslinker competition and sorting drive emergent GUV size-dependent actin network architecture. Commun Biol [Internet]. 2021 Apr 21 [cited 2021 Sep 12];2020.10.03.322354. Available from: https://www.biorxiv.org/content/10.1101/2020.10.03.322354v3

352. Wubshet NH, Bashirzadeh Y, Liu AP. Fascin-induced actin protrusions are suppressed by dendritic networks in GUVs. Mol Biol Cell. 2021;mbc-E21.

353. Teissie J, Tsong TY. Electric field induced transient pores in phospholipid bilayer vesicles. Biochemistry. 1981;20(6):1548–54.

354. Riske KA, Dimova R. Electric pulses induce cylindrical deformations on giant vesicles in salt solutions. Biophys J. 2006;91(5):1778–86.

355. Yu M, Lira RB, Riske KA, Dimova R, Lin H. Ellipsoidal relaxation of deformed vesicles. Phys Rev Lett. 2015;115(12):128303.

356. Vlahovska PM. Voltage-morphology coupling in biomimetic membranes: dynamics of giant vesicles in applied electric fields. Soft Matter. 2015;11(37):7232–6.

357. Mauroy C, Portet T, Winterhalder M, Bellard E, Blache M-C, Teissié J, et al. Giant lipid vesicles under electric field pulses assessed by non invasive imaging. Bioelectrochemistry. 2012;87:253–9.

358. Knorr RL, Staykova M, Gracia RS, Dimova R. Wrinkling and electroporation of giant vesicles in the gel phase. Soft Matter. 2010;6(9):1990–6.

359. Dimova R, Bezlyepkina N, Jordö MD, Knorr RL, Riske KA, Staykova M, et al. Vesicles in electric fields: Some novel aspects of membrane behavior. Soft Matter.

2009;5(17):3201–12.

360. Dimova R, Riske KA, Aranda S, Bezlyepkina N, Knorr RL, Lipowsky R. Giant vesicles in electric fields. Soft Matter. 2007;3(7):817–27.

361. Vlahovska PM, Gracià RS, Aranda-Espinoza S, Dimova R. Electrohydrodynamic model of vesicle deformation in alternating electric fields. Biophys J. 2009;96(12):4789–803.

362. Nganguia H, Young Y-N. Equilibrium electrodeformation of a spheroidal vesicle in an ac electric field. Phys Rev E. 2013;88(5):52718.

363. Wu B, Veerapaneni S. Electrohydrodynamics of deflated vesicles: budding, rheology and pairwise interactions. J Fluid Mech. 2019;867:334–47.

364. Wagner O, Zinke J, Dancker P, Grill W, Bereiter-Hahn J. Viscoelastic properties of f-actin, microtubules, f-actin/α-actinin, and f-actin/hexokinase determined in microliter volumes with a novel nondestructive method. Biophys J. 1999;76(5):2784–96.

365. Wu X, Zhao Z, Kang Y, Ji X, Liu Y. Viscoelasticity of poly (ethylene glycol) in aqueous solutions of potassium sulfate: a comparison of quartz crystal microbalance with conventional methods. Polym J. 2019;51(5):471–80.

366. Zhao Z, Ji X, Dimova R, Lipowsky R, Liu Y. Viscoelasticity of poly (ethylene glycol) solutions on supported lipid bilayers via quartz crystal microbalance with dissipation. Macromolecules. 2015;48(6):1824–31.

367. Suarez C, Carroll RT, Burke TA, Christensen JR, Bestul AJ, Sees JA, et al. Profilin regulates F-actin network homeostasis by favoring formin over Arp2/3 complex. Dev Cell. 2015;32(1):43–53.

368. Burke TA, Christensen JR, Barone E, Suarez C, Sirotkin V, Kovar DR. Homeostatic actin cytoskeleton networks are regulated by assembly factor competition for monomers. Curr

Biol. 2014;24(5):579–85.

369. Hinner B, Tempel M, Sackmann E, Kroy K, Frey E. Entanglement, elasticity, and viscous relaxation of actin solutions. Phys Rev Lett. 1998;81(12):2614.

370. Falzone TT, Blair S, Robertson-Anderson RM. Entangled F-actin displays a unique crossover to microscale nonlinearity dominated by entanglement segment dynamics. Soft Matter. 2015;11(22):4418–23.

371. McNamee CE, Yamamoto S, Higashitani K. Effect of the physicochemical properties of poly (ethylene glycol) brushes on their binding to cells. Biophys J. 2007;93(1):324–34.

372. Sorichetti V, Ninarello A, Ruiz-Franco JM, Hugouvieux V, Kob W, Zaccarelli E, et al. Effect of chain polydispersity on the elasticity of disordered polymer networks. Macromolecules. 2021;54(8):3769–79.

373. Chugh P, Clark AG, Smith MB, Cassani DAD, Dierkes K, Ragab A, et al. Actin cortex architecture regulates cell surface tension. Nat Cell Biol. 2017;19(6):689–97.

374. Gilden J, Krummel MF. Control of cortical rigidity by the cytoskeleton: emerging roles for septins. Cytoskeleton. 2010;67(8):477–86.

375. Guevorkian K, Manzi J, Pontani LL, Brochard-Wyart F, Sykes C. Mechanics of Biomimetic Liposomes Encapsulating an Actin Shell. Biophys J. 2015;109(12):2471–9.

376. Hu J, Chen S, Hu W, Lü S, Long M. Mechanical point loading induces cortex stiffening and actin reorganization. Biophys J. 2019;117(8):1405–18.

377. Luo T, Mohan K, Iglesias PA, Robinson DN. Molecular mechanisms of cellular mechanosensing. Nat Mater. 2013;12(11):1064–71.

378. Wubshet NH, Liu AP. Methods to mechanically perturb and characterize GUV-based minimal cell models. Comput Struct Biotechnol J. 2022;

379. Yashar B, Nadab W, Thomas L, Petra S. Rapid encapsulation of reconstituted cytoskeleton inside giant unilamellar vesicles. 2021;

380. Olbrich K, Rawicz W, Needham D, Evans E. Water permeability and mechanical strength of polyunsaturated lipid bilayers. Biophys J. 2000;79(1):321–7.

381. Uchida N, Grest GS, Everaers R. Viscoelasticity and primitive path analysis of entangled polymer liquids: From F-actin to polyethylene. J Chem Phys. 2008;128(4):44902.

382. Bavi N, Nakayama Y, Bavi O, Cox CD, Qin Q-H, Martinac B. Biophysical implications of lipid bilayer rheometry for mechanosensitive channels. Proc Natl Acad Sci. 2014;111(38):13864–9.

383. Atcha H, Jairaman A, Holt JR, Meli VS, Nagalla RR, Veerasubramanian PK, et al. Mechanically activated ion channel Piezo1 modulates macrophage polarization and stiffness sensing. Nat Commun. 2021;12(1):3256.

384. Li C, Zhang X, Yang B, Wei F, Ren Y, Mu W, et al. Reversible deformation of artificial cell colonies triggered by actin polymerization for muscle behavior mimicry. Adv Mater. 2022;34(34):2204039.

385. Melcher JR, Taylor GI. Electrohydrodynamics: a review of the role of interfacial shear stresses. Annu Rev Fluid Mech. 1969;1(1):111–46.

386. Rahimian A, Veerapaneni SK, Biros G. Dynamic simulation of locally inextensible vesicles suspended in an arbitrary two-dimensional domain, a boundary integral method. J Comput Phys. 2010;229(18):6466–84.

387. Veerapaneni S. Integral equation methods for vesicle electrohydrodynamics in three dimensions. J Comput Phys. 2016;326:278–89.

388. Yoon G. Dielectric properties of glucose in bulk aqueous solutions: Influence of electrode

polarization and modeling. Biosens Bioelectron. 2011;26(5):2347–53.

389. Telis VRN, Telis-Romero J, Mazzotti HB, Gabas AL. Viscosity of aqueous carbohydrate solutions at different temperatures and concentrations. Int J food Prop. 2007;10(1):185–95.

390. McConnell LC, Vlahovska PM, Miksis MJ. Vesicle dynamics in uniform electric fields: squaring and breathing. Soft Matter. 2015;11(24):4840–6.

391. Gonzalez-Tello P, Camacho F, Blazquez G. Density and viscosity of concentrated aqueous solutions of polyethylene glycol. J Chem Eng Data. 1994;39(3):611–4.

392. Burnett S, van Iersel M, Thomas P. PEG-8000 alters morphology and nutrient concentration of hydroponic impatiens. HortScience. 2005;40(6):1768–72.